TECHNISCHE UNIVERSITÄT MÜNCHEN

TUM School of Natural Sciences

Developing Rigid DNA Origami Structures for High-Resolution Cryo-EM Applications

Sayed Ali Khoshouei Esfahani

Vollständiger Abdruck der von der TUM School of Natural Sciences der Technischen Universität München zur Erlangung des akademischen Grades eines

Doktors der Naturwissenschaften (Dr. rer. nat.)

genehmigten Dissertation.

Vorsitz:	Prof. Dr. Martin Zacharias
Prüfende der Dissertation:	1. Prof. Dr. Hendrik Dietz
	2. Prof. Dr. Friedrich C. Simmel

Die Dissertation wurde am 10.07.2024 bei der Technischen Universität München eingereicht und durch die TUM School of Natural Sciences am 11.10.2024 angenommen

TUM School of Natural Sciences

Technische Universität München

Developing Rigid DNA Origami Structures for High-Resolution Cryo-EM Applications

Dissertation by
Ali Khoshouei

List of peer-reviewed publications

- **Designing Rigid DNA Origami Templates for Molecular Visualization using Cryo-EM**

  Ali Khoshouei, Georg Kempf, Volodymyr Mykhailiuk, Johanna Grießing, Maximilian Honemann, Lukas Kater, Simone Cavadini, and Hendrik Dietz
  Nano Lett. 2024, 24, 16, 5031–5038

- **Triple-Stranded DNA As a Structural Element in DNA Origami**

  Ken Sachenbacher, Ali Khoshouei, Maximilian Nicolas Honemann, Wouter Engelen, Elija Feigl, and Hendrik Dietz
  ACS Nano 2023, 17, 10, 9014–9024

- **Scalable protein design using hallucination in a relaxed sequence space**

  Christopher Frank, Ali Khoshouei, Lara Fuß, Yosta de Stigter, Dominik Schiewitz, Dominik Putz, Lara Weber, Zhixuan Zhao, Motoyuki Hattori, Shihao Feng, Sergey Ovchinnikov, and Hendrik Dietz
  Submitted

- **Mono-exponential Current Attenuation with Distance across 16 nm Thick Bacteriorhodopsin Multilayers**

  Domenikos Chryssikos, Jerry A. Fereiro, Jonathan Rojas, Sudipta Bera, Defne Tüzün, Evanthia Kounoupioti, Rui N. Pereira, Christian Pfeiffer, Ali Khoshouei, Hendrik Dietz, Mordechai Sheves, David Cahen, and Marc Tornow
  Submitted

Table of Contents

Abstract

DNA origami is a technique that utilizes DNA molecules to accurately assemble two-dimensional and three-dimensional nanostructures. The precision and addressability of DNA origami are particularly crucial for scaffolding applications that necessitate the precise placement of DNA or non-DNA functional elements onto DNA origami structures.

In our research, we aimed to improve the compactness and functionality of DNA origami. Our analysis focused on two main areas: design parameters, such as the density of scaffold crossovers and the varying lengths of the staple strands, and ensuring the compositional consistency of the staple strands. These factors were investigated to understand their impact on the rigidity of the DNA origami. We utilized cryogenic electron microscopy (cryo-EM) single-particle analysis, a cutting-edge technique known for its high-resolution capabilities, to gain deeper insight into these interactions and outcomes.

We used our optimized compact DNA origami structure as a robust host-guest alignment framework. We characterized and determined its structure after successfully integrating an 8kDa Thrombin Binding Aptamer (TBA) into our DNA origami substrate. We have demonstrated that when DNA origami platforms are finely tuned and optimized, they can be used as scaffolds for precise molecular positioning, especially within cryo-EM novel structural applications.

Introduction

Programmable self-assembly using DNA is a method for nanofabrication that has applications in various fields [1, 2]. DNA origami allows the construction of nanostructures by folding a long single-stranded DNA, known as the scaffold. The process of folding DNA origami begins with the strategic integration of short single-stranded DNA segments, known as staples. The staples bind to specific scaffold sections through sequence-specific hybridization to form the desired nanostructure. DNA origami utilizes DNA strands to create molecular structures, like how traditional origami transforms paper into art through folding. This method can potentially drive advancements in numerous fields, especially biomedical applications. It offers new ways to interact with biological systems at the nanoscale [2-10].

One of the uses of DNA origami lies in its capacity to function as an accurate template at the molecular level. This enables the precise placement of DNA and non-DNA elements, opening possibilities for discoveries in molecular research. Various factors, such as material quality and folding complexities, can lead to imperfections in origami structures [8, 11, 12]. Our study focused on refining and enhancing the elements required for folding DNA origami. Our efforts involved analyzing the design parameters and assessing the purity of the staple strands used to fold DNA origami [7, 13]. Our experiments cover a wide range, from adjusting crossover densities and staple lengths to using various purification methods.

Understanding the structural features of DNA origami is challenging due to the intricate flexibility arising from lattice breathing, but it is essential for their implementation in various applications [14]. Cryo-EM is an advanced imaging technique that determines biological molecules' and complexes' three-dimensional (3D) structures at near-atomic resolution [15-18]. Previous research has demonstrated cryo-EM's ability to reconstruct the 3D structure of DNA origami and show structural features, such as the DNA's major and minor grooves [14, 19-21]. To investigate and probe the changes in DNA origami structure that

result from design modifications and material consistency, we used the capabilities of cryo-EM imaging and the current advancement in data processing. We have combined high-resolution cryo-EM imaging with electrophoretic mobility analysis to provide feedback mechanisms.

Although cryo-EM is a powerful method for structural investigation, it also has limitations that don't allow it to reach subatomic resolution for biological samples. One of the challenges is the lack of sufficient signal-to-noise ratio (SNR), which is a bottleneck for imaging smaller molecular structures. This issue is more pronounced in single-particle analysis (SPA), where achieving high contrast without damaging the biological sample using a high electron dose is challenging [22]. Distinguishing the proteins below a specific molecular weight threshold from the background noise is impossible. Therefore, the alignment and averaging of the particles, crucial for SPA data analysis, becomes impossible [23]. Proteins with a molecular weight below approximately 38 kDa were considered too small for practical analysis by cryo-EM [24].

Recent advancements in microscope components have enhanced the SNR in cryo-EM. These include using more coherent electron sources, employing energy filters, volta phase plates [25, 26], and state-of-the-art high-end detectors [27]. Additionally, improvements in data processing can be helpful at lower SNR levels. Although the mentioned methods help improve the SNR, we are still limited by the molecular weight. Therefore, Another approach to address this limitation is using the scaffolding method [28].

This approach involves fusing a minor protein of interest with a larger, more easily identifiable structure, creating a scaffold. As a result, the molecular weight increases beyond the mentioned threshold. This method has successfully solved various protein structures in cryo-EM studies [29-33]. One example using this scaffolding method is using Green Fluorescent Protein (GFP), a protein with a molecular weight of 26 kDa [32].

DNA origami can be a scaffold to improve the SNR due to its inherent adaptivity and precision. This capability of DNA origami is especially promising for nucleic acid-based molecules, including aptamers, ribozymes, and DNAzymes. Earlier research has highlighted the potential of DNA origami in enhancing cryo-EM imaging for understanding protein structures [19, 34]. Our study aims to use compact DNA origami structures to improve the cryo-EM SPA outcomes.

DNA Origami

Biomolecules like amino and nucleic acids can self-assemble into complex structures like organelles and cells, essential for life. The activity of living organisms is influenced by biological processes, which happen at different scales, from molecular and cellular levels to the organismal levels. Nucleosome remodeling can alter the accessibility of DNA to transcription factors and RNA polymerase, thus modifying gene expression. Motor proteins transport the essential cargo within the cell to maintain cellular organization, signaling, and function. Cells interact to share resources, coordinate actions, and respond to environmental changes through direct contact and through signaling molecules. Much research has been performed to explore these processes. One challenge in the field is related to precision and demanding experimental conditions. DNA origami can fulfill the precision and experimental requirements due to its programmability and nanoscale accuracy. It provides a strong foundation for investigating biological functions and revealing the complex processes that govern life at the molecular level (Figure *1*).

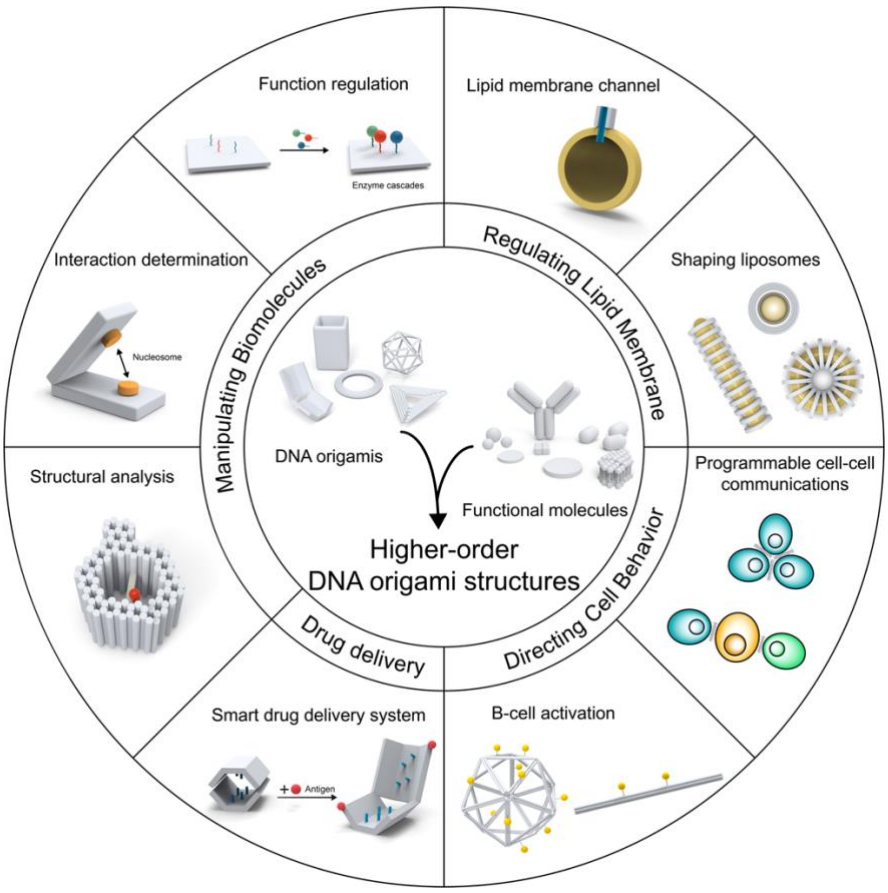

Figure 1: Construction of Complex DNA Origami Structures for Multiscale Biological Applications: This includes manipulating biomolecules, regulating lipid membranes, directing cellular behavior, and facilitating targeted drug delivery [35].

DNA molecules, fundamental to all known life forms, are crucial for storing and transmitting genetic information [36]. In materials and biomedical engineering, DNA has emerged as a promising alternative to various natural and synthetic polymers traditionally employed in biomedical fields like drug delivery and cancer immunotherapy [37-41]. Unlike traditional polymeric materials, DNA-based materials provide nanoscale programmability and exhibit unique structural and biochemical characteristics [42, 43]. These properties make them suitable for constructing complex nanostructures and arranging various biomolecules and inorganic substances with nanometer precision [42-46].

DNA molecules primarily exist as B-form double-stranded DNA (dsDNA) in their natural state. The dsDNA consists of two complementary single strands of DNA (ssDNA) connected through Watson-Crick base pairing [47]. This structure forms

a right-handed double helix about 2 nm wide, with a repeating pattern of 10.5 bases per turn and a 3.4 Å spacing between each base pair [36, 47].

The predictability of DNA assembly and the specificity of DNA sequences have contributed to the growth of structural DNA nanotechnology [46, 48-50]. Nadrian Seeman initiated the work in creating nanostructures using DNA [51], and the field advanced further with the advent of DNA origami in 2006 by Paul Rothemund [52]. DNA origami has been used in diverse fields, including nanofabrication [53], nanorobotics [54], nanomedicine[55], biological computing[56], and fundamental science [57]. This technique involves a long, circular DNA strand acting as a scaffold that is folded into specific shapes by binding with custom-designed shorter DNA staples. The final structure is determined by the sequence of these staples.

The assembly process includes mixing the scaffold with an excess of staples in a buffer, heat to 90°C, and then letting it cool gradually to room temperature, allowing the desired structure to form (Figure *2*a) [58]. DNA origami allows for the creation of larger and more stable structures than earlier DNA nanotechnology efforts. These constructs can even assemble into superstructures with weights in the megadalton range (Figure *2*b) [52]. DNA origami was initially limited to 2D structures. In 2009, Andersen et al. folded three-dimensional shapes, such as a hollow box with an operable lid [59].

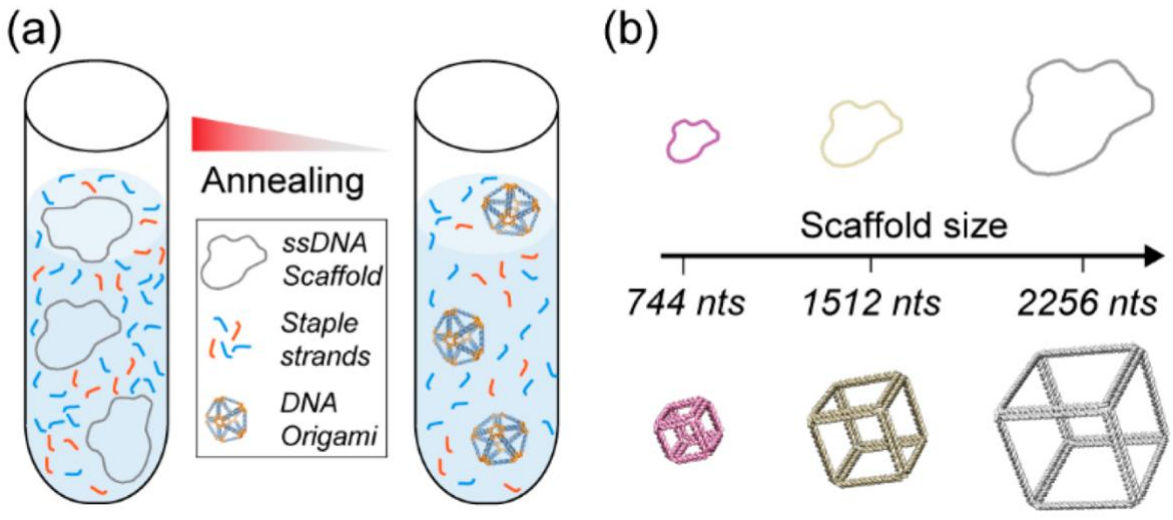

Figure 2: Assembly of DNA Origami Nanoparticles. (a) DNA origami structures are created using a lengthy single-stranded DNA scaffold combined with

numerous staple strands, employing a thermal annealing technique for folding. (b) Tailoring the size of DNA origami by customizing the length of the scaffold strands [60].

William Shih introduced a method to create 3D structures with a honeycomb cross-section capable of creating different shapes [6]. Andersen's approach involved using crossover points, like two-dimensional origami, occurring at each complete rotation of the DNA strand. Shih's technique increased the frequency of crossovers to every seven base pairs, resulting in a more complex 3D structure. Shih's DNA origami technique allows for complex 3D nanostructures featuring a honeycomb lattice. In a honeycomb lattice configuration, it is possible to connect to the adjacent helix using a crossover at a 240° angle, and this pattern repeats every 21 base pairs. When assembling 3D lattice origamis compared to their 2D counterparts, a key difference lies in the annealing time. While planar origamis fold relatively quickly, often within hours, 3D structures require significantly longer, sometimes days. This extended time is due to the complexity of the design and the buffer composition, which can affect the temperature needed for the hybridization. For example, having divalent cations in the buffer can improve successful folding compared to having monovalent cations. 3D origamis face more complex kinetic traps because of denser crossover arrangement and undergoing multiple folding and unfolding phases during annealing. Additionally, due to their multi-layered structure, 3D origamis with higher DNA density require a slower temperature gradient during folding. This gradual approach gives each part of the structure sufficient time to reach its optimal folding temperature, increasing the likelihood of successfully navigating kinetic traps. The Shih group also developed a method for creating square-lattice 3D DNA origami [8]. By arranging crossovers every 8 base pairs, or approximately 76% of a helical turn, they could achieve an angle of 274° between adjacent crossovers. This setup allows helices to interact at nearly right angles. However, since the angle isn't exactly 90 degrees, it introduces torsional strain. This slightly unwinds the DNA to an average of 10.67 base pairs per turn, causing a right-handed twist in the structure. To counteract this strain, base pairs are strategically removed from each helix at certain points, aligning the average base pair density more closely with the 10.5 base pairs per turn, typical of regular B-form DNA. They developed and introduced a software called caDNAno, specifically designed for crafting honeycomb and square-lattice 3D origami [7].

Dietz group introduced a new set of dynamic origami consisting of multiple individually assembled origami units that are later connected through shape complementarity instead of base pairing [54]. One origami piece had a pocket designed to fit a protrusion from another piece. Successful fitting resulted in increased stability due to stacking interactions between the protrusion and pocket terminal base pairs. This design principle facilitated the creation of homogeneous and heterogeneous multimeric structures. Multimers can grow to micrometer sizes and achieve gigadalton molecular weights. These developments also included lattices and reconfigurable structures, with conformation control achievable through cation concentration or temperature alterations.

In a separate study, shape complementarity was utilized to create a rotary device using three precisely fitting components: two clamp units and a rotor unit. The clamps are designed with pockets to fit the protrusions on the rotor [61]. Once the clamps were assembled, they were locked around the rotor using complementary DNA strands, creating a mechanical interlock. This design allowed the rotor high rotational freedom while restricting its translational movement. The rotor's free rotation was confirmed using total internal reflection fluorescence microscopy. However, it was only driven by Brownian motion, lacking controllable directionality. This experiment demonstrated the potential of constructing dynamic and engineered machines using separate DNA origami components.

Biomedical applications of DNA origami face challenges due to the low stability of DNA nanostructures, especially in biological fluids [62, 63]. Factors like low magnesium ions create these challenges, and the activity of nucleases can lead to structural disintegration, shrinking their operational lifespan [64]. We can use encapsulation [65], transfer structural patterns into alternative materials [66], and reinforce staple strands through chemical [67] and enzymatic methods [68] or covalent cross-linking [69] to protect DNA nanostructure from environmental conditions. DNA nanostructures' stability can significantly depend on their geometry and internal structural details, influencing their endurance against enzymatic breakdown and adaptability to varying conditions [70-72]. Design parameters like lattice type, staple lengths, crossover distribution, relative space,

and twist correction can effectively determine DNA origami's structural and mechanical properties, essential to their behavior in various environmental conditions [73, 74]. Studies, such as those by Chandrasekaran et al. [75], have shown that more crossovers in paranemic crossover (PX) DNA nanostructures translate to heightened nuclease resistance. In DNA origami, the number of staple crossovers determines mechanical strength, and the lower number of staple crossovers leads to increased flexibility and local movement [76, 77]. This flexibility is a critical factor in the susceptibility of DNA origami to nucleases, influencing the trajectory of their enzymatic breakdown. Moreover, the routing and length of the staple strands that make these crossovers also affect the origami's folding endurance and stability in challenging conditions such as high temperatures or disruptive environmental factors[78, 79].

Yang Xin et al.'s research [80] demonstrates how the arrangement and density of inter-helical crossovers in DNA nanostructures directly impact their environmental stability and mechanical properties. The study analyzed two DNA origami structures consisting of six-helix bundles with crossovers spaced at different intervals. The study indicated that raising the number of crossovers enhances DNA origami's strength against nuclease attack by restricting enzyme access. Increasing the number of crossovers also reduces stability in environments with low magnesium ion concentrations due to decreased structure flexibility. This finding is critical for altering ionic conditions and enzymatically active biological fluids. The implications for designing DNA origami-based drug delivery systems are particularly promising, as crossover engineering could allow for fine-tuning drug release profiles while maintaining structural integrity.

In a 2016 study by Funke et al. [81] at Dietz Lab, a DNA origami-based force spectrometer was developed to quantify the conformations of biomolecular assemblies under various environmental conditions. This DNA origami tool analyzes the salt-induced disassembly of nucleosome particles, providing insights into how varying ionic strengths can cause nucleosomes to change between tightly bound and open states. The spectrometer enabled the measurement of nucleosome dissociation constants, revealing a range from low ion concentration to high ion concentration. This research displayed the DNA origami spectrometer's ability to capture these dissociation dynamics with high

resolution using advanced imaging techniques such as TEM and FRET. The utility of DNA origami highlights its potential for studying biomolecular interactions and stability. It provides a platform for studying complex biological processes, such as protein folding and the dynamic behavior of large molecular structures.

In another study conducted by the same team in 2016, Funke et al. [82] employed a DNA origami-based force spectrometer to explore the energy landscape of nucleosome interactions, aiming to discover chromatin structures and their regulatory roles in the genome. Subnanometer-resolution measurements of nucleosome-nucleosome distances were achieved by integrating two nucleosomes into the spectrometer using single-particle electron microscopy. Analysis of these measurements enabled the mapping of a Boltzmann-weighted energy landscape. It revealed a long-range attractive potential between nucleosome pairs, approximately 6 nm in range, with a minimum energy of -1.6 kcal/mol near close contact points. The orientation of nucleosomes had minimal impact on their interaction; however, modifications such as histone H4 acetylation or the removal of histone tails significantly weakened these interactions. These insights provide an understanding of chromatin dynamics and demonstrate the utility of the DNA origami force spectrometer as a precise tool for studying molecular interactions at high resolution.

Dietz's group scaled up DNA origami assembly by three orders of magnitude compared to chemical synthesis by using bacteria and bacteriophage DNA. This method is effective for producing large quantities of identical origami structures. The technique involves encoding the staple strands into a phagemid with two Zn^{2+}-dependent self-cleaving DNAzymes flanking each staple. The phagemid and a helper plasmid containing the scaffold are replicated in the bacteria via rolling circle amplification. The phagemid is isolated and exposed to $ZnCl_2$, releasing the staples, and it can be used to fold DNA origami. Conventional assembly methods are used after removing $ZnCl_2$ from the buffer.

Drug delivery systems are promising in DNA origami applications. DNA origami is a nanoscale carrier for pharmaceuticals, capable of switching between open and closed states. The drug is securely enclosed in the closed state, preventing unintended interactions. Aptamers [83-85] are typically used to trigger these

conformational changes; they open the origami structure when encountering specific target molecules, thereby releasing the drug. The use of different aptamers allows responsiveness to various targets. Beyond drug delivery, DNA origami has been used to create synthetic membrane ion channels [86], offering the potential for intracellular payload delivery.

In 2021, Sigl et al. utilized the principle of shape complementarity in DNA origami to develop a structure capable of binding to and neutralizing viruses [87]. They engineered triangular DNA origami subunits, programmed with virus-binding molecules, that assemble into octahedral or icosahedral containers, scaling up to 925 MDa. This technique was successfully applied to hepatitis-B core particles and adeno-associated viruses. In their experiments, the origami structures could inhibit hepatitis-B interactions in vivo and prevent infection in human cells exposed to AAV2, demonstrating a novel approach to fighting viral infections.

Kretzmann et al.'s 2023 study on DNA origami demonstrates an approach to gene delivery by constructing nanoscale objects specifically designed for targeted gene expression in mammalian cells [88]. Their research highlights the capacity of these DNA origami constructs to deliver genes effectively. It allows for the precise control of gene expression levels and the co-delivery of multiple genes. Strategic design elements, such as virus-inspired motifs and responsive crosslinkers, enhance gene expression. DNA Origami offers a platform for advancing gene therapy techniques, highlighting its potential in future biomedical applications.

Significant advancements in DNA origami have occurred in the past two decades. Researchers have repurposed DNA as a material for construction despite its natural limitations. The techniques for folding and shaping DNA are both straightforward and innovative. Additionally, software tools simplify the design process and enable scientists to create DNA origami for various applications quickly and precisely. The potential applications of this field are extensive and continue to expand as more scientists explore the capabilities of DNA origami.

Electron Microscopy

Detailed imaging of objects can be achieved using light or electron microscopes, which rely on radiation for visualization. Optical microscopes utilize light sources positioned beneath the specimens. For samples thin enough to allow light penetration, details become visible; otherwise, they appear opaque. A condenser lens directs light to the specimen, illuminating a specific point on its surface. When molecules encounter white light, they either absorb or reflect it based on its properties, creating an image with varying color and contrast. When processed through lenses, this image offers a magnified view to the observer.

Electron microscopes employ electron beams as the primary illuminating source. These microscopes operate in a vacuum environment, essential for allowing electrons to move freely. The behavior of electrons in this environment parallels that of photons, showcasing a wave-particle duality. Their advantage lies in their shorter wavelengths compared to visible light, enabling them to resolve and capture much finer structural details down to atomic scales in some advanced versions.

In electron microscopes, magnetic and electric fields are used as lenses to guide, focus, and manipulate the electron beams instead of conventional glass lenses. These fields control the trajectory of the electrons, ensuring optimal interaction with the specimen. When the high-energy electron beam interacts with a sample, it can either pass through or scatter from the atoms in the specimen. This interaction provides contrast and compositional details, vital for imaging.

The Transmission Electron Microscope (TEM) requires samples to be ultra-thin, often around 100 nanometers in thickness [89]. Some electrons are absorbed or scattered as the beam passes, while others transmit through unaltered. The transmitted electrons form an image on a detector, then converted into a visual representation. It's important to note that since the human eye can't directly perceive electrons, these microscopes use phosphorescent screens or digital detectors to capture the patterns of transmitted electrons and convert them into greyscale images. Here, the contrast corresponds to variations in sample

thickness, atomic structure, and density. Furthermore, advancements in electron microscopy, such as cryo-EM single particle analysis, allow for imaging biological specimens in near-native states, opening doors to unprecedented insights into molecular biology and biochemistry.

In essence, while optical microscopes offer a broader view of specimens, electron microscopes, with their intricate mechanisms and advanced techniques, provide atomic-level insights, making them invaluable tools in scientific research.

Basic Components of an Electron Microscope

In 1931, Max Knoll and Ernst Ruska developed the transmission electron microscope. While there have been numerous advancements in electron microscopy, the fundamental design has remained consistent. The quality of the resulting image depends on factors such as resolution, contrast, and the signal-to-noise (S/N) ratio. Over the years, the resolution of electron microscopes has significantly improved, progressing from an initial 100 nm in the early models to an impressive 1Å in modern ones. Electrons travel approximately one to two meters from top to bottom within the high-vacuum column of the microscope. Critical components of an electron microscope include the electron sources, condenser lenses, specimen holders, objective lenses, projector lenses, and screens and cameras, as shown in Figure *3*. Each of these elements plays a crucial role in determining the clarity and quality of the final image [90].

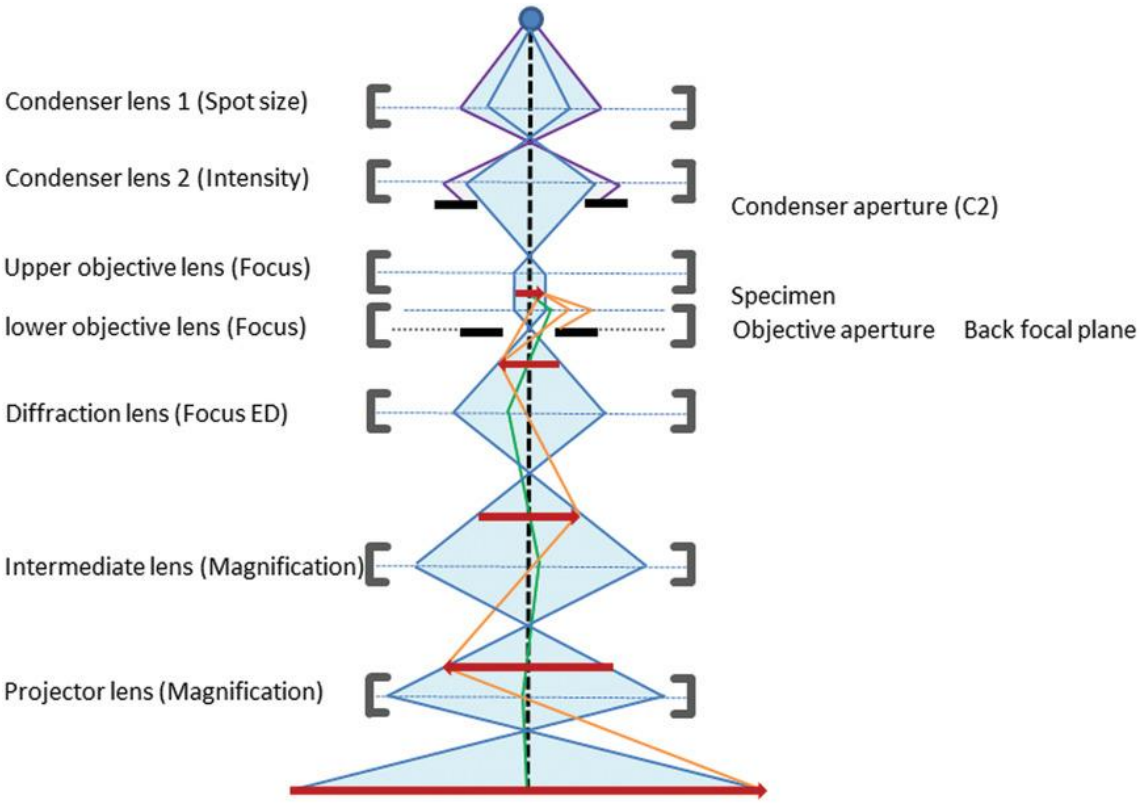

Figure 3: This diagram illustrates the electron microscope. The beam is highlighted in blue; gray brackets represent lenses labeled with their names and the microscope function that controls them; black bars represent apertures; and the red arrow indicates the specimen and its (intermediate) image. Orange and green lines represent scattered electron paths [90].

Electron gun

The performance of a source can be described by three parameters: stability, brightness, and coherence. The stability of an electron source is determined by the fluctuations in its electron current, often referred to as emission. Brightness refers to the current density radiated per unit solid angle (A cm^{-2} sr^{-1}).

Electron beam coherence is divided into spatial and temporal types. A beam is considered coherent when the electrons emit from a singular point, all sharing an identical wavelength and phase [91]. A source has a heightened level of spatial coherence when it approximates a point-like structure. It is hypothesized that as electrons emit from a wide area, the fine details in the image fade more quickly. This information decay is explained by the spatial coherence envelope function, expressed as a function of frequency (q). Here, Cs represents the objective lens's spherical aberration, λ represents the electron's wavelength, Δz is the predominant defocus, and α_i denotes the illumination angle's half-opening. The mathematical representation is:

$$K_s(q) = \exp\left[\frac{-(\pi C_s \lambda^2 q^3 - \pi \Delta \mathrm{zq})^2 \alpha_i^2}{\ln(2)}\right]$$

The coherence of an electron beam is fixed, but its impact on imaging can be enhanced through adjustments to the envelope function. One can employ a Cs corrector to decrease spherical aberration, increase the acceleration voltage to reduce the wavelength, and apply minimal defocus, although these changes might reduce contrast. Crucially, to narrow down the effective size of the electron source, the C2 lens cross-over can be adjusted by increasing the current, which is only viable if parallel illumination isn't required. In such instances, the cross-over should align with the objective lens's front focal plane for optimal results. Additionally, achieving the largest possible spot size by increasing the Condenser lens 1 current reduces beam intensity. This reduction should not lead to a lower C2 current, which would counteract improvements in coherence. The beam's spatial coherence depends on the minimum dose rate detectable by the detector for image capture. Reducing the aperture size of C2 can improve coherence in

focused beam applications. However, parallel or diverging illumination mainly involves filtering electrons from the source's core, primarily adjusting the beam width. The degree of spatial coherence is crucial as it directly impacts the clarity of phase-contrast images and the precision of electron diffraction patterns. These are essential for high-quality imaging of crystalline structures.

Temporal coherence, also known as coherence length, refers to the uniformity of electron wavelengths in a beam. It is related to the stability of the power supply and the variation in electron velocity relative to the beam's total voltage or energy spread (ΔE/E (eV)). The function representing temporal coherence is mathematically expressed as:

$$K_c(q) = \exp\left[-\left(\frac{\pi\lambda q^2 H}{4\sqrt{\ln(2)}}\right)^2\right] \text{ where } H = C_c\frac{\Delta E}{E}f_r$$

Here, λ symbolizes the wavelength of the electrons, Cc is the coefficient representing chromatic aberration within the lenses, and ΔE/E refers to the relative energy spread. The temporal coherence can be enhanced by higher acceleration voltages, which reduce the wavelength and narrow the relative energy spread. Also, a monochromator can refine the energy spread (ΔE) to achieve resolutions below one angstrom [92].

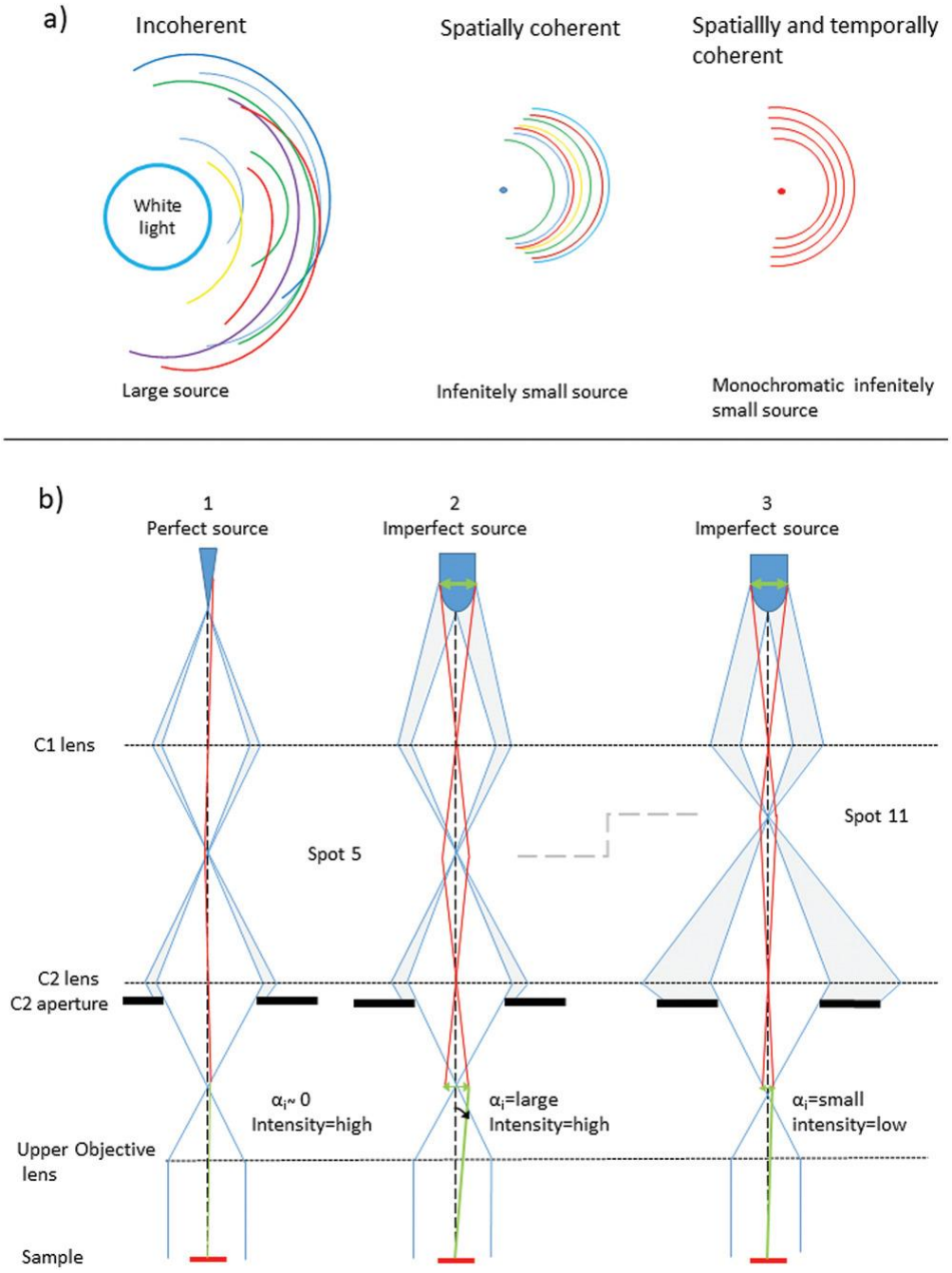

Figure 4: Spatial and Temporal Coherence: a) Incoherent sources release light or electrons with varying wavelengths and do not emerge from a singular point. Spatial coherence measures how closely the source resembles a single point, while temporal coherence relates to the uniformity of the emitted wavelengths. b) In TEM, spatial coherence is influenced by the physical size of the source, for instance, comparing a thermionic gun to a field emission gun, with the latter being closer to an ideal point source. An ideal point source results in an illumination angle that is effectively zero (b1). If the source is less than ideal, improvements can be made by increasing the distance between the sample and the cross-over via strengthening the C2 lens. However, this is fixed in a parallel illumination setup with a dual condenser lens system. The finest spatial coherence is also achieved with the largest possible spot size, although this diminishes the beam's intensity (b2 versus b3) [90].

Field-emission guns (FEGs) and thermionic sources are two types of electron sources. During a thermonuclear reaction, electrons escape when their energy overcomes a natural barrier (work function) preventing their escape [89]. Tungsten and lanthanum hexaboride (LaB6) do not melt at the temperature at which electrons escape. Tungsten wire functions similarly to a traditional light bulb in its V-shaped shape. More electrons are produced when more energy is applied to these materials, but their lifespan is shortened. Although tungsten-wire sources perform poorly, they are cheap in material and maintenance costs and do not require a particular operating environment (e.g., vacuum). In addition to having a smaller tip radius (r), LaB6 cathodes have a low work function, which results in better coherence and higher brightness. FEG's working principle is based on the increased electric field at sharp points. As an emitter, tungsten is used in cold field emission guns (FEG) for its ability to be shaped into very sharp tips. In Schottky FEG, the tungsten is coated with zirconium oxide to reduce the energy barrier and heated to overcome it. The FEGs need a vacuum because emissions are only possible without any contamination at the source. In cold field emission guns, gas adherence to the tip increases the work function, leading to a gradual decrease in electron current and reduced stability compared to heated sources. Regular heating is required to maintain the tip's cleanliness and compensate for the diminished current. Due to their superior coherence and brightness, cold FEGs are currently the preferred choice compared to Schottky FEGs [93, 94]. With increasing operating voltage, brightness increases while contrast decreases, which leads to a trade-off between brightness and contrast. As the voltage increases, the number of electron interactions decreases, resulting in a larger mean free path for electrons. Increasing the accelerating voltage makes it possible to image thicker soft-matter samples, allowing transmission microscopy to penetrate thicker objects. By using higher voltages, radiation damage is reduced, and wavelengths are shorter, resulting in higher resolution [95]. The probability of multiple scattering events decreases with higher electron energy and depends on specimen thickness. The highest possible accelerating voltage is not always desirable. Contrast may be more advantageous for some samples than resolution. In some cases, more contrast is seen in the imaging at a lower acceleration voltage for a particular sample. Therefore, we can ignore the increased radiation damage and the lack of temporally coherent beam sources [96].

Electromagnetic Lenses

Electromagnetic lenses are arranged along the optical axis of the electron microscope (Figure *3*). Two or more condenser lenses are positioned below the electron source to regulate the spot size and intensity. They produce a demagnified image of the beam's crossover and help control the beam's shape. An objective lens is located beneath the condenser lenses. A TEM typically consists of an objective twin lens, which is made up of two electromagnetic fields. Above the sample is an objective lens that provides extra control over the beam, and below the sample is an objective lens that magnifies the image approximately 50 times. The beam passes through the diffraction lens after passing through the objective lens. During diffraction modes, the diffraction lens is weakened, resulting in an image of the diffraction pattern of the specimen, which is reflected from the back focal plane of the objective lens. A series of magnifying lenses are located below the diffraction lens to magnify the intermediate image.

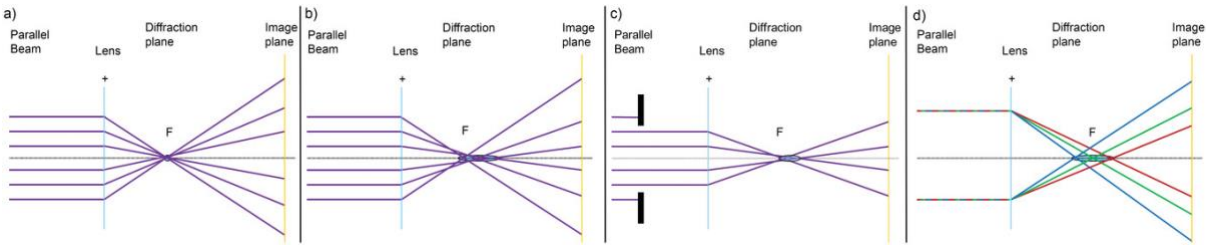

Figure 5: Electromagnetic lenses have spherical and chromatic aberration. a) In a perfect lens, there is a focal point (F). b) The cause of spherical aberration is that electrons passing through the lens are subjected to stronger electromagnetic fields when passing closer to the coil than through the lens center, forming a focal area rather than a focal point. c) This area can be reduced by using a C2 aperture. d) As electron speed varies, chromatic aberration occurs. Slower electrons (blue) will be more focused than faster (red) [90].

There are three types of aberrations in electromagnetic lenses (Figure *5*): spherical aberration (Cs), chromatic aberration (Cc), and astigmatism. Condenser lenses, which determine beam quality, and objective lenses, which magnify all aberrations several thousand times, can significantly reduce image quality. Electrons passing closer to the center of an electromagnetic field will be exposed to a weaker force than ones passing closer to the coils (Figure *5*b), resulting in spherical aberration.

To eliminate aberrations in TEM, microscopes introduce some opening angles that reduce the maximum resolution possible. TEM images are illuminated parallel to the optical axis (coma-free alignment) to avoid an uneven rotational contribution from the objective lens (coma). The Cs effect can be eliminated using a Cs corrector, a multipole lens that produces negative spherical aberration. It is also possible to reduce the Cs effect by taking a smaller C2 aperture (Figure 5c) [97-99]. In Figure 5d, chromatic aberration is caused by not all electrons moving through the lens at the same speed. An electron moving at a faster speed is less affected by the lens' current than an electron moving at a slower speed. Due to inelastic scattering, one can use a monochromator and an energy filter to remove electrons with a wavelength different from what they should be. Electrons are sorted by their energy using an energy filter. A pinhole then selects those with zero losses (electrons that did not transfer energy to the sample) or specific losses. By removing inelastic scattered electrons, an energy filter improves the signal-to-noise ratio. Astigmatism arises when the strength of the lens varies in the x and y directions. Due to stigmatism in the condenser lenses, there is an oval-shaped beam. In the objective lenses, astigmatism causes a difference in focusing strength between the x and y directions. It is possible to correct astigmatism before imaging on all microscopes. However, an image's astigmatism can be corrected computationally if it is relatively small. However, more severe levels can also result in magnification variations that are much more challenging to correct.

Specimen

High vacuum and intense radiation significantly impact sample preparation. It is important to consider this when interpreting images, as preparation procedures often alter the natural state of the specimen. There is better contrast in dry samples containing heavy metals because they are less sensitive to radiation damage. The drying of hard materials is suitable for TEM because they are often independent of solvents. However, organic and soft matter materials need to be preserved. It is essential to consider the contrast, achievable resolution, and natural state of the sample when selecting a suitable sample preparation procedure and deciding whether or not to use heavy metals [100].
Cryo and negative staining are currently the most common methods for studying samples in soft matter chemistry. The staining process also helps fix the sample shape, enhance contrast, and prevent some damage caused by dehydration and radiation. Adding metals that adhere to specific parts of the sample results in a positive heavy metal stain. Negative stains consist of fine-grained metal solutions that cover and surround the sample [101]. The result is that light objects of interest are surrounded by a dark halo caused by staining by heavy metals. There are several disadvantages to negative stain preparations. The image shows the stain-excluding surface, which obscures interior features. Staining requires sample support, limiting the orientations that can be observed. Additionally, the grain size of the stain restricts the achievable resolution, and the specimens undergo significant dehydration during processing.

The most effective preservation technique is generally considered to be cryo-fixation. It involves applying a sample drop to a grid of carbon or gold-coated holes and blotting the sample to leave a thin solution within the holes. Liquid ethane or ethane/propane is then used to freeze the grid. As a result of this rapid freezing step, vitreous (glass-like) ice is produced, preventing the formation of damaging ice crystals. The thickness of the specimen will have an impact on cryopreservation. The thickness of the ice sample should not exceed 100 nm for single-particle cryo-EM to prevent electron multiple scattering. The ice thickness cannot generally be smaller than the particle size, typically 10-30 nm [102]. In vitrified soft matter specimens, cryo-EM gives minimal contrast, requiring phase

contrast. However, it is the most effective method of reaching high resolution in imaging and image processing when the sample is in its native state.

Detector

Another component of the electron microscope that can impact image quality is the detector positioned in the image plane. In the past, images were recorded on film, which provided an acceptable level of sample details. However, there are disadvantages, such as the large amount of work associated with it. As a result, many images could not be processed, and instant feedback was impossible for most automated data acquisition processes. A slow-scan CCD camera provides lower-quality images but can automatically capture many images. The CCD camera indirectly records electrons by translating them into photons using a scintillator layer. Due to the thickness of the scintillator layer (resulting from multiple scattering) and the spread of light caused by the incident electron, the image blurs. There is a trade-off between sensitivity and local precision when the scintillator layer is thicker. CCD cameras were the most common type of cameras until a decade ago. Their maximum resolution was limited by their sensitivity and the mechanical stability of the sample stage. To achieve a sufficient signal, we needed to account for the beam-induced motion of the sample and use long exposure times.

Proteins are irreversibly damaged by high-energy electrons used in imaging. Thus, the overall electron dose is limited in cryo-EM micrographs, resulting in high noise and a low signal-to-noise ratio (SNR). Alignment and averaging are two steps in the process of reconstructing the 3D structure of a protein. When the SNR of the cryo-EM image is high, the alignment accuracy improves, resulting in better achievable resolution in cryo-EM 3D volume reconstruction.

Cryo-EM images show a correlation between scattered photons and protein size. Small proteins scatter fewer electrons, resulting in weak signals, low signal-to-noise ratios, and inaccurate alignment. Reconstructing small proteins becomes more challenging as the signal-to-noise ratio decreases. Improving the SNR of cryo-EM images is crucial for enhancing final resolution and remains a prominent

topic in cryo-EM research. Since 2013, direct detection devices (DDDs) have significantly improved cryo-EM's capability to resolve 3D structures of proteins. Compared to charge-coupled devices (CCDs) and films, the DDD has a higher frame rate and better detective quantum efficiency (DQE), enabling cryo-EM images to be recorded with a higher signal-to-noise ratio, leading to improved resolution. Electrons scattered by an atom have a negative correlation with their energy. Consequently, electrons with lower acceleration voltages yield more signals when interacting with cryo-EM specimens. Low-energy electrons cause increased radiation damage, leading to fewer electrons for imaging, potentially compromising a cryo-EM image's overall signal-to-noise ratio. For cryo-EM images, DDD cameras are currently available to detect electrons at a voltage of 300 kV. A decrease in acceleration voltage results in a reduction of their DQE. It has been possible to determine the electron's position entering the camera and to normalize the intensity of the electron using counting algorithms. For each signal, some DDD cameras calculate the center of mass/gravity to determine the position of the incident electron using a counting algorithm. It has been demonstrated that this position is often accurate to a subpixel level. The center of the mass position may deviate from the actual incident position if the incident electron is backscattered or interacts with multiple pixels [103].

Image Formation

The sample in electron microscopy acts like a grating, allowing most electrons to pass through without absorption. It is the interference of waves that produces a TEM image. Interference between waves occurs when two or more waves reach each other [104]. According to the phase of the electron waves, interference can be constructive or destructive (Figure *6*).

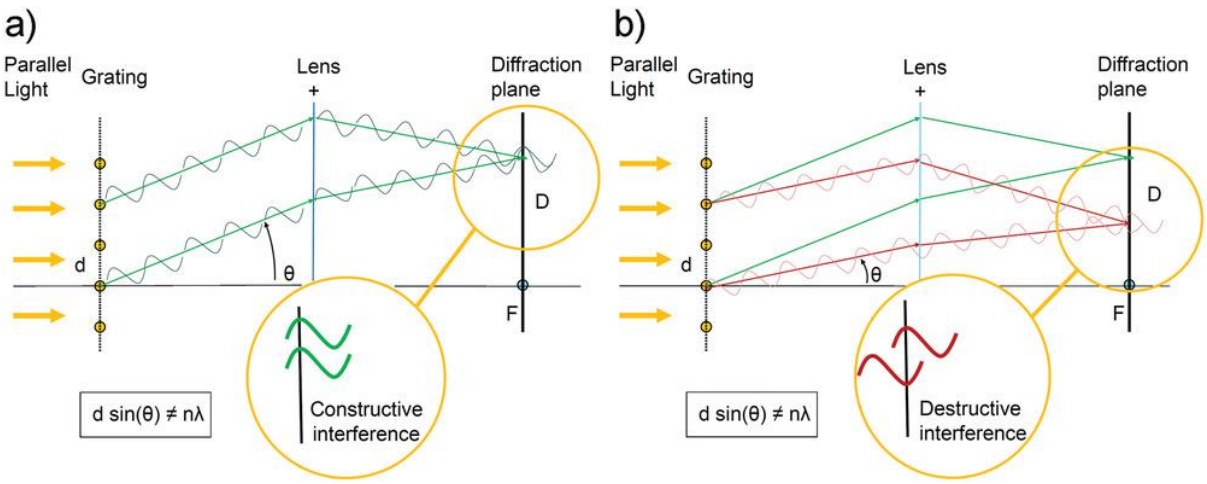

Figure 6: Constructive and destructive interference. A lens' back-focal plane is the diffraction plane, where parallel scattered waves interact. When they reach each other, the phase between waves determines how their amplitudes are added. Constructive interference results in an intensity peak when the interfering waves are in phase. The intensity peak occurs at scattering angles where the difference in path lengths between the two phases is nλ (a vs. b). An image of positive wave interference shows a magnified reciprocal distance between events (D). A smaller detail requires a larger scattering angle and a larger D value. The diffraction plane sorts the information from the grating (specimen) according to size, with the smallest details the furthest out [90].

The process can be visualized by shining a laser on a grid of regularly spaced gratings, such as a TEM grid, and placing a screen at a distance from the gratings. The Fraunhofer grating formula defines the diffraction pattern in the back focal plane as an image:

$$d \sin \theta = n\lambda$$

The wavelength of the source, spacing in the grating, and scattering angle of the wave from the sample relative to the source direction are indicated by λ, *d, and* θ. To achieve positive interference according to the grating formula, certain conditions must be satisfied. Because the particles of the samples are located at different distances from each other, (d) could be a very different number than the regular spacing determined by the grid mesh. Combined with the grating formula, the scattering angle must be larger when d is smaller. This is to have positive interference and for all parallel scattered waves to reach each other at the back focal plane of the lens. As a result, all information in the sample is sorted by

frequency (1/d), with higher frequencies closer to the optical axis and smaller frequencies farther away.

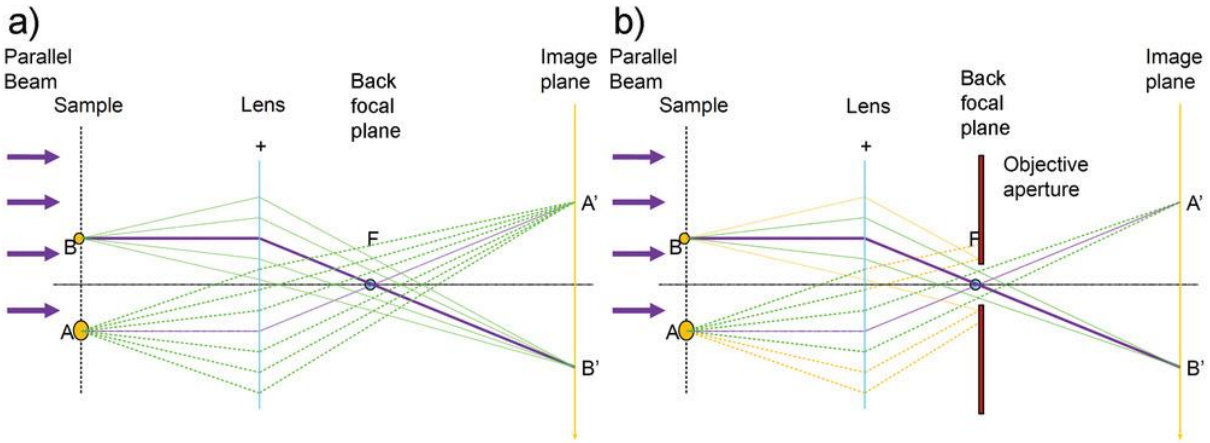

Figure 7: Electron microscope scattering contrast. As the beam passes through thin samples without interacting with particles, the purple lines show unscattered beams, whereas the green lines show scattered beams. As the scattered electrons interfere in the back-focal plane (F), the unscattered beam is separated from the scattered beam. a) Scattered and unscattered electrons interfere in the image plane. b) The objective aperture is positioned at the back focal plane, removing the highly scattered beams and preventing them from reaching the image plane [90].

Since scattered and unscattered electrons are separated in the back focal plane, a diffraction pattern does not contain structural phase information. The coherency of the incoming beam is the only factor that affects the diffraction pattern. The interference of scattered and unscattered beams results in the formation of the image plane, which consists of information such as intensity, spherical aberrations in the lenses, focusing, and beam-induced drift.

To determine the energy differences in the scattered electron, we must consider two types of scattering: elastic and inelastic. There is no energy transfer during elastic scattering, only a wide distribution of angular angles, resulting in high-resolution information. A low-resolution background with a narrow scattering distribution is produced by inelastic scattering, which involves energy transfer [105]. The wave-optical picture shows a phase shift $\varphi(r)$ in the incoming wave

traveling in the z-direction caused by the elastic scattering of electrons by the object:

$$\varphi(r) = \int C(\boldsymbol{r}, z)\mathrm{d}z$$

Where ***r***(x,y) represents a vector in 2D space and C(**r**,z) represents the Coulomb potential distribution within the object in 3D space (Figure *8*).

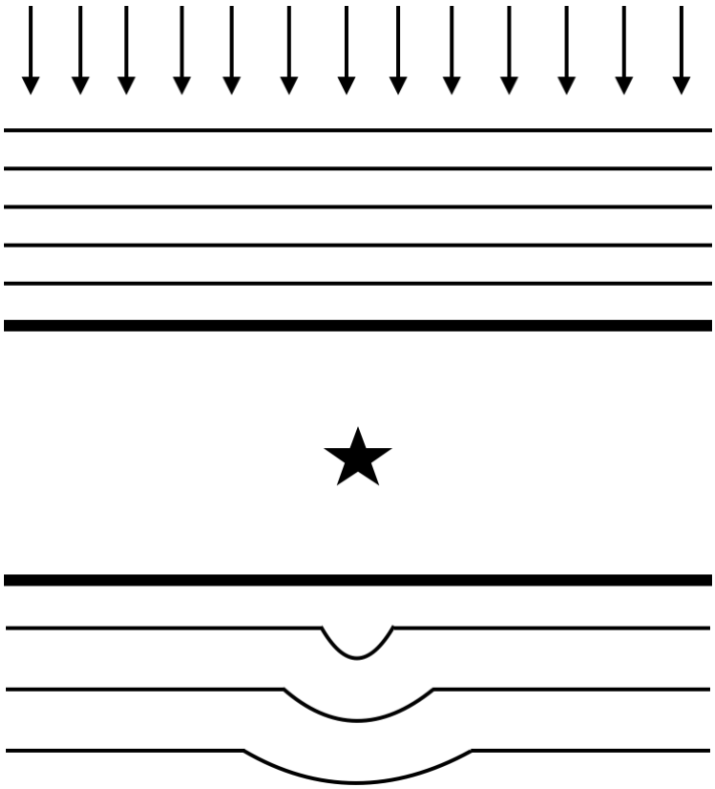

Figure 8: An object (within another medium like ice) in the path of an incoming plane wave causes a phase shift. Upon arrival of an incoming wave, the phase is shifted by a factor proportional to the integral of the potential distribution in the propagation direction. Unlike x and y, the incoming wave is uniformly shifted in the Z direction. Upon exiting the medium, the wavefront is deformed by the wave shift proportional to the object's thickness. In a weak-phase object, the shift is much smaller than the wavelength [105].

Consequently, the wave function $\psi_0 = \exp(ikz)$ will be modified to:

$$\psi(\boldsymbol{r}) = \psi_0 \, exp[i\varphi(r)]$$

The formulation can be expanded if the phase is so weak $\varphi(r) \ll 1$:

$$\psi(\boldsymbol{r}) = \psi_0 \left[1 + i\varphi(r) - \frac{1}{2}\,\varphi(r)^2 + \cdots\right]$$

Based on this formulation, the wave is decomposed into the unscattered wave in the first term, the scattered wave in the second term, and after that ($i\varphi(r)$ and following). In the image mode of a transmission electron microscope, it is assumed that the observation was taken close to the optical axis and far from the object, so the Fraunhofer approximation to diffraction theory (Goodman, 1968) is applied. Fraunhofer has proposed that in the back focal plane of the objective lens, the wave function represents the Fourier transform of the scattered and unscattered wave functions. Because of lens aberrations and defocusing, the scattered wave's phase is shifted by an amount expressed by the following expression:

$$\gamma(\mathbf{k}) = 2\pi\chi(\mathbf{k})$$

In polar coordinates, wave aberration $\chi(\mathbf{k})$ and spatial frequency $\mathbf{k} = \left(k_x, k_y\right)$ are as follows:

$$k = |\mathbf{k}| \quad , \quad \phi = a\tan(k_x, k_y)$$

$$\chi(k, \phi) = -\frac{1}{2}\,\lambda\left[\Delta z + \frac{z_a}{2}\sin 2(\phi - \phi_0)\right]k^2 + \frac{1}{4}\lambda^3 C_s k^4$$

Electron wavelengths are represented by λ, defocus of the objective lens is represented by Δz, focal differences because of axial astigmatism are represented by z_a, reference angles for azimuthal astigmatism are defined by ϕ_0, and third-order spherical aberration constants by C_s.

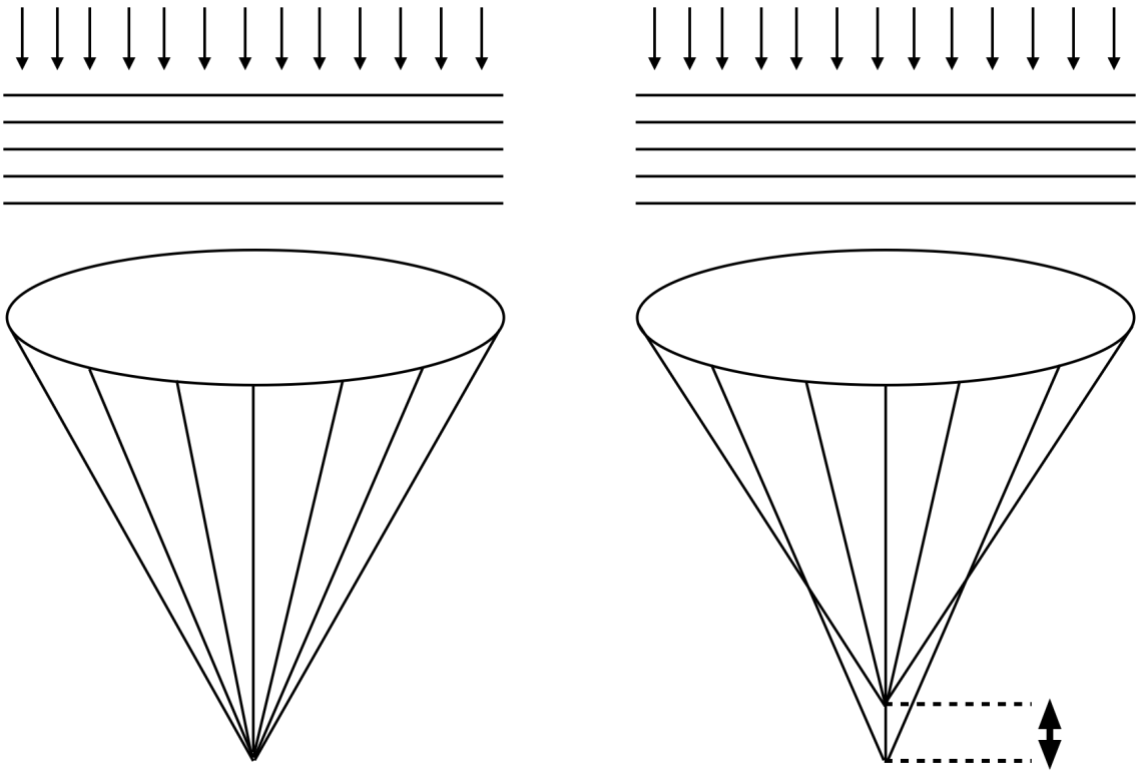

Figure 9: Wave fronts are affected by spherical aberrations. In the ideal case, C_s=0, the incoming wave converts into a spherical wave that converges in the focal plane. If the amount of C_s is small, the focal length for the peripheral regions of the lens is shorter than for the central regions; therefore, the parts of the plane wave intersecting the periphery are focused at a point closer to the lens [105].

When a lens is ideally designed, incoming plane waves are transformed into spherical wavefronts (Figure *9*, left) that converge at a single point on the back focal plane. Due to the spherical aberration term, the outer zones of the wavefront are curved more strongly than the inner zones, resulting in a decrease in focal length (Figure *9*, right).

Due to lens aberrations, the wave function at the back focal plane of the objective lens is derived from the Fourier transform of the wave function multiplied by a phase shift term:

$$\psi_{bf}(\mathbf{k}) = \mathcal{F}\{\psi(\mathbf{k})\} exp[i\gamma(\mathbf{k})]$$

By inverse Fourier transformation, we can obtain the wave function in the image plane from the wave function in the back focal plane. It is also necessary to consider the aperture function A(k).

$$\psi_i(\mathbf{r}) = \mathcal{F}^{-1}\{\mathcal{F}\{\psi'(\mathbf{k})\} A(\mathbf{k}) exp[i\gamma(\mathbf{k})]\}$$

$$A(\mathbf{k}) = \begin{cases} 1 : \text{ for } |k| = {}^{\theta}/_{\lambda} \leq {}^{\theta_1}/_{\lambda} \\ 0 : \text{elsewhere} \end{cases}$$

Depending on the objective aperture radius, angle θ_1 corresponds to the angle of the objective. Lastly, the image plane shows the following intensity distribution:

$$I(\mathbf{r}) = |\psi_i(\mathbf{r})|^2$$

In the extension of the wave equation $\psi(\boldsymbol{r})$, if we only consider the first two terms, the intensity combines the scattered and unscattered beams. Both terms are used in bright field electron microscopy, whereas in dark field electron microscopy, the unscattered beam is blocked at the back focal plane.

Scattering and phase contrasts make it possible to distinguish particles from the background. When an aperture is placed in the back focal plane of an objective lens, the electrons scattered at large angles are removed to produce scattering contrast. As a result, they are prevented from recombining with unscattered electrons (Figure *7*). Due to the higher scattering strength of heavy atoms, their images will appear darker than those of lighter atoms (lower atomic number), like in biological samples. As a result of recombining scattered and unscattered electrons at the image plane, imaging of soft matter samples in focus produces almost no contrast (Figure *10*). There is no contrast because the unscattered waves have a large amplitude, and the scattered waves have a small amplitude. In addition, there is a phase difference in the image plane, approximately 0.25λ. As a result of both factors, it is impossible to distinguish between constructive and destructive interference. Phase contrast allows us to overcome these limitations by defocusing the image. Even though applying defocus blurs the image, phase shifting with increasing frequency can increase the contrast, thereby creating frequency-dependent interferences. The objective lens's spherical aberration (Cs) is a second source of phase shift. We can determine the phase contrast transfer function (CTF) based on the Fourier transform of the image at the image plane and compare it with the actual diffraction at the objective plane:

$$CTF(k) = \sin\big(\gamma(k)\big) = \sin\left[2\pi\left(-\frac{1}{2}\Delta z\lambda k^2 + \frac{1}{4}C_s\lambda^3 k^4\right)\right]$$

$\gamma(k)$ refers to the total phase shift caused by spherical aberration and applied defocus, k refers to the spatial frequency, and Δz refers to the amount of applied defocus (nm).

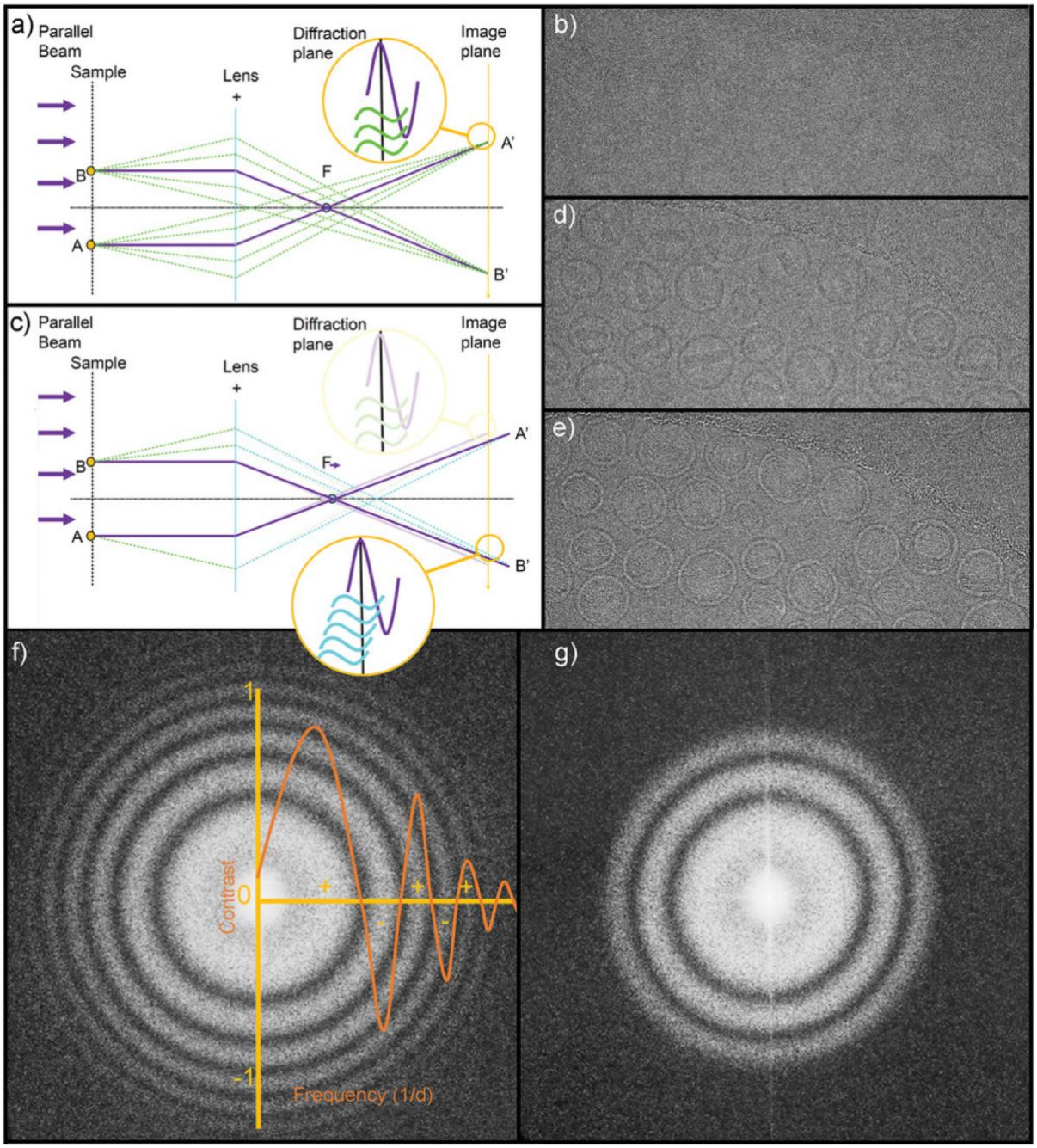

Figure 10: Phase Contrast in Electron Microscopy: An Exploration of Techniques and Their Impact on Image Quality. a) Challenges in Achieving Contrast: When scattering angles are too small for effective removal by an aperture without compromising resolution, an in-focus image may lack contrast as the scattered and unscattered beams recombine. b) In-Focus Imaging Limitations: The absence of contrast in in-focus images, where the recombination of scattered information with the unscattered beam occurs. c) Phase Delay in Out-of-Focus Imaging: Scattered waves experience delayed phases due to varying scattering

angles and corresponding electron path lengths, leading to frequency-dependent phase shifts. This not only blurs out-of-focus images but also introduces per-frequency phase alterations. The impact of defocusing on contrast is exemplified using cryo-EM images (Titan Krios, 300 keV, FEG, Ceta-camera) of Doxil, an anticancer drug composed of liposome-encapsulated doxorubicin hydrochloride crystals: (b) in-focus, (d) under focus, and (e) over-focus images display varying contrast across different frequencies. (f) Fourier Transform Analysis: Analyzing the Fourier Transform (FT) of an image reveals the contrast intensity sorted by frequency, highlighting the influences of the Contrast Transfer Function (CTF, indicated by the orange line) and the limitations imposed by temporal and spatial coherence (evident as reduced signal intensity at higher frequencies). (g) Aperture Size and Frequency Information: A comparison of images taken with 100 µm and 30 µm apertures shows the latter's inability to capture high-frequency information (visible as outer rings in FT), emphasizing the importance of appropriate aperture selection [90].

Single Particle Analysis and Data Processing

The use of TEM for biological specimens poses a significant challenge due to the fragile nature of these samples. Although TEM is more effective for atomic-scale imaging of inorganic substances, its application to biological samples is challenging. These specimens are highly susceptible to radiation damage and are often destroyed by the electron beam used for imaging. To address this issue, imaging could potentially use lower electron doses. However, biological molecules are primarily made up of elements with low atomic numbers, resulting in weak electron scattering. As a result, this leads to the creation of images with low signal-to-noise ratios and inadequate contrast. It is common to treat samples with fixatives and stains to preserve the structure and enhance the contrast. Negative staining is a widely used technique for examining purified biological macromolecules. This method involves coating the particles with a dense metal salt, such as uranyl acetate, to effectively form a protective layer around them. Once the samples are dried and stained, they become more resistant to radiation, yield higher contrast, and are better suited to the vacuum conditions of the TEM instrument's column. However, the resulting images mainly show the heavy metal stain rather than the biological particle. Additionally, staining and drying processes may distort the natural shapes and structures of the samples,

potentially leading to misinterpretations. Negative stain TEM is suitable for illustrating the overall structure of biological samples but does not offer high-resolution details, requiring more advanced imaging methods for clearer images.

1975 Richard Henderson and Nigel Unwin published a 7Å resolution structure of bacteriorhodopsin using TEM, revealing its transmembrane α-helices [106]. They enhanced electron crystallography by capturing electron micrographs and diffraction patterns from unstained 2D protein crystals, a technique first demonstrated by David De Rosier and Aaron Klug, who were awarded the Nobel Prize in 1982 [107]. Although the achievable resolution compared to X-ray crystallography is lower, Henderson in 1990 achieved a 3.5 Å cryo-EM map of bacteriorhodopsin, demonstrating TEM's potential for atomic-level biological imaging [108]. Henderson's work achieved high resolution, but it was still unclear whether such high-resolution TEM could be applied to diverse biological samples. That uncertainty was due to the challenges in forming 2D crystals and capturing high-quality data from tilted specimens. In the 1970s, Joachim Frank developed a method for generating 3D reconstructions from low-dose, noisy TEM images of randomly oriented particles [109]. This established the foundation for what we now recognize as single-particle analysis, with crucial concepts subsequently validated through additional research. The process starts by computationally aligning particle images through cross-correlation, which enhances the signal-to-noise ratio and reveals finer details by averaging the aligned images. Frank and Marin van Heel later introduced multivariate statistical methods to classify particles into classes that reflect their various structural forms [110]. Following the initial alignment, the next step involves determining the spatial orientations of all 2D projections. The information is then used in a back-projection technique to create the 3D reconstruction. Frank and his team successfully used these methods to reconstruct the asymmetric structure of the negatively stained bacterial ribosome [111]. To maintain the biological integrity of molecules for TEM imaging, it is crucial to keep them hydrated. This can be challenging within the vacuum of the microscope. While Henderson used a glucose solution to hydrate 2D crystals, this approach was ineffective for single particles. The alternative, cryo-cooling, initially resulted in disruptive ice crystal formation in the images. In the 1970s, Kenneth Taylor and Robert Glaeser managed to overcome this challenge by capturing clear diffraction patterns of catalase crystals in a frozen

state without the interference of ice crystals [112]. Taylor and Glaeser's research demonstrated that cryo-cooling can protect against radiation damage. This method could enhance image contrast and led to the development of cryo-EM techniques. They aimed to rapidly freeze samples to avoid crystalline ice and preserve them in a glassy state known as vitreous ice. In 1981, Jacques Dubochet and Alasdair McDowall successfully created vitrified ice suitable for TEM analysis [113]. Dubochet and his team later revealed the first cryo-EM image of viruses suspended in vitreous ice, confirming their technique's ability to visualize biological molecules in their natural, hydrated form [17]. They also developed a vitrification method, which is still considered the best technique for cryo-EM sample preparation [114]. The work by Nobel winners and other pioneers developed the cryo-EM method and it is used for high-resolution structural analysis. This enabled the 3D reconstruction of various hydrated particles at a high resolution, highlighting the combined contributions of Dubochet, Frank, and Henderson [115]. In recent years, there has been a significant increase in the use of electron microscopy in structural biology, particularly SPA, highlighting the crucial role of cryo-EM. Advances in detector technologies, improved image processing, and the ability to study biological structures at near-atomic detail without crystallization overcome a limitation of X-ray crystallography. Cryo-EM's ability to visualize proteins and complex molecules in their natural states is revolutionizing drug discovery by informing the design of more effective therapeutics. Furthermore, its capability to visualize molecules in various configurations offers dynamic insights into biological mechanisms. Cryo-EM's increasing impact on current research and publications has the potential to deepen our understanding of molecules and lead to advancements in medical applications.

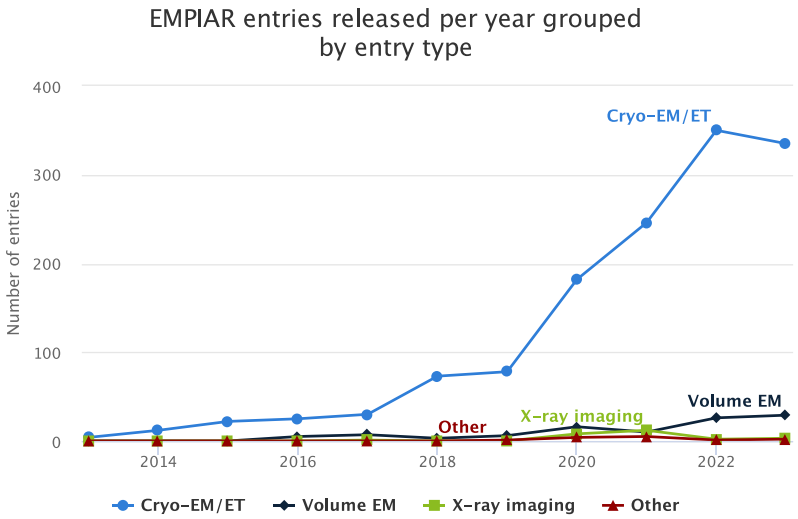

Figure 11: From 2013 to 2023, the EMPIAR database entries showed an annual increase, with Cryo-EM/ET submissions experiencing the most growth, while volume EM, X-ray imaging, and other techniques demonstrated stable trends.

Single-particle analysis in cryo-EM involves vital steps, such as motion correction, correcting lens aberrations, locating particle coordinates, classifying particles in 2D and 3D, initializing and refining structures, determining resolution, and interpreting 3D maps. Advancements in software developed over decades continue to enhance this process. The capabilities of cryo-EM have been further improved with the introduction of direct detectors and movie-mode data collection. These allowed for near-atomic resolution reconstruction using software like RELION, which utilizes robust algorithms like maximum likelihood [116]. Using direct electron detectors with high frame rates, which can record images as subframes in single-particle cryo-electron microscopy, has enabled atomic-resolution imaging of macromolecules. Correcting beam-induced motion blurring involves aligning and combining subframes to create a clear image. MotionCor2 is a software tool that corrects uniform and varied motion across the image. It utilizes a model of smooth local motion deformations, verified by tilt experiments, and applies a dynamic 2D polynomial function for motion correction. MotionCor2 software divides the image into patches for precise motion tracking and adjustment. The software goes through global frames and intricate local motions and conducts vital preprocessing tasks such as detecting and repairing faulty pixels before the standard cryo-EM processing [117].

Accurate Contrast Transfer Function (CTF) estimation is crucial for evaluating micrograph quality and determining structures. Essential parameters for CTF estimation include acceleration voltage, spherical aberration, defocus, astigmatism, and amplitude contrast, typically assumed to be 5-10% for cryo-EM images. Voltage and spherical aberration are fixed parameters of the TEM. More accurate measurements of defocus and astigmatism are obtained by aligning calculated CTF patterns with Thon rings in the image spectrum. After setting the CTF parameters, correcting CTF distortions is possible, especially when multiple defocused views of particles are available. This correction can address both amplitude and phase distortions and offers the option for phase-only correction, known as phase flipping. Additionally, the resulting 3D structure must be adjusted for envelope functions that reduce high-frequency details because of microscopy system limitations and particle orientation inaccuracies [118].

During the 3D reconstruction process, accurate particle picking is crucial for identifying the positions of particles in micrographs. It requires precision and speed to distinguish between particle states and potential contaminants. Traditional particle picking relies on template matching and specific feature identification, methods such as FindEM [119], Signature [120], DoGpicker [121], gAutoMatch, and routines in EMAN [122] and RELION [116], where users must provide templates or feature descriptions. These methods can be biased and highly dependent on user expertise. In contrast, deep learning approaches, notably convolutional neural networks (CNNs), offer a more adaptive and automated solution. These methods, including DeepPicker [123] and subsequent developments like DeepEM [124], Warp [125], Topaz [126], and crYOLO [127], use CNNs' ability to generalize particle-picking tasks across diverse datasets, learning complex feature sets autonomously [128].

Refining the 2D image dataset involves aligning images and organizing them into uniform groups, which is crucial in the initial phase of single-particle EM structure analysis. 2D classification is useful for removing artifacts, invalid particles, or blanks. It also deals with the unknown particles' angular distribution, which is essential for 3D analysis. The other benefit of 2D classification is that it provides the high-SNR data required for ab initio 3D structure determination, found in

quality class averages. Alignment and clustering in single-particle EM image datasets typically rely on variations of the K-means clustering algorithm. The basic form of this in EM analysis is a 2D Multi-Reference Alignment [129], where images are matched to the closest of K initial reference images through an iterative process that refines the references over time. This procedure is included in most EM software. It is often combined with the Principal Component Analysis [105] to enhance the speed and accuracy by clustering based on reduced data dimensions.

Ab initio 3D structure determination is essential when no existing structural templates can guide the process. To have a reliable 3D structure and to speed up and improve the refinement procedure, it is necessary not to start from a distorted and not completely different or noisy initial model. In some cases, low-resolution models or maps, or starting from a random point, can also help reconstruct highly symmetric structures. However, it's always best to conduct comprehensive analysis and validation procedures to ensure accurate results. Ab initio methods are divided into experimental techniques, such as tilt-pair analysis and computational methods that rely on data from untilted samples. The Variable-metric Gradient Descent with Adaptive Moments estimation (VDAM) algorithm within RELION software is an initial 3D model generation method. It evaluates the model by iterative refinement and validation against a known structure. It operates by dividing particle sets into classes, refining them over iterations, and using the most representative class for further refinement. The rate of successfully building an initial model is different due to the specific dataset challenges, such as particle heterogeneity and alignment issues [130].

Refining an initial structural map to a detailed final map involves using a 3D projection matching technique. This technique adjusts the orientations of particle images to better align with the structure of the current model projections. The refinement techniques in SPA vary between software packages and depend on user influences and parameter specifications. The refinement process and quality can be monitored using various metrics, specifically the Fourier Shell Correlation (FSC) curve. The FSC curve shows the signal-to-noise ratio (SNR) across spatial frequencies, reflecting the map's resolution [131]. To generate the FSC curve, the particle image dataset is divided in half to create two volumes. The Fourier

transforms of two independently reconstructed are used to calculate the FSC curve. Fourier space can be visualized using shells that show spatial frequencies or resolutions. The correlation coefficient of each map is calculated within each spherical shell. In the FSC cure, the x-axis represents the spatial frequency, and the y-axis represents the correlation coefficient. The point where FSC falls below a certain threshold indicates the resolution. The benefit of using this method is avoiding independent noise in each half map, which may not be possible using a single map reconstruction. The standard threshold is commonly set at 0.143 to align EM resolution standards with X-ray crystallography standards [132].

Results and Discussions

Designing Rigid DNA Origami

Rigidity With Design Parameters

To enhance the rigidity of DNA origami structures, we used the Cadnano software to adjust essential design parameters. Our research successfully designed three distinct multi-layer DNA origami objects, designated as V1, V2, and V3 (Figure *21*, Figure *22*, and Figure *23*). These DNA origami structures were used as models to investigate improvements in structural rigidity through design modifications. Each construct was folded from a 2873-nucleotide-long single-stranded DNA scaffold (Note 1) into a square lattice configuration. This approach was crucial in achieving our structural goals, especially in enhancing the mechanical stability of the DNA origami structures. To enhance the stability of our DNA origami constructs, we implemented two crucial design adjustments while preserving the overall shape of the test object. The first parameter we modified while preserving the three-dimensional integrity of the DNA origami was the frequency of the crossovers, specifically changing the number of scaffold crossovers. Secondly, we altered the lengths of the staple strands while ensuring their accurate folding and maintaining the intended shape of the DNA origami. (Figure *12*A). These adjustments to the crossover frequency and the length of the staple strands were crucial in strengthening the rigidity and compactness of our structures. Our work illustrates the connection between strategic design choices and the resulting compactness of DNA origami.

The primary difference between V1 and V2 lies in their different distributions of staple strand lengths, as illustrated in Figure *12*B. V1 staples ranging from 40 to 80 nucleotides, with an average length of 67, while V2 utilizes a narrower range of 40 to 60 nucleotides, with a mean length of 54. Moreover, V2 is characterized by more scaffold crossovers than V3, with counts of 138 and 86, respectively. We employed agarose gel electrophoresis to assess the compactness of our DNA

origami designs. Following the earlier self-assembly process, the three variants were analyzed for electrophoretic mobility, as shown in Figure *12*C. The V2 monomer band exhibited higher electrophoretic mobility compared to its counterparts, indicating a denser and more tightly packed structure. While V1 and V2 exhibited similar folding byproducts, V3 was distinguished due to its less byproduct formation.

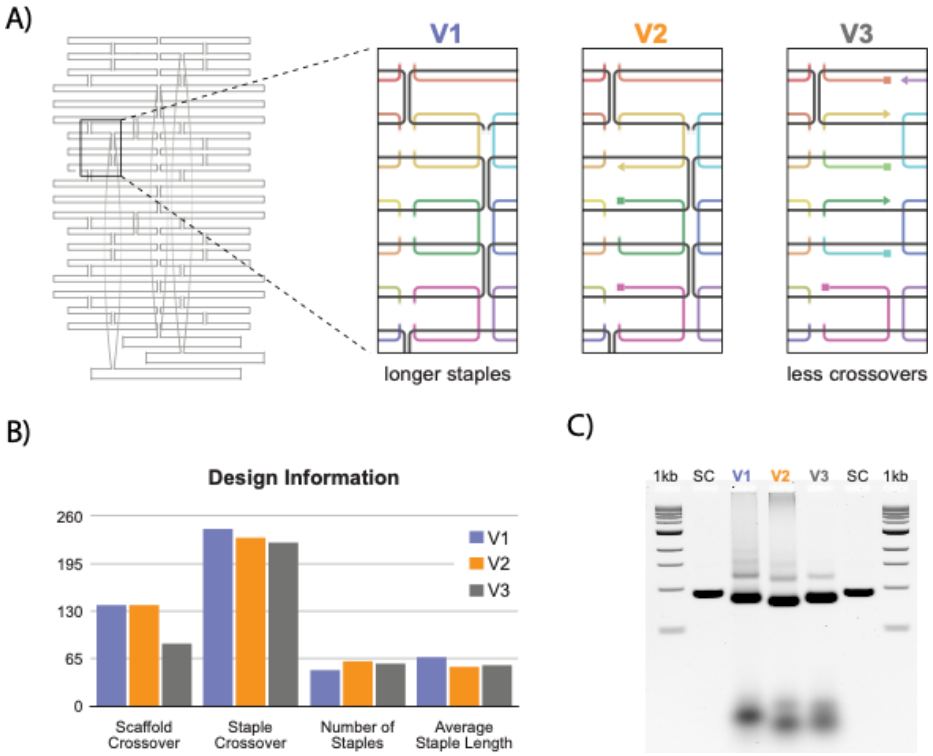

Figure 12: Comparative Design and Analysis of DNA Origami V1, V2, and V3: A) Depicts the scaffold routing for V1 and V3, showing the maintained overall structural shape across all variants, with V3 having an altered number of scaffold crossovers. V1 is noted for having longer staples compared to V2, while V3 is distinguished by a reduced number of scaffold crossovers. B) Provides a statistical diagram detailing the design elements of each version. C) Gel electrophoresis results demonstrate the differences in mobility among V1, V2, and V3 despite their similar overall shapes [133].

In addition to using gel electrophoresis to evaluate the compactness of our DNA origami designs, we utilized cryo-EM SPA. Before preparing for cryo-EM, we initially purified the three DNA origami variants. Since the initial concentration of

the staple strands was four times higher than that of the scaffold, the excess strands were removed through polyethylene glycol (PEG) precipitation. The resulting pellet containing the monomer band and any higher-order structures was resuspended in 1x FOB5 buffer, which was the same buffer selected for cryo-EM TEM imaging. We concentrated the samples using molecular weight cut-off filtration to meet the concentration requirements for cryo-EM SPA. We performed additional agarose gel electrophoresis after concentration to confirm sample purification success (Figure *30*). We utilized negative stain imaging to confirm the structural integrity of the DNA origami. These initial steps were crucial to ensure that the samples were in optimal condition for high-resolution structural analysis by cryo-EM SPA.

All three DNA origami samples were imaged using a 300kV Titan Krios transmission electron microscope, and cryo-EM SPA was utilized to determine the three-dimensional structures of each design variant. Figure *13* presents the cryo-EM experiment data for DNA origami versions V1, V2, and V3. Panel A focuses on Origami V1, Panel B on Origami V2, and Panel C on Origami V3. The sequence in all three panels is as follows from left to right: 2D classification images, 3D reconstructions of the DNA origami displayed in three distinct orientations, and finally, on the far right, the Fourier Shell Correlation (FSC) curves are shown. These curves provide insights into the final resolution achieved for each version. These reconstructions present various perspectives of the DNA origami structures, emphasizing their overall shape and configuration. The achievable resolution allows for identifying interhelical crossovers and distinguishing between each helix's major and minor grooves. Using SPA, the DNA origami structure achieved a resolution of 8.6Å for V1, 7.5Å for V2, and 8.3Å for V3.

In this experiment, we utilized the same imaging equipment, computational analysis tools, and nearly the same number of particles examined. The higher resolution for version 2 suggests a more densely packed and structurally rigid DNA origami construct than versions 1 and 3. The findings suggest that varying the design can enhance the compactness and stability of DNA origami structures, resulting in assemblies with better physical integrity.

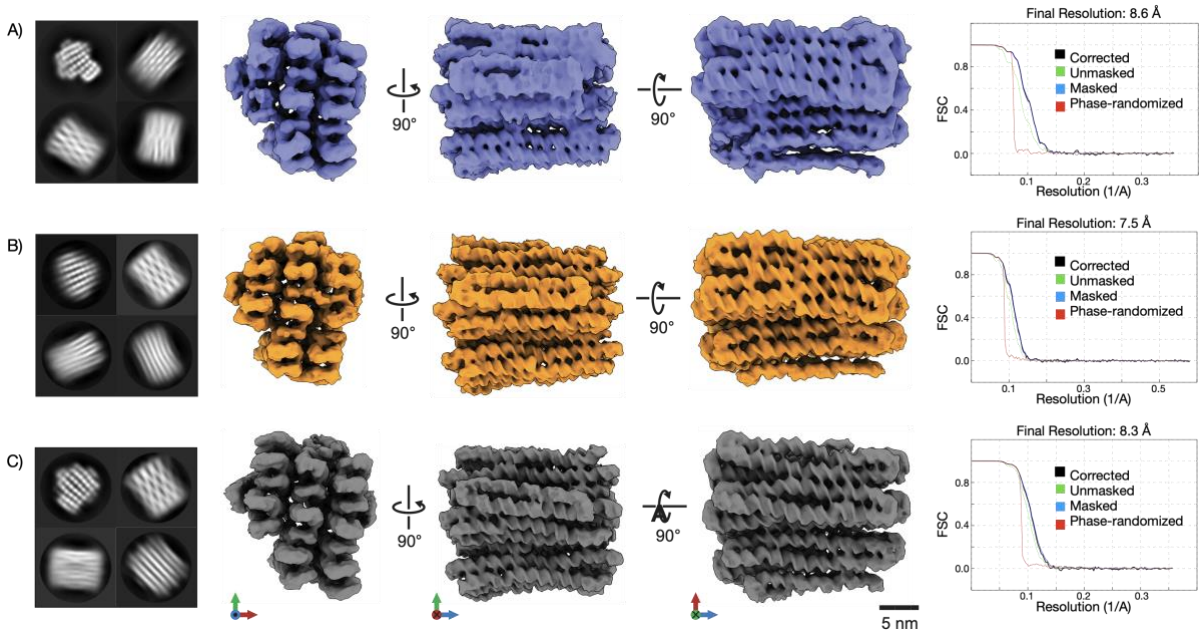

Figure 13: Cryo-EM Characterization of DNA Origami Variants V1, V2, and V3: A) For V1, from right to left, the panels illustrate the 2D classification, the 3D reconstruction, and the Fourier Shell Correlation (FSC) curve indicating a resolution of 8.6Å. B) The sequence for V2, also from right to left, features the 2D classification, 3D reconstruction, and FSC curve, revealing a finer resolution of 7.5Å. C) V3's arrangement from right to left includes the 2D classification, 3D reconstruction, and the corresponding FSC curve with a resolution of 8.3Å [133].

The cryo-EM density maps were superimposed for our comparative analysis of DNA origami structures to compare their compactness in their structural densities. The V2 map showed a denser arrangement, with narrower helical spacing within its lattice, as depicted in Figure *14*A and Figure *14*B. This observation is consistent with previous gel electrophoresis data. V2 exhibited the highest migration speed, suggesting its compact nature. These results confirm that our design changes have successfully increased the structural compactness in V2.

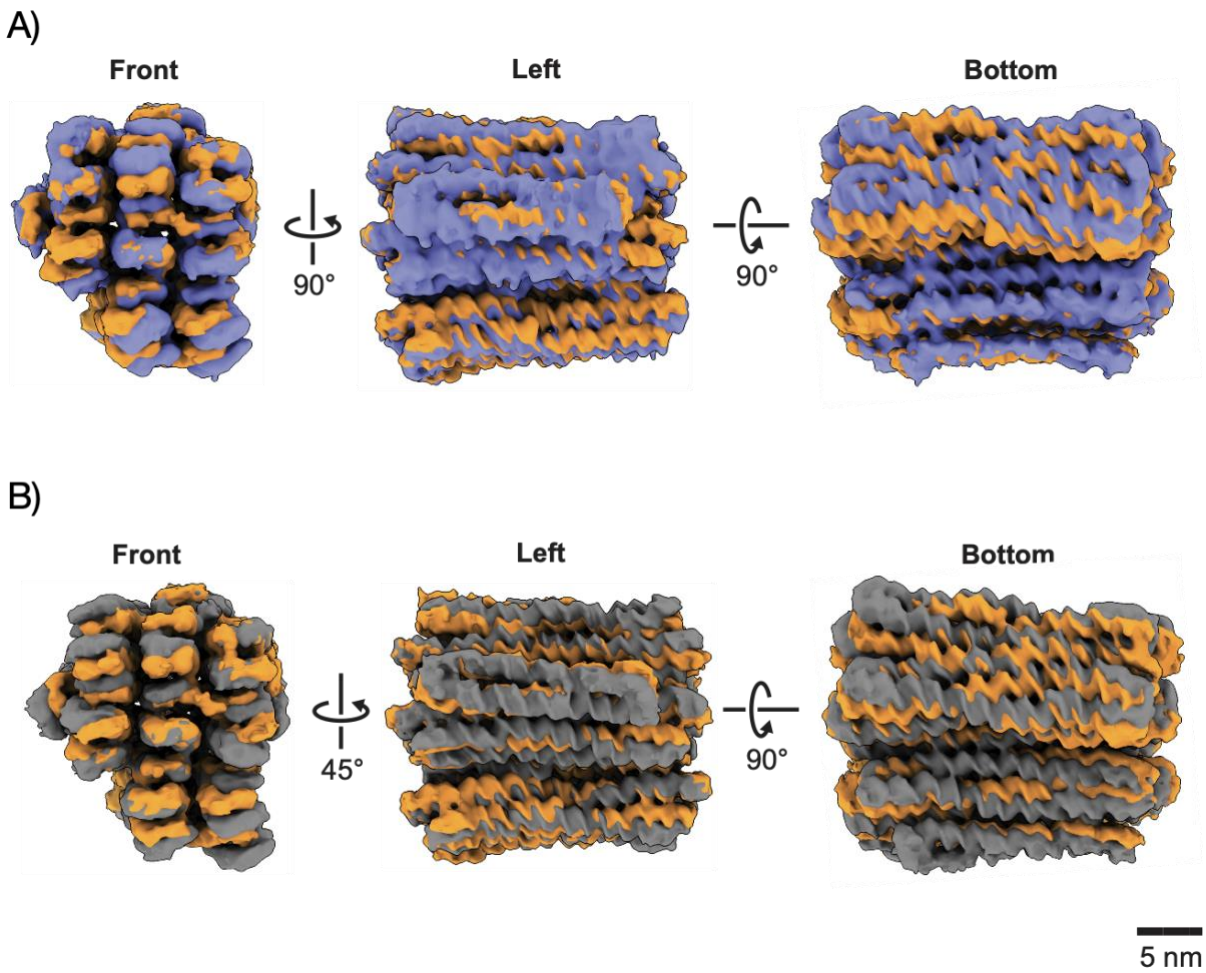

Figure 14: Assessing Structural Density with Fitted Cryo-EM Maps of DNA Origami Versions: A) The superimposed maps of V1 (in purple) and V2 (in orange) are displayed in three distinct orientations to highlight the interhelical distances, illustrating the relative compactness. B) Similarly, the overlay of V2 (in orange) and V3 (in gray) is presented in three orientations, providing a comparative view of the interhelical spacing between these versions [133].

Rigidity by Compositional Homogeneity

Our study investigated how the purity of staple strands affects the structural rigidity of DNA origami constructs. Despite the high precision provided by M13 bacteriophage-derived scaffold strands, chemically synthesized staples (which are essential for DNA origami formation) can introduce imperfections. These flaws often arise during the synthetic process, particularly in the capping stage following the coupling step in DNA oligonucleotide synthesis. After deblocking removes protective groups from the oligo's 5' end, capping prevents incomplete nucleotide addition by terminating unreacted chains. This step could result in structural inconsistencies that might hinder the proper folding of DNA origami.

We used two staple purification methods to evaluate the effect of these synthetic inaccuracies in folding DNA origami structures. In this experiment, we utilized high-performance liquid chromatography (HPLC) and desalting as purification methods. HPLC purification is recognized for its high purification standards, resulting in higher-quality strands with fewer synthetic errors. Desalting may not effectively remove truncated sequences or other erroneous oligonucleotide forms. Our analysis focused on determining how the varying levels of purification affect the assembly and rigidity of the DNA origami. It revealed that higher purity, as achieved by HPLC, is effective for the integrity of these nanostructures.

To investigate the impact of the purification method on the stiffness of DNA origami, we designed origami V4 (Figure *24*). Origami V4 was designed using a square lattice pattern and a scaffold strand of 1033 bases (Note 2). For designing origami V4, we applied the design principles that helped to enhance the compactness of origami V2. To design origami V4, we utilized an average staple length of 58 nucleotides and extensively used scaffold crossovers to enhance the overall structural assembly compactness. We used polyacrylamide gel electrophoresis (PAGE) to analyze five randomly selected staples to compare the purity of different staple strands. The findings are presented in Figure *15*A. The HPLC-purified staples primarily showed a single, clean band, indicating the absence of shorter byproducts and reduced truncation artifacts. The same staples using desalted purification were analyzed using the PAGE gel, and multiple bands were found. These additional bands indicate higher

electrophoretic mobility, suggesting the presence of truncated DNA sequences due to synthesis-related imperfections.

In our investigation of how staple strand purity affects DNA origami structure V4 assembly, we performed folding tests using desalted and HPLC-purified staples. The gel electrophoresis results indicated quality differences. HPLC-purified samples exhibited a distinct, faster, and well-defined DNA monomer band compared to the more diffuse band seen in desalted samples, as shown in Figure *15*B. This implies that the HPLC purification process of staples may enhance the compactness of DNA origami.

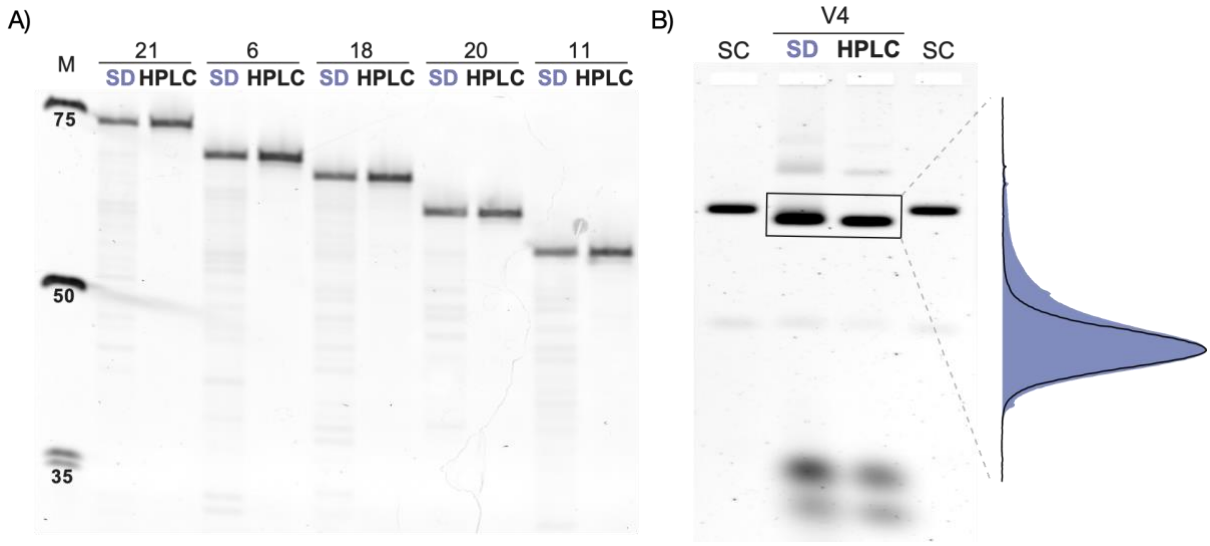

Figure 15: Evaluating Staple Purity's Effect on DNA Origami Structure via Gel Electrophoresis: A) Examining five distinct staple lengths to showcase the differences between desalting and HPLC purification methods, emphasizing identifying potential truncations. B) Analysis of DNA origami folding with either desalted or HPLC-purified staples, demonstrating the impact on the monomer band's electrophoretic mobility and clarity [133].

We performed further analysis to evaluate the importance of compositional similarity using cryo-EM SPA. After assembling, structure V4 underwent filtration purification to remove excess staples and concentrate the sample. This optimization prepared it for grid preparation and subsequent cryo-EM SPA. SPA was employed to show the structures of the V4 DNA origami objects composed

of desalted and HPLC-purified staple strands, shown in Figure *16*A and Figure *16*B, respectively. The cryo-EM consensus map for the variant, assembled with desalted oligonucleotides, yielded an overall resolution of 7.8Å from a dataset comprising 409k particles (Figure *32*). The variant folded with HPLC-purified oligonucleotides yielded a resolution of 7.2Å, achieved from a smaller dataset of approximately 390k particles (Figure *34*). This result highlights the importance of oligonucleotide purity in enhancing the structural resolution of cryo-EM maps.

Multilayer DNA origami structures can experience internal dynamics, such as lattice breathing or domain motions, which may impact their rigidity. Techniques such as multibody analysis or focused refinement address this issue, allowing us to consider flexibility and achieve higher resolution in specific areas. The structure of DNA origami V4 contains no distinct domains; therefore, to improve the resolution, we employed focused refinement on subsection slices that include peripheral regions and a slice through the central core. This process, detailed in Figure *33* and Figure *35*, improved the resolution, with the central domains of the V4 object achieving resolutions of 5.0 Å and 5.1 Å for the desalted and HPLC-purified samples, respectively. After the focused refinement of the two cryo-EM maps, our goal was to identify any structural differences resulting from the various purification methods.

Despite using consistent data processing techniques and applying equal threshold settings within ChimeraX before fitting the maps, Figure *16*C reveals structural differences between the two samples. By setting the same threshold for both cryo-EM maps, we aimed to compare their compactness after superimposition. The comparison in Figure *16*C indicates that the main surface color corresponds to the DNA origami constructed with desalted purified staple oligonucleotides. We conducted precise width measurements at two specific locations within two helices on longitudinal cross-sections. This allowed us to accurately assess how the purity of the staple strands affects DNA origami density and to eliminate any potential errors arising from visual threshold calibration in ChimeraX. As displayed in Figure *16*C, the distance from the midpoint of the upper to the lower helices consistently showed a difference of approximately 4 Å. The consistent difference in size shows that DNA origami structures folded with HPLC-purified staples are more tightly packed than those

purified by desalting. This highlights the influence of purification quality on the compactness of DNA origami structures.

Our experiments, which included gel electrophoresis and whole-object SPA cryo-EM, have demonstrated that the purity of staple strands plays a crucial role in determining the compactness of DNA origami structures. Despite the multibody refinement analysis revealing comparable local resolution improvements for both purity methods, it also suggests a challenge in discerning sample heterogeneity at an atomic scale with the current resolution capabilities. Nonetheless, we can distinguish differences in their compactness by visually assessing and precisely measuring interhelical distances in the DNA origami cryo-EM maps. Higher purity in staple strands correlates with increased compactness in the resulting DNA origami configuration.

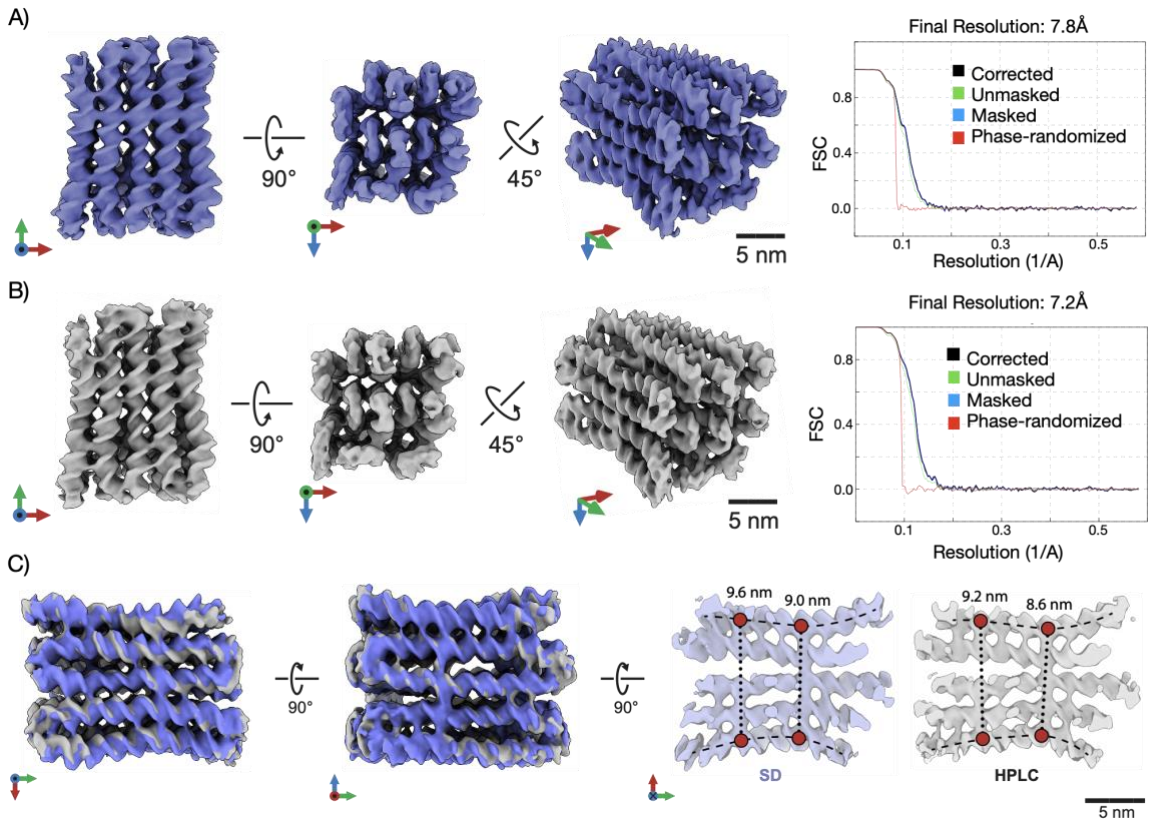

Figure 16: Three-Dimensional Cryo-EM Mapping of DNA Origami V4 Utilizing Distinct Staple Purification Techniques: A) Presents the cryo-EM map of Origami V4 folded with desalted purified staples, depicted in three orientations, with the Fourier Shell Correlation (FSC) curve displayed in the far-right panel. B) Exhibits the cryo-EM map of Origami V4 folded with HPLC purified staples, also shown in three views, followed by the FSC curve in the extreme right panel. C) Showcases a comparative analysis of both versions, with the leftmost panels highlighting the superimposed maps' disparities and the rightmost panels detailing the longitudinal cross-sections, where the interhelical distance measurements at two designated points illustrate the variance in structural compactness between the two methods [133].

Applications of Rigid DNA Origami

Throughout the previous sections, we have examined various approaches to maximize the compactness of DNA origami structures. Building on this, we utilized the designed rigid DNA origami as an alignment scaffold to improve the resolution of small molecules in cryo-EM SPA. Our goal was to enhance the signal-to-noise ratio. This method deals with the challenges faced in cryo-EM studies when working with small molecular targets. Specifically, we focused on a 27-nucleotide thrombin-binding DNA aptamer sequence (GTCCGTGGTAGGGCAGGTTGGGGTGAC). This sequence has an approximate molecular weight of 8 kDa. We used this sequence to demonstrate the application of our design improvements.

To attach the DNA aptamer to our origami structure, we utilized DNA origami V4 as the base framework. This design strategically included single-stranded regions within the scaffold to facilitate specific hybridization with the aptamer. The aptamer had handle sequences of eight bases at the 3' and 5' termini for attachment. The oligonucleotide staples were purified using HPLC to ensure accurate hybridization (as illustrated in Figure *17*A). The aptamer was then combined with the other components necessary for origami assembly, and the entire self-assembly occurred in a single-pot reaction. After assembly, the sample was stored at 4°C to preserve its structural integrity. To verify the successful integration of the aptamer into the DNA origami structure, we labeled the aptamer with the fluorescent marker Cy5. This allowed confirmation of its attachment through the hybridization of the designed handle sequences (shown in Figure *29*). The aptamer-origami complexes were purified using size exclusion chromatography and concentrating using a molecular-weight cut-off filtration. Gel electrophoresis analysis confirmed the retention of the aptamer after purification and sample concentration (Figure *31*).

Utilizing SPA, we successfully captured the structure of a DNA origami-aptamer complex. In Figure *17*, we present a typical micrograph, the 2D class averages, and the consensus map of the DNA origami particles, which was resolved to an overall resolution of 7.5 Å. This consensus map distinctly revealed the aptamer as a globular extension at its anticipated location on the scaffold.

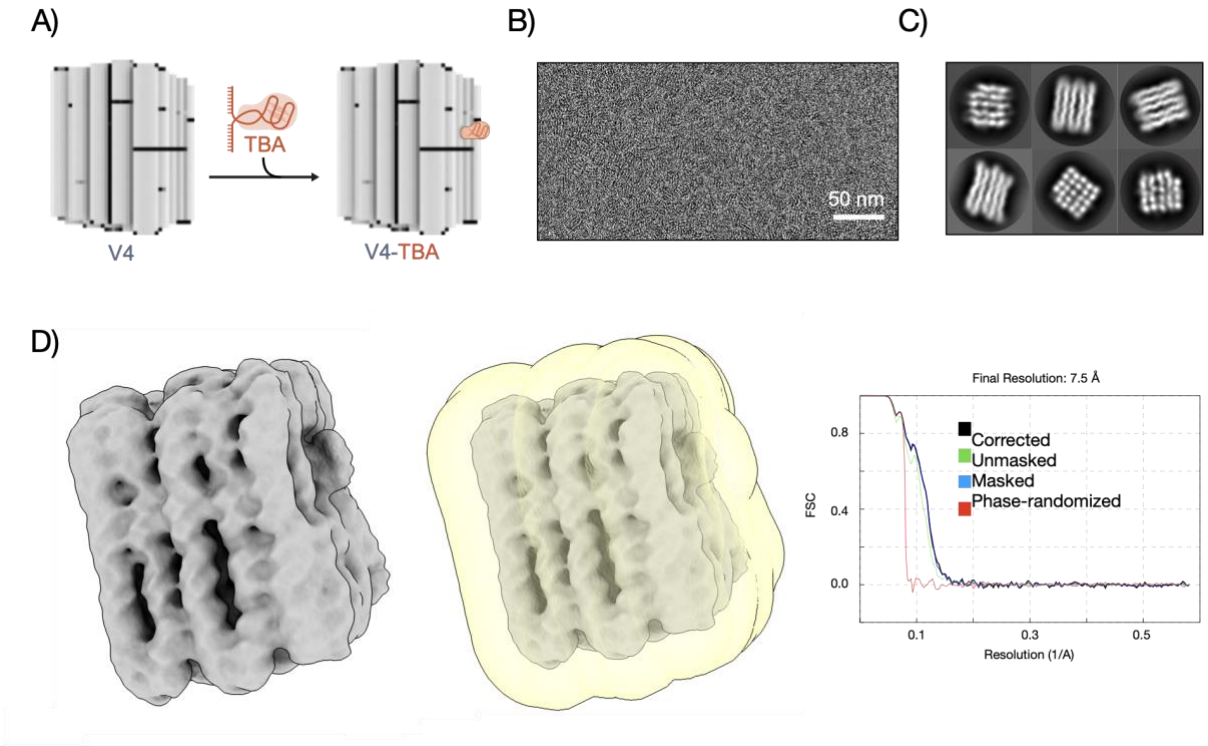

Figure 17: Elucidating the Attachment of TBA to DNA Origami V4 via Cryo-EM SPA: A) A schematic representation of the DNA origami V4 intertwined with the thrombin-binding aptamer (TBA), depicting their points of attachment. B) A representative cryo-EM micrograph demonstrating a high concentration of particles. C) Select 2D class averages derived from the cryo-EM micrograph particle picks. D) Sequentially from left to right: the 3D reconstructed complex of Origami-TBA, the mask utilized for resolution determination, and the FSC curve, which indicates an achieved resolution of 7.5 Å [133].

To improve the resolution of specific parts of the Origami-TBA complex, which is limited by the flexible nature of DNA origami, we utilized focused refinement using the multibody feature in the Relion software. This approach enabled us to refine distinct regions separately, each with varying degrees of rigidity, thus enhancing the resolution of each specific segment within the complex.

In Figure *18*, we present the precise refinement results for various sections of the DNA origami structure. Employing a tight mask that covers the entire target area allowed us to enhance each feature to its highest potential resolution. After conducting the multibody analysis, we used a broader mask that had been previously employed in the entire origami refinement process to ensure an

accurate resolution estimation. This process yielded resolutions of 5.1Å for the upper segment, 4.9Å for the central region, and 5.1Å for the lower segment, demonstrating the effectiveness of our targeted refinement approach.

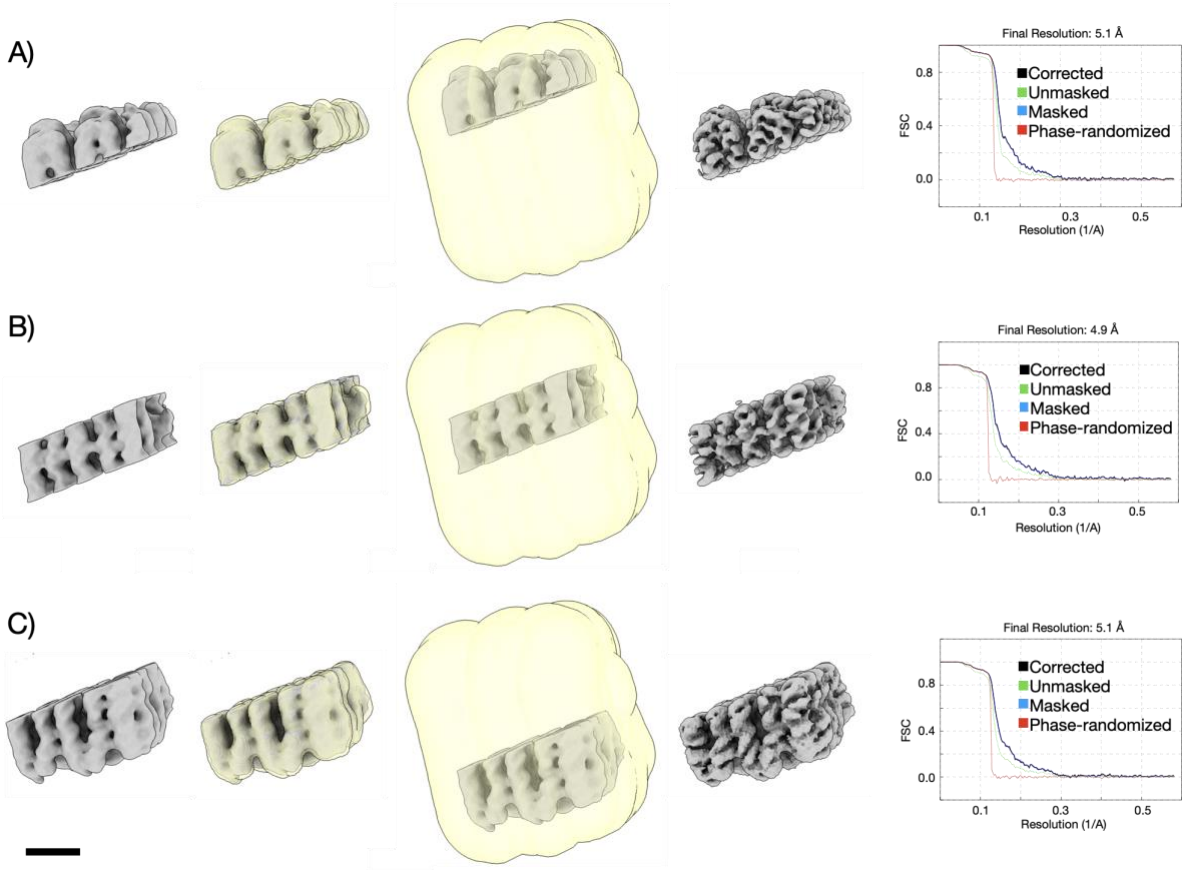

Figure 18: Enhancing Segment-Specific Resolution in the Origami-TBA Complex via Focused Refinement: A) Presented sequentially from left to right are: the upper flexible segment of the DNA origami from the consensus map; the tight mask applied for multibody refinement in Relion; the resolution-defining mask, identical to that used for the consensus map; the refined reconstruction of the upper segment of the DNA origami; and the FSC curve, delineating a final resolution of 5.1Å. B) Depicted in order from left to right: the central rigid section of the DNA origami containing the bound TBA, excised from the consensus map; the tight mask for multibody refinement; the resolution determination mask, mirroring the consensus map; the enhanced reconstruction of the central DNA origami segment; and the FSC curve, indicating a final resolution of 4.9Å. C) Illustrated in sequence from left to right: the lower flexible segment of the DNA origami taken from the consensus map; the tight mask for multibody analysis; the resolution assessment mask, which is consistent with the one used for the overall map; the sharpened reconstruction of the lower DNA origami section; and the FSC curve, confirming a final resolution of 5.1Å [133].

The cryo-electron microscopy reconstructed map shown in Figure *19*A and Figure *19*B highlights specific structural characteristics of the aptamer, particularly the noticeable torsional alignment of the G-quadruplex domain towards the adjacent stem helix. This configuration contrasts with the aptamer's arrangement in the known crystal structure, detailed in PDB 4I7Y and referenced in Figure *19*C, where the aptamer assumes a different orientation. This conformational adjustment was further examined using a model based on the aptamer's crystallographic data and the double-stranded scaffold DNA, refined through restrained molecular dynamics simulations (MDFF) as outlined in our methods section.

The altered aptamer conformation in our model, compared to the crystal structure, may be due to the absence of α-Thrombin, which was closely associated with the aptamer in the crystal structure. In the crystallographic data, the aptamer was captured in its thrombin-bound form. In contrast, in our cryo-EM experiments, α-Thrombin was absent, potentially allowing the aptamer more structural freedom. Additionally, the 5’ end of the aptamer's stem, which links to the scaffold DNA, is predicted to enforce a geometry-restricting U-turn formation. This could impart further structural constraints, influencing the aptamer's overall conformation in the DNA origami context and providing insight into its structural dynamics when not bound to its protein target.

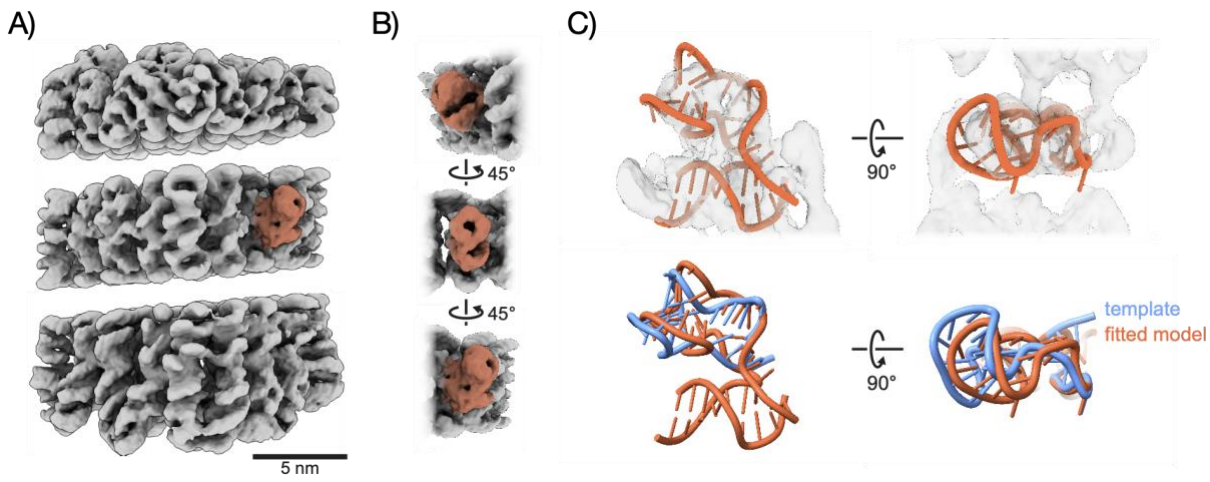

Figure 19: Integration of a Thrombin-Binding DNA Aptamer into DNA Origami Visualized by Cryo-EM SPA: A) Displays separated views of the flexible outer segments and the more rigid core regions delineated by multibody analysis, with the DNA aptamer highlighted in distinctive colors for clear identification. B) Presents the DNA aptamer in a color-coded format from various perspectives for an all-encompassing visual evaluation. C) The upper panel showcases the model of the aptamer combined with the DNA scaffold integrated into the cryo-EM map, and the lower panel contrasts this fitted model with the original crystallographic template derived from the protein-bound structure (PDB 4I7Y) [133].

After determining the structure of the DNA aptamer in conjunction with the DNA origami framework, we evaluated its functionality in this composite arrangement. Human α-Thrombin was introduced to the DNA origami-aptamer complex in a 1:1 concentration ratio thirty minutes before the preparation of cryo-EM grids. This step ensured the aptamer was bound to the DNA origami scaffold and maintained its binding affinity for the thrombin protein target. Cryo-EM was employed as the investigative tool to observe the thrombin-aptamer interaction to provide structural insights and confirm the aptamer's biological activity in its new configuration.

Figure *20* shows an acquired micrograph, 2D classes, and 3D refined structure. We employed multibody analysis, and the rigid central part containing the DNA Aptamer and human α-Thrombin, according to the FSC curve, shows a resolution of 9.3Å. Therefore, the cryo-EM confirmation of the human α-Thrombin binding to the aptamer confirms that its anchorage to the scaffold did not hinder its

functionality. This finding demonstrates that the aptamer maintains its structural integrity and binding capability after assembly, with active sites accessible and correctly aligned for interaction. Such successful binding, as visualized through cryo-EM, emphasizes the capability of DNA origami as a functional platform. This opens avenues for constructing complex biomolecular assemblies while retaining biological activity.

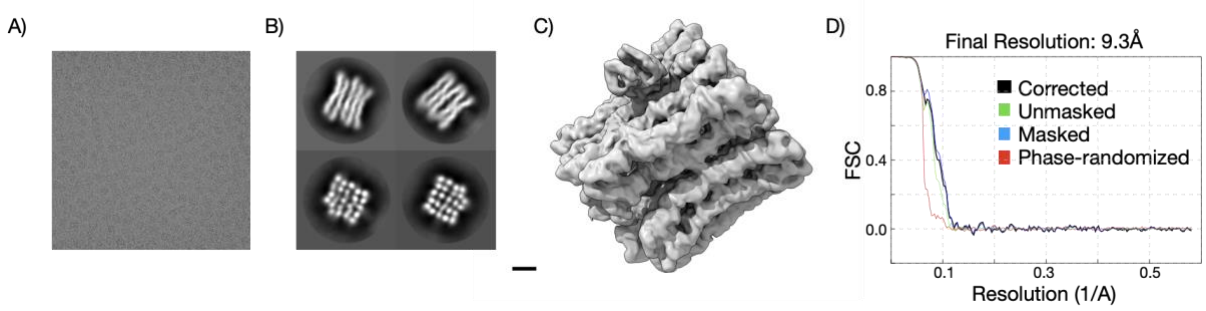

Figure 20: Interaction Analysis of DNA Origami-Aptamer-Thrombin Complex: A) An exemplar cryo-EM micrograph from the sample. B) 2D class averages derived from Relion data processing. C) The 3D refined structure of the complex. D) The FSC curve indicates the final resolution of 9.3Å [133].

In summary, this study successfully incorporated a 27-nucleotide thrombin-binding DNA aptamer into a DNA origami scaffold and used cryo-EM to confirm the aptamer's structure consistency with its crystallized counterpart. The pursuit of determining the DNA aptamer's structure at the individual nucleobase level requires a higher resolution than what was achieved here. This goal is hindered by the inherent flexibility of DNA origami and the dynamic interactions at the aptamer-origami interface. Advancements in experimental techniques will be crucial to overcome these challenges and enable the detailed structural elucidation aimed at this research.

To verify the functional viability of the integrated aptamer, we introduced human α-Thrombin to the complex. We demonstrated through cryo-EM that the aptamer retains its ability to bind its protein target effectively. The aptamer's active sites remained accessible and were properly oriented for binding, indicating that the structural assembly process preserved its functional integrity. The potential of

DNA origami as a scaffold for assembling complex biomolecular systems is highlighted by the successful demonstration of specific binding. The research findings suggest potential future applications utilizing the functional capabilities of DNA nanotechnology.

Conclusions and Future Perspectives

Recognizing the challenges presented by the inherent flexibility of DNA origami, our research aimed to explore the potential of design and composition modifications to enhance the rigidity of these structures. We strategically increased the number of scaffold crossovers and adjusted the lengths of the staple strands to achieve a more rigid structure. Additionally, we focused on using staples with a higher degree of purity to promote a more compact assembly. These intentional changes were designed to investigate their collective impact on producing a more rigid DNA origami structure.

Our research has revealed that increasing the number of scaffold crossovers in DNA origami design contributes to the compactness of the structure. This structural compactness, however, necessitates a higher salt concentration and a longer folding period to achieve the desired stability. The results of these adjustments were demonstrated through gel electrophoresis and cryo-EM, providing evidence of the enhanced rigidity within the DNA origami constructs.

In addition to scaffold crossover adjustments, another critical design parameter we modified was the average length of the staple strands. Our study showed that the DNA origami structure with shorter staple strands resulted in a more rigid framework than a structure with identical shapes and scaffold routings but longer staple strands. This correlation between staple length and structural rigidity was confirmed through cryo-EM and gel electrophoresis analyses, emphasizing the importance of staple length in designing more compact DNA origami structures.

Another critical factor we explored was the influence of compositional heterogeneity on DNA origami structure. To address this, we utilized two distinct methods for purifying the staple strands. The first method involved desalting purification, while the second used HPLC to purify chemically synthesized oligonucleotides. Our analysis, mainly through PAGE gel, revealed excess bands indicative of truncated staple oligonucleotides resulting from the synthesis process. We discovered differences in rigidity and compactness by comparing

the structural outcomes of DNA origami folded using both desalting and HPLC purification methods. This was demonstrated through gel electrophoresis and cryo-EM SPA. The DNA origami structures assembled with HPLC-purified staples exhibited more rigid forms with reduced interhelical distances. These findings emphasize the significance of staple purity on the structural integrity of DNA origami constructs.

The development of rigid DNA origami structures shows potential for improving cryo-EM studies, especially when studying low molecular weight molecules. In cryo-EM, the main challenge often lies in the signal-to-noise ratio, which decreases as the molecular weight is reduced. To address this issue, we used our designed rigid DNA origami as a scaffold for guest molecules, enhancing the signal-to-noise ratio. Our target for this application was a thrombin-binding aptamer weighing approximately 8 kDa. Utilizing cryo-EM, we successfully imaged this aptamer. However, we faced an important challenge: overcoming the resolution limits through advanced data processing techniques. Like the one in our study, flexible structures often present challenges when achieving high-resolution 3D reconstructions. To address these challenges, we utilized the multibody refinement feature of the Relion software, enabling us to separately refine different areas of the DNA origami structure based on their flexibility. This approach was crucial in overcoming the constraints imposed by the flexibility of DNA origami, allowing us to achieve higher resolution in our cryo-EM studies. This achievement underscores the effectiveness of rigid DNA origami in cryo-EM and illustrates the potential of advanced data processing methods in resolving complex biomolecular structures.

In addition to analyzing the structure, we thoroughly assessed the functional integrity of the DNA aptamer while bound to the DNA origami scaffold. Our experiments aimed to determine whether the aptamer could still effectively bind to human alpha thrombin when integrated into the origami structure. The promising results revealed that the aptamer maintained its affinity for the thrombin target. This was evidenced by the fact that the aptamer's active sites remained both accessible and properly aligned for interaction, suggesting that the process of incorporating it into the DNA origami did not compromise its biological function. The successful demonstration of this specific binding interaction shows that DNA

origami can effectively serve as a scaffold for assembling complex biomolecular systems without hindering the functionality of the individual components. The findings of our study provide a basis for future advancements in DNA nanotechnology, where the combination of structural stability and functional viability is essential.

Supporting information: Materials and Methods

Buffers

Folding Buffer (FOBx):

This buffer consists of 5 mM TRIS, 1 mM EDTA, 5 mM NaCl, and a variable concentration of $MgCl_2$, adjusted to pH 8. The $MgCl_2$ concentration is denoted by the 'x' in FOBx; for instance, FOB30 includes 30 mM MgCl2.

Gel Running Buffer:

For electrophoresis, a 0.5 x TBE buffer with an addition of 5.5 mM $MgCl_2$ is used.

PEG Precipitation Buffer:

The PEG precipitation buffer comprises 15% polyethylene glycol (PEG) 8000, 5 mM TRIS, 1 mM EDTA, and 500 mM NaCl, facilitating the precipitation process in DNA origami purification.

HPLC Buffer:

High-Performance Liquid Chromatography (HPLC) requires a buffer of 5 mM TRIS, 1 mM EDTA, 5 mM NaCl, and 35 mM $MgCl_2$, balanced to pH 8, to ensure optimal separation and stability of the DNA structures during purification.

Folding

DNA origami designs were synthesized within this research through a unified one-pot mixture approach. This involved the combination of in-house prepared circular scaffold DNA with oligonucleotides acquired from IDT, all integrated within a 1x FOB buffer. The concentration of magnesium chloride was precisely adjusted from 5 mM to 30 mM, aligning with the specific folding criteria required for each structure. Folding reactions took place in a Tetrad thermal cycler and began with a 15-minute denaturation stage at 65°C, resolving any secondary structures within the DNA. This initial step was succeeded by a customized annealing schedule, individually adapted for the various DNA strands. After annealing, samples (V1-V4) were kept at room temperature, while V4_TBA was stored at 4°C to maintain its structural integrity.

An initial folding screen (IFS) (Figure *25*, Figure *26*, Figure *27*, and Figure *28*) was conducted as a fundamental part of the assembly protocol. This screening involved an exhaustive evaluation of scaffold-to-staple ratios, thermal profiles, and magnesium chloride concentrations, all crucial in fine-tuning the folding mechanism. The assembly conditions explored were extensive, including:

- RM1: Utilizing a scaffold concentration of 50 nM paired with staples at 200 nM.
- RM2: Employing a scaffold concentration of 20 nM, again with staples at 200 nM.
- T1 to T8 series: Encompassing a progression of temperature intervals, starting at a 50 °C to 47 °C range for T1 and ascending in 2 °C increments for each subsequent condition, up to a 64 °C to 61 °C range for T8.
- M series: Featuring incremental magnesium chloride concentrations, starting from M5 at 5 mM and increasing by 5 mM steps through M10, M15, M20, and M25, culminating at M30 with 30 mM MgCl2.

After rigorous trials, the most effective folding parameters were determined to guide the accurate assembly of DNA origami structures.

Gel Electrophoresis

To prepare 2% agarose gels for analyzing larger DNA origami structures with 2873 scaffold bases, 2.5 g of UltraPure™ Agarose (Invitrogen™, Thermo Fisher Scientific) was dissolved in 122.5 ml of 0.5 x TBE buffer. To analyze smaller DNA origami constructs with 1033 scaffold bases, 4% agarose gels were prepared by dissolving 5 g of agarose into 120 ml of 0.5 x TBE buffer. These differing concentrations accommodate the resolution requirements for DNA origami structures of various sizes. This mixture was then heated in a microwave until the agarose fully dissolved. Any water lost to evaporation during this process was replaced with double-distilled water. The molten agarose was cooled to around 40 °C with continuous agitation. Subsequently, 5.5 mM $MgCl_2$ and 5 drops of 0.025% ethidium bromide solution (250 µg/ml, from a dropper bottle by Carl Roth) were incorporated into the solution. This agarose solution was poured into a gel casting tray (Owl Easycast™ B2, Thermo Scientific) and left to set.

Once solidified, the gel was placed in an electrophoresis chamber and covered with a running buffer. Samples were mixed with loading dye composed of 15% Ficoll 400, 0.1% Bromphenol blue, and 5 mM TRIS (pH 8) at a 5:1 sample-to-dye ratio and loaded into the wells. Electrophoresis was conducted at 90V for approximately 2 hours. The resulting gel was scanned using a Typhoon FLA9500 (GE Healthcare) laser scanner set to a 50 µm/px resolution and a 532 nm excitation wavelength. For enhanced clarity of the gel images, the scan data was processed with the auto-contrast feature in Fiji (ImageJ2).

Optimal folding conditions were determined by assessing the intensity of the monomeric band, its migration distance, and bandwidth on the gel. Conditions that produced a prominent leading band but exhibited significantly shorter migration distances or wider bandwidths were deemed inferior and excluded from further consideration.

Purification

PEG Purification

Polyethylene glycol (PEG) purification is an effective alternative method for isolating DNA origami structures, particularly useful for preparing samples for high-resolution imaging techniques like cryo-EM. Our study employed PEG purification to prepare variants V1, V2, and V3 for subsequent cryo-EM analysis. The process begins with the folded DNA origami structures thoroughly mixed with a PEG precipitation buffer at a 1:1 volume ratio. This step is crucial for inducing the precipitation of DNA origami, as PEG alters the solvation properties and effectively concentrates the DNA structures. Following the addition of PEG, the mixture is subjected to centrifugation at 21,000 rcf for 25 minutes. This high-speed centrifugation ensures the efficient sedimentation of the DNA origami structures, separating them from the supernatant. After centrifugation, the supernatant is carefully removed, leaving behind a pellet that contains the concentrated DNA origami structures. The pellet is then gently resuspended in FoB5 buffer and incubated at 30 °C with moderate shaking. This step, lasting at least one hour, allows the DNA origami structures to dissolve fully into the buffer, ensuring a homogenous sample. The temperature and gentle agitation are important factors in facilitating the complete dissolution of the origami structures without causing damage or denaturation. To adjust the concentration of the DNA origami sample for optimal visualization under cryo-EM, the pellet from an initial 1 ml folding reaction is typically redissolved in a smaller volume, ranging from 50 µl to 100 µl.

PEG purification effectively concentrates and purifies DNA origami samples by removing excess staples after folding. This technique is valuable for high-resolution structural analyses like cryo-EM.

HPLC Purification

Incorporating Size Exclusion Chromatography (SEC) into the workflow, the method was utilized for the final purification step of the sample in preparation for cryo-EM analysis. SEC employs a gel matrix composed of spherical beads with pores that sort molecules by size. Smaller molecules diffuse into these pores, slowing their elution, while larger molecules bypass the pores and elute more quickly. This size-dependent elution allows for the separation of molecules by molecular weight, with smaller molecules exiting the column after larger ones.

The sample was processed using High-Performance Liquid Chromatography (HPLC) on an Agilent Technologies 1260/1290 Infinity system, using an Agilent Bio SEC-5 column with a 5 µm particle size, 1000 Å pore size and 21.2 mm by 300 mm dimensions. The process was carried out at a constant flow rate of 1 ml/min with 1x FOB35 buffer, identical in salt concentration to that used for folding the DNA origami V4 structure, thus ensuring uniform conditions for purification. The monomeric peak fractions were collected, and this purified sample was subsequently used for cryo-EM, which provides high-resolution structural information about the molecular assembly in its native state.

Filter Purification and Concentration

In the filter purification process, DNA origami samples, specifically V4-SD and V4-HPLC, were first diluted with 1 × Filtered Origami Buffer (FOB) to reach a final MgCl2 concentration of 5mM. This was followed by preparing Amicon Ultra 0.5-ml filters with a 50-kDa cut-off (Millipore), which were rinsed with 500 µl of 1 × FOB5 and centrifuged at 5000 rcf for 1 minute. The diluted samples were added to these filters and centrifuged at 5000 rcf for 5 minutes. A series of washing steps ensued, involving the removal of the flow-through, refilling the filters with 500 µl of 1 × FOB5, and repeated centrifugation. This was done several times to ensure thorough purification. Finally, the filters were inverted into fresh tubes and centrifuged to collect the filtered samples, which were then pooled for further use.

For the concentration of DNA origami samples, the same Amicon Ultra 0.5-ml 50-kDa cut-off filters (Millipore) were employed, initially rinsed with 500 µl of 1 × FOB5 and centrifuged at 5000 rcf for 1 minute. The DNA origami samples, encompassing V1, V2, V3, V4-SD, V4-HPLC, and V4-TBA, were added to the filters and subjected to a centrifugation of 5000 rcf for 10 minutes. In cases where the sample volume was larger, adding the sample and centrifuging at 5000 rcf was repeated for 5 minutes each, with the final step extended to 10 minutes. The process culminated with the filters being inverted into new tubes and centrifuged at 5000 rcf for 5 minutes, enabling the collection of the concentrated samples.

Negative Stain EM

Our Transmission Electron Microscopy (TEM) negative stain imaging protocol began with preparing the staining solution. In an Eppendorf tube, we carefully added a 1 µl droplet of 5 M NaOH to 200 µl of a 2% uranyl formate solution prepared in-house. This mixture was thoroughly vortexed for 1 minute to ensure homogeneity and then centrifuged at 16,100 rcf for 6 minutes. This step aids in removing any particulates from the stain, ensuring a clear and consistent staining solution for the samples. For sample preparation, a 5 µl droplet of the biological sample was gently placed onto the carbon-coated surface of a Cu400 TEM grid obtained from Electron Microscopy Sciences. Before this, the grid had been treated with a glow discharge process, enhancing its hydrophilicity and promoting uniform sample distribution and adherence.

After the sample application, the grid was blotted with filter paper to remove excess liquid, a critical step to achieve an optimal sample layer for imaging. The grid was then washed with a 5 µl droplet of the stain solution, followed by another blotting step to remove excess stain. This washing step is crucial for removing any unbound or loosely attached particles. Next, a 20 µl droplet of the stain solution was placed on the grid and incubated for 30 seconds. This step is pivotal for achieving sufficient sample staining, which enhances contrast in TEM imaging. After the incubation period, final blotting was performed, and the grid was left to dry for 15 minutes, ensuring that the sample was adequately adhered to and stained. The TEM imaging was conducted on two microscopes to provide comprehensive structural details. The first was a Philips CM-100 electron microscope, operating at an acceleration voltage of 100 kV and equipped with an AMT 2k x 2k CCD camera. The second was an FEI Tecnai Spirit TEM, operating at 120 kV and fitted with a Tietz TEMCAM-F416 camera, using SerialEM software for image acquisition. This combination of high-performance imaging equipment and meticulous sample preparation allowed us to capture detailed and high-contrast images of the negatively stained samples, facilitating a thorough structural analysis.

Cryo-EM

Preparation of Vitrified Specimens

We employed Quantifoil 200-mesh copper grids equipped with R1.2/1.3 holey carbon support films to prepare our cryo-EM grids. These grids are specifically designed to provide an optimal background for cryo-EM imaging, ensuring minimal interference with the visualization of samples. Before sample application, the grids underwent a critical cleaning step using an EMS K100X plasma cleaner (Electron Microscopy Sciences). During this 90-second treatment, they underwent a glow discharge process in a high-pressure air environment. This plasma cleaning is essential as it renders the grid surfaces hydrophilic, enhancing the sample's adhesion and spreading on the grid. The sample application was meticulously carried out in the controlled environment of a Vitrobot Mark IV chamber (FEI). To preserve the native state of the sample and prevent crystalline ice formation, which can obscure structural details, the chamber's conditions were precisely set to 100% humidity and maintained at a temperature of 4°C. This environment closely mimics the natural, hydrated state of biological samples. After placing the sample on the grid, the excess solution was carefully blotted away for 3 seconds, employing a blot force 20. This blotting step is crucial for achieving the optimal sample thickness on the grid. It is finely balanced to remove excess liquid while retaining a thin, uniform sample layer. Following blotting, the grid was rapidly plunged into liquid ethane. This quick-freezing method is vital for vitrification, a process where the water in the sample turns into amorphous ice without forming ice crystals. Vitrification effectively 'snap-freezes' the sample, preserving its structure in a close-to-native state, which is crucial for accurate cryo-EM analysis.

Data Acquisition

Our cryo-EM data acquisition was conducted using the Titan Krios microscope (ThermoFisher Scientific), which operates at 300 kV. This advanced microscope has a Falcon3 direct electron detector, renowned for its exceptional sensitivity and resolution capabilities. Additionally, the microscope features a spherical aberration (Cs) corrector. This integral component enhances image quality by correcting for spherical aberrations, thus improving the microscope's ability to produce sharp, detailed images at high resolutions. The imaging process was carried out in nanoprobe mode, utilizing a 50 µm C2 aperture and a 100 µm objective aperture. This mode is particularly suitable for achieving high-resolution images. For the datasets of V2, V4-SD, V4-HPLC, and V4-Aptamer, we used a magnified pixel size of 0.86 Å. In contrast, the datasets for V1 and V3 were captured at a slightly larger pixel size of 1.4 Å. Each movie was acquired with a total electron dose of 50 $e^{-}/Å^{2}$, a carefully calibrated exposure to ensure optimal image quality while minimizing electron beam-induced sample damage. The entire data collection procedure was automated using the EPU software from ThermoFisher Scientific. This software is instrumental in maintaining consistent and controlled imaging conditions, a crucial factor for the success of cryo-EM studies.

Data Processing

Our study's data processing began with applying motion correction to the collected cryo-EM movies. This step was accomplished using RELION's integration of the MotionCor2 algorithm[117], a sophisticated method designed to counteract the effects of electron beam-induced motion. This correction is vital for maintaining the integrity and clarity of the microscopic images. Following motion correction, the Contrast Transfer Function (CTF) of the non-dose-weighted micrographs was estimated using the CTFFIND-4.1 software[134]. Accurate CTF estimation is crucial for subsequent image processing stages as it affects the interpretation of the electron microscopy data. For the crucial task of particle selection, we employed two approaches depending on the dataset: the crYOLO software[135] and the Laplacian-of-Gaussian (LoG) automated picking routine. The crYOLO software uses deep learning to identify particles, offering high accuracy and efficiency. In contrast, the LoG routine, utilized within Relion4 on dose-weighted micrographs, provides an automated, algorithm-based approach to particle picking. Initial models were generated directly in Relion using the extracted particle data in its unprocessed form. These models serve as starting points for further refinement and provide an initial guess of the particle structure. For a more detailed structural analysis, we conducted multibody refinement in Relion. This process involved dividing the consensus maps into specific regions using UCSF Chimera's crop tool[136]. These regions were then subjected to low-pass filtering, binarization, and the addition of soft-edge voxels to create the masks necessary for multibody refinement. The masks used were tightly fitted around all critical features of the consensus map to ensure accurate refinement. Post-refinement, the maps were processed with broad, low-pass-filtered masks—identical to those used in the post-processing of the consensus map—for the computation of the Fourier Shell Correlations (FSCs), as shown in Figure *18*. This step helps in evaluating the resolution and quality of the reconstructed images. Lastly, to further enhance the clarity and detail of the final maps, we employed deepEMhancer[137] and LocSpiral[138] software. These tools allow for the sharpening and improving the images, providing a clearer and more detailed visualization of the structures under study. This comprehensive and nuanced approach to data processing is critical for extracting the most accurate structural information from the cryo-EM datasets.

Model Building

We initiated our model-building methodology by utilizing the crystal structure of the aptamer DNA strand from the Protein Data Bank (PDB entry 4I7Y) as a foundational template. This structure was meticulously fitted into the density map as a rigid body using COOT software[139]. To elucidate the junction between the aptamer and its adjoining DNA scaffold, we constructed a 16-base pair model of canonical B-form DNA helix within COOT, subjected to rigid body fitting.

In the next step, the bases of this model were renumbered to align with the aptamer sequence as detailed in PDB entry 4I7Y, and the strands of DNA were manually connected within COOT. For a more nuanced fit, flexible fitting was carried out using the CHIMERAX/ISOLDE[140, 141] software, which included applying specific self-distance restraints to the aptamer section and the scaffold DNA helix.

Subsequently, the model was refined in real space using the FastRelax protocol in the ROSETTA [142]suite. This refinement was comprehensive, integrating density scoring and torsional reference model restraints for accuracy. These reference model restraints were generated by phenix.real_space_refine, based on nucleotides 5-20 from the 4I7Y structure (except for nucleotides 8-9 in chain A) and an ideal DNA model (excluding nucleotides 8 and 38 in chain B) as depicted in Figure *19* [143]. This meticulous process allowed for a highly detailed and accurate representation of the aptamer-DNA scaffold interface.

Supporting information: DNA Origami Designs

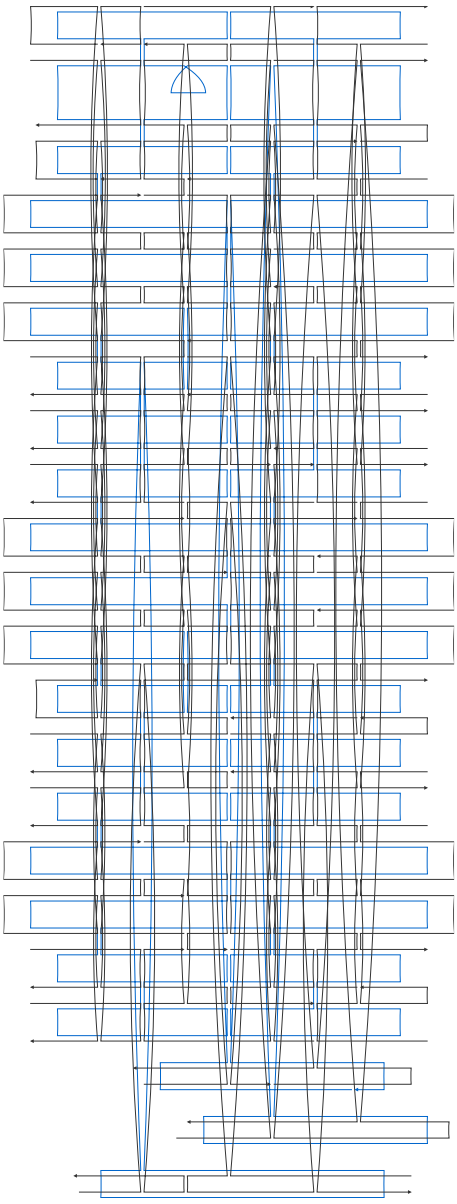

Figure 21: DNA Origami Version 1 Design Diagram: This diagram represents the V1 design, created using cadnano software on a square lattice framework. The design features a scaffold of 2,873 nucleotides of single-stranded DNA, represented by blue lines that illustrate the scaffold's pattern and gray lines indicating the routing of the staples.

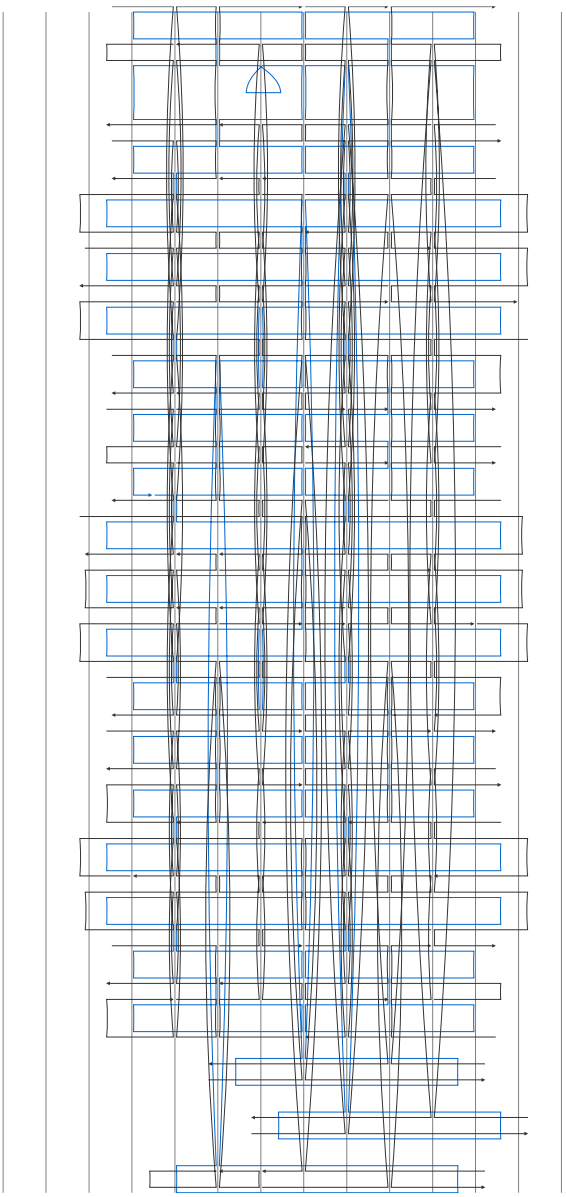

Figure 22: DNA Origami Version 2 Design Diagram: This diagram represents the V2 design, created using cadnano software on a square lattice framework. The design features a scaffold of 2,873 nucleotides of single-stranded DNA, represented by blue lines that illustrate the scaffold's pattern and gray lines indicating the routing of the staples.

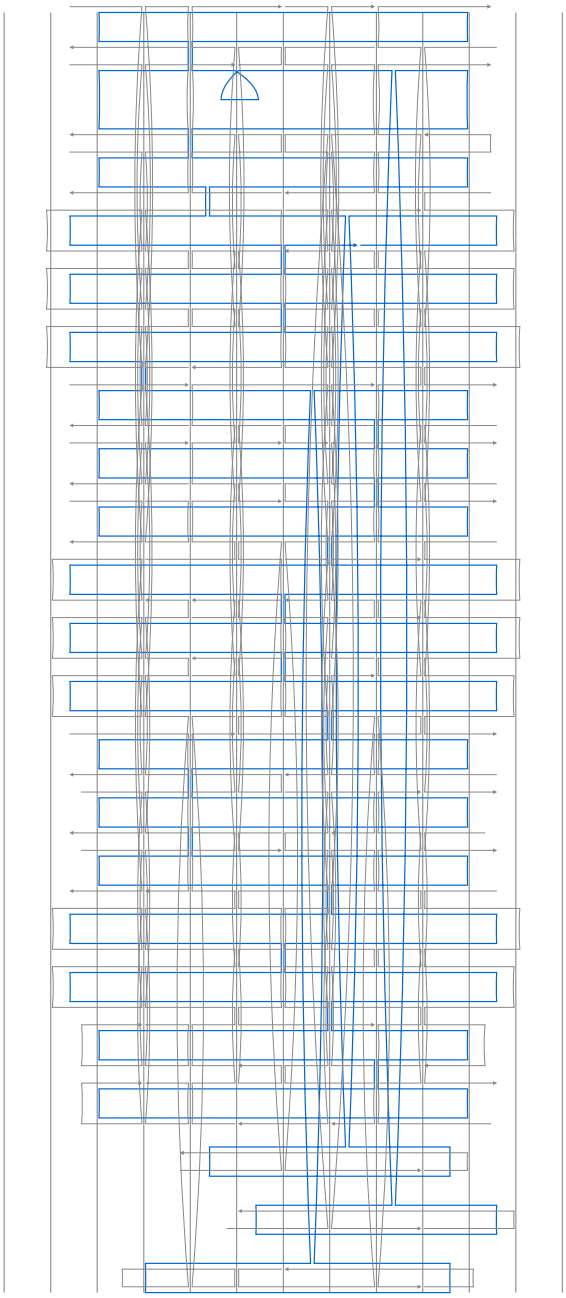

Figure 23: DNA Origami Version 3 Design Diagram: This diagram represents the V3 design, created using cadnano software on a square lattice framework. The design features a scaffold of 2,873 nucleotides of single-stranded DNA, represented by blue lines that illustrate the scaffold's pattern and gray lines indicating the routing of the staples.

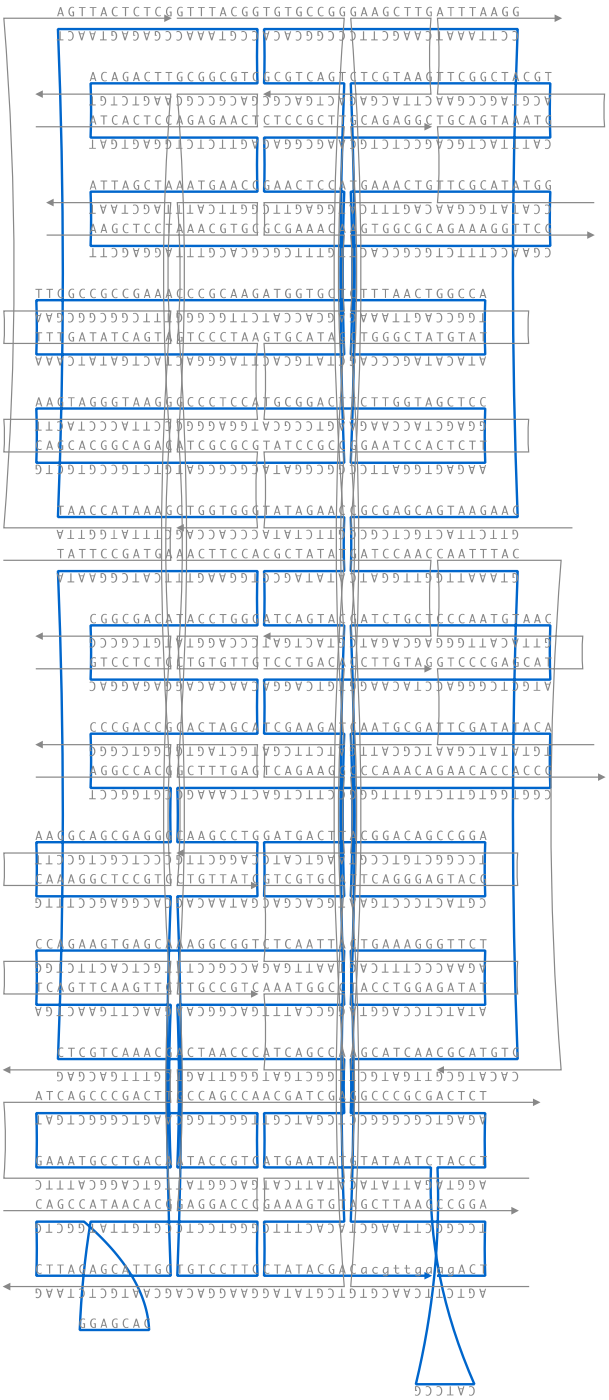

Figure 24: DNA Origami Version 4 Design Diagram: This diagram represents the V4 design, created using cadnano software on a square lattice framework. The design features a scaffold of 1,033 nucleotides of single-stranded DNA, represented by blue lines that illustrate the scaffold's pattern and gray lines indicating the routing of the staples.

Note 1: 2873 Scaffold:

GTGGCACTTTTCGGGGAAATGTGCGCGGAACCCCTATTTGTTTATTTTTCT
AAATACATTCAAATATGTATCCGCTCATGAGACAATAACCCTGATAAATGCT
TCAATAATATTGAAAAAGGAAGAGTATGAGTATTCAACATTTCCGTGTCGCC
CTTATTCCCTTTTTTGCGGCATTTTGCCTTCCTGTTTTTGCTCACCCAGAAA
CGCTGGTGAAAGTAAAAGATGCTGAAGATCAGTTGGGTGCACGAGTGGGT
TACATCGAACTGGATCTCAACAGCGGTAAGATCCTTGAGAGTTTTCGCCCC
GAAGAACGTTTTCCAATGATGAGCACTTTTAAAGTTCTGCTATGTGGCGCG
GTATTATCCCGTATTGACGCCGGGCAAGAGCAACTCGGTCGCCGCATACA
CTATTCTCAGAATGACTTGGTTGAGTACTCACCAGTCACAGAAAAGCATCT
TACGGATGGCATGACAGTAAGAGAATTATGCAGTGCTGCCATAACCATGA
GTGATAACACTGCGGCCAACTTACTTCTGACAACGATCGGAGGACCGAAG
GAGCTAACCGCTTTTTTGCACAACATGGGGGATCATGTAACTCGCCTTGAT
CGTTGGGAACCGGAGCTGAATGAAGCCATACCAAACGACGAGCGTGACAC
CACGATGCCTGTAGCAATGGCAACAACGTTGCGCAAACTATTAACTGGCG
AACTACTTACTCTAGCTTCCCGGCAACAATTAATAGACTGGATGGAGGCGG
ATAAAGTTGCAGGACCACTTCTGCGCTCGGCCCTTCCGGCTGGCTGGTTT
ATTGCTGATAAATCTGGAGCCGGTGAGCGTGGGTCACGCGGTATCATTGC
AGCACTGGGGCCAGATGGTAAGCCCTCCCGTATCGTAGTTATCTACACGA
CGGGGAGTCAGGCAACTATGGATGAACGAAATAGACAGATCGCTGAGATA
GGTGCCTCACTGATTAAGCATTGGTAACTGTCAGACCAAGTTTACTCATAT
ATACTTTAGATTGATTTAAAACTTCATTTTTAATTTAAAAGGATCTAGGTGAA
GATCCTTTTTGATAATCTCATGACCAAAATCCCTTAACGTGAGTTTTCGTTC
CACTGAGCGTCAGACCCCGTAGAAAAGATCAAAGGATCTTCTTGAGATCCT
TTTTTTCTGCGCGTAATCTGCTGCTTGCAAACAAAAAAACCACCGCTACCA
GCGGTGGTTTGTTTGCCGGATCAAGAGCTACCAACTCTTTTTCCGAAGGTA
ACTGGCTTCAGCAGAGCGCAGATACCAAATACTGTTCTTCTAGTGTAGCCG
TAGTTAGGCCACCACTTCAAGAACTCTGTAGCACCGCCTACATACCTCGCT
CTGCTAATCCTGTTACCAGTGGCTGCTGCCAGTGGCGATAAGTCGTGTCTT
ACCGGGTTGGACTCAAGACGATAGTTACCGGATAAGGCGCAGCGGTCGG
GCTGAACGGGGGGTTCGTGCACACAGCCCAGCTTGGAGCGAACGACCTA
CACCGAACTGAGATACCTACAGCGTGAGCTATGAGAAAGCGCCACGCTTC
CCGAAGGGAGAAAGGCGGACAGGTATCCGGTAAGCGGCAGGGTCGGAAC
AGGAGAGCGCACGAGGGAGCTTCCAGGGGGAAACGCCTGGTATCTTTATA
GTCCTGTCGGGTTTCGCCACCTCTGACTTGAGCGTCGATTTTTGTGATGCT
CGTCAGGGGGGCGGAGCCTATGGAAAAACGCCAGCAACGCGGCCTTTTT
ACGGTTCCTGGCCTTTTGCTGGCCTTTTGCTCACATGTTCTTTCCTGCGTT
ATCCCCTGATTCTGTGGATAACCGTATTACCGCCTTTGAGTGAGCTGATAC
CGCTCGCCGCAGCCGAACGACCGAGCGCAGCGAGTCAGTGAGCGAGGAA
GCGGAAGAGCGCCCAATACGCAAACCGCCTCTCCCCGCGCGTTGGCCGA
TTCATTAATGCAGCTGGCACGACAGGTTTCCCGACTGGAAAGCGGGCAGT
GAGCGCAACGCAATTAATGTGAGTTAGCTCACTCATTAGGCACCCCAGGC
TTTACACTTTATGCTTCCGGCTCGTATGTTGTGTGGAATTGTGAGCGGATA
ACAATTTCACACAGGAAACAGCTATGACCATGATTACGCCAAGCGCGAATT
CTCCAGGCTTAGAATTCGCTCACTGGCCGTCGTTTTACACCATGATTACGC
CAAGCGCGAATTCTCCAGGCTTAGAATTCGCTCACTGGCCGTCGTTTTACA
ACGTCGTGACTGGGAAAACCCTGGCGTTACCCAACTTAATCGCCTTGCAG
CACATCCCCCTTTCGCCAGCTGGCGTAATAGCGAAGAGGCCCGCACCGAT
CGCCCTTCCCAACAGTTGCGCAGCCTGAATGGCGAATGGGACGCGCCCT
GTAGCGGCGCATTAAGCGCGGCGGGTGTGGTGGTTACGCGCAGCGTGAC

CGCTACACTTGCCAGCGCCCTAGCGCCCGCTCCTTTCGCTTTCTTCCCTTC
CTTTCTCGCCACGTTCGCCGGCTTTCCCCGTCAAGCTCTAAATCGGGGGC
TCCCTTTAGGGTTCCGATTTAGTGCTTTACGGCACCTCGACCCCAAAAAAC
TTGATTAGGGTGATGGTTCACGTAGTGGGCCATCGCCCTGATAGACGGTT
TTTCGCCCTTTGACGTTGGAGTCCACGTTCTTTAATAGTGGACTCTTGTTC
CAAACTGGAACAACACTCAACCCTATCTCGGTCTATTCTTTTGATTTATAAG
GGATTTTGCCGATTTCGGCCTATTGGTTAAAAAATGAGCTGATTTAACAAAA
ATTTAACGCGAATTTTAACAAAATATTAACGCTTACAATTTAG

Note 2: Scaffold 1033:

AGACTTCCGGCTTAAGCTCTGAAAGGGTTCTATATCTCCAGGTAGATCTGC
TCCCAATGTAACATGCTCGGGACCTACAAGGTGTCAGGATCGAAGATTGC
ACGACGATGACTTACGGACAGCCGGACGTACTCCCTGAACAATGCGATTC
GATATACACGGTGGTGTTCTGTTTGGGCCTTCTGACTCAAAGCCAAGCCTG
GATAACAGTGTCCTTCGGGTCCTCCGTGTTATGGAGCACGGCTGCTTAGA
GCATTGCCACGGAGCCTTTGAAGGCAGCGAGGGCGTGGCCTCCCGACCG
CACTAGCACAACACAGGAGAGGACCGGCGACATACCTGGGTGGAAGTTTC
ATCGGAATACTCGTCAAACGACTAACCCATCAGCCATCGATCGTATGAATA
TGTATAATCCATCCGTACCTAGAGTCGCGGGCCAGCATCAACGCATGTGG
TAAATTGGTTGGATCCGCGAGCAGTAAGAACCCTTAAATCAAGCTTCCCGG
CACAGCGTCAGTGGCGGATACGCGCGATGTCTGCCGTGCTGAAGTAGGG
TAAGGGCCCTCCATGCGGACTTCTTGGTAGCTCCAAGAGTGGATTCCCTC
GTAAGTTCGGCTACGTCATTTACTGCAGCCTCTGCAAGCGGAGGAACTCC
ACTATGCACTTAGGGACTACTGATATCAAATTCGCCGCCGAAACCCGCAAG
ATGGTGCTCTTTAACTGGCCAATACATAGCCCAGTGAAACTGTTCGCATAT
GGCGAACCTTTCTGCGCCACTTGTTTCGCGCACGTTTAGGAGCTTATTAGC
TAAATGAACCAGTTCTCTGGAGTGATACAGACTTGCGGCGTCCCGTAAACC
GAGAGTAACTTAACCATAAAGCTGGTGGGTATAGAACATATAGCGATCAGT
ACGGCCATTTGACGGCAAATACCGTCTGGCTGGCAAGTCGGGCTGATGAA
ATGCCTGACAGAACTTGAACTGACCAGAAGTGAGCAAAGGCGGTCTCAAT
TAACACTTTCCTATACGACACGTTGA

Supporting information: Gel Electrophoresis

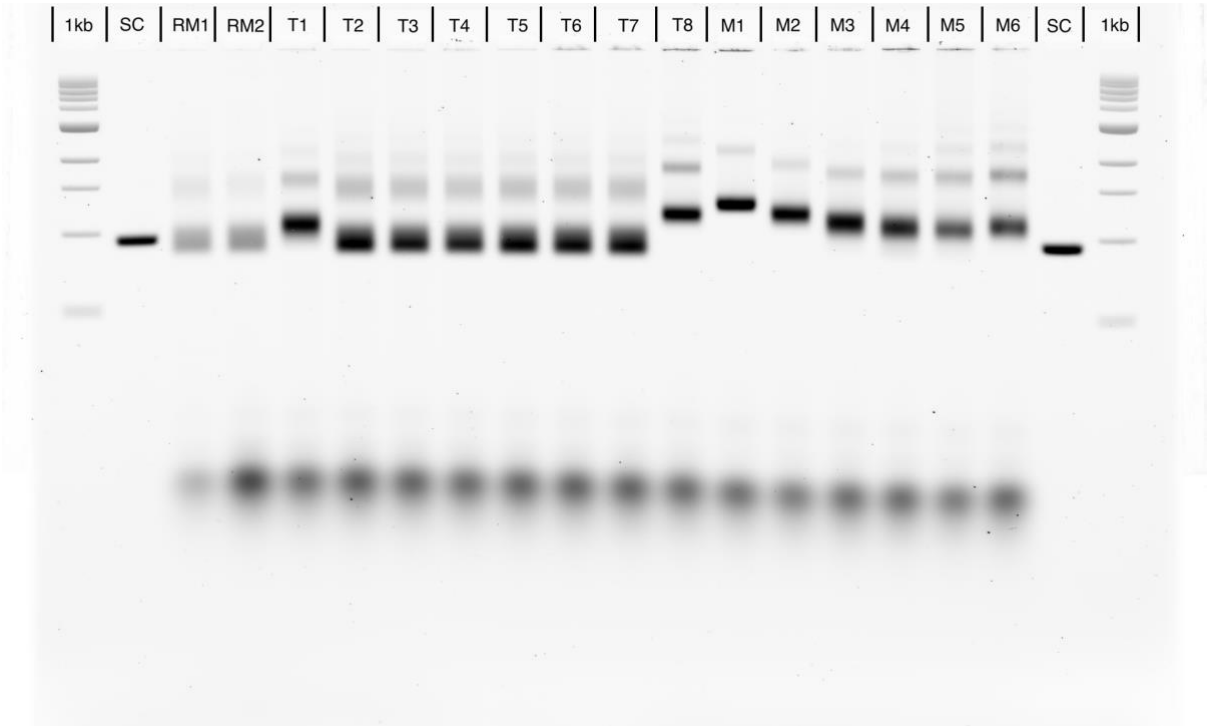

Figure 25: Fluorescent Gel Electrophoresis of V1 Initial Folding Screen: a 2% agarose gel image is displayed, run with 5.5 mM MgCl2 at 90 V for 2 hours. The gel lanes are loaded with a 1kb DNA ladder (1kb), a 2873 nucleotide scaffold strand (SC), and samples from folding conditions RM1 and RM2 with a 60 to 44 °C interval and 20 mM MgCl2 at scaffold-to-staple ratios of 1:4 and 1:10, respectively. Additionally, lanes T1-T8 represent a 20 mM MgCl2 condition with varying temperature intervals (T1 at 50 to 47 °C, escalating to T8 at 64 to 61 °C). The lanes labeled M5-M30 correspond to a 60 to 44 °C interval with increasing MgCl2 concentrations from 5 mM (M5) to 30 mM (M30).

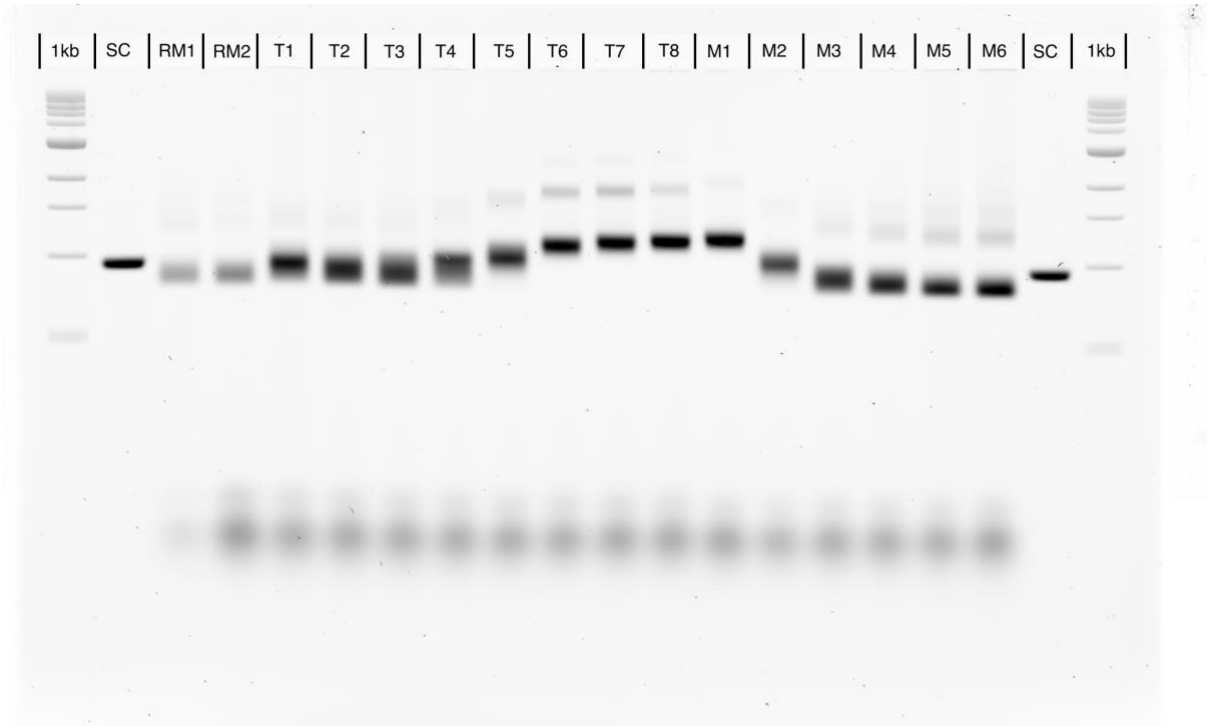

Figure 26: V2 Initial Folding Evaluation: This image captures a 2% agarose gel fluorescence following electrophoresis with 5.5 mM MgCl2 at 90 V for 120 minutes. The gel delineates lanes with a 1kb standard ladder (1kb), a 2873 nucleotide scaffold DNA (SC), and samples processed under RM1 and RM2 conditions with a 60 to 44 °C folding range and 20 mM MgCl2 at scaffold to staple ratios of 1:4 and 1:10, respectively. Lanes T1 through T8 correspond to folding tests at 20 mM MgCl2 across varying temperature ranges (T1 at 50 to 47 °C through T8 at 64 to 61 °C). Further, lanes M5 through M30 depict the same temperature range (60 to 44 °C) with increasing MgCl2 concentrations, from 5 mM (M5) up to 30 mM (M30).

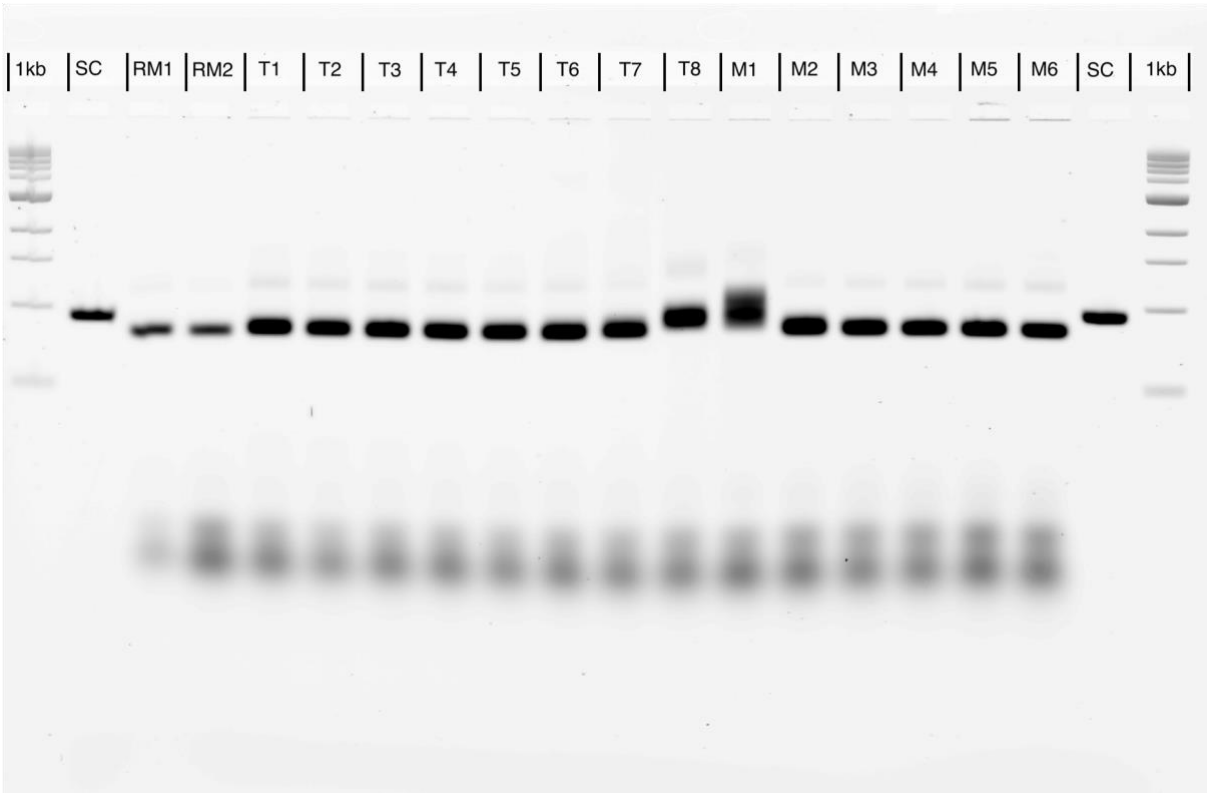

Figure 27: V3 Initial Folding Assessment: A 2% agarose gel visualized by fluorescent gel electrophoresis with 5.5 mM MgCl2 and electrophoresed at 90 V for 120 minutes is presented. The gel displays lanes containing a 1kb DNA ladder (1kb), a 2873 nucleotide long scaffold strand (SC), and folding condition samples RM1 and RM2 with a thermal range of 60 to 44 °C and 20 mM MgCl2 at scaffold-to-staple ratios of 1:4 and 1:10, respectively. Additionally, lanes T1 through T8 showcase a 20 mM MgCl2 condition with varied folding intervals from 50 to 47 °C for T1 up to 64 to 61 °C for T8. Lanes M5 through M30 depict folding intervals of 60 to 44 °C with MgCl2 concentrations incrementing from 5 mM (M5) to 30 mM (M30).

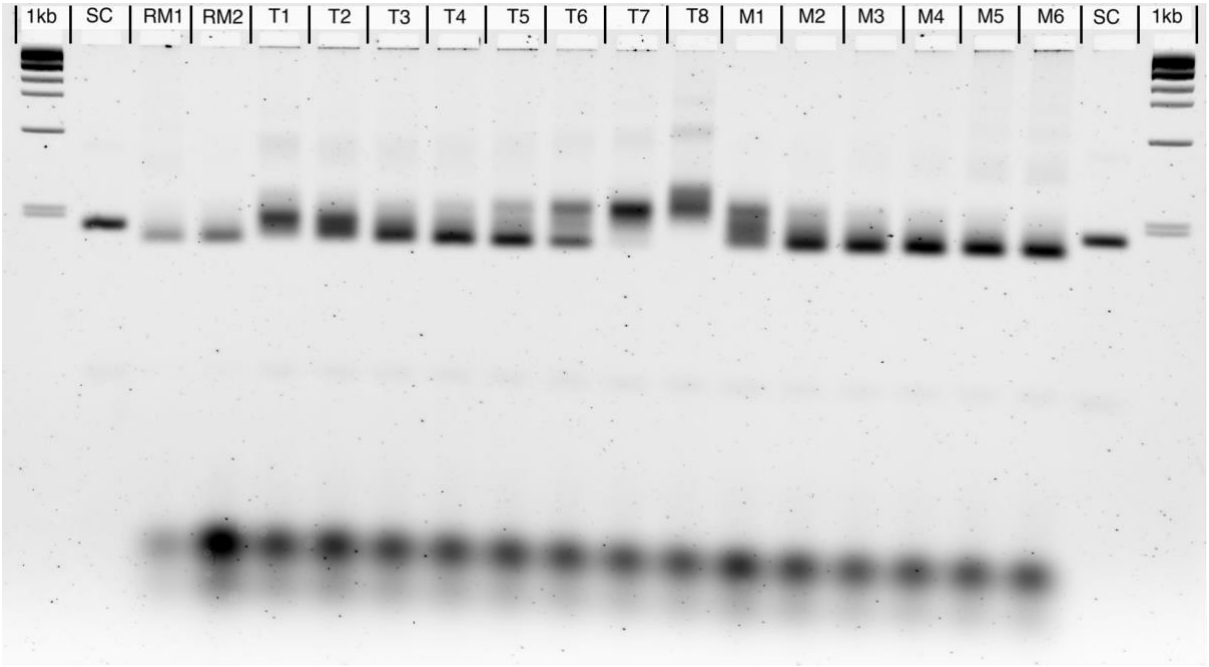

Figure 28: V4 Initial Folding Exploration: Displayed is a 2% agarose gel under fluorescent gel electrophoresis, embedded with 5.5 mM MgCl2, and subjected to a voltage of 90 V for a duration of 120 minutes. The gel features lanes with the following samples: a 1kb standard ladder (1kb), a 1033 nucleotide scaffold DNA strand (SC), folding samples RM1 and RM2 with a temperature range of 60 to 44 °C and 20 mM MgCl2 at 1:4 and 1:10 scaffold to staple ratios, respectively. The lanes T1 through T8 are set under a 20 mM MgCl2 environment, with progressive folding intervals ranging from 50 to 47 °C for T1, incrementing to 64 to 61 °C for T8. Additionally, lanes M5 to M30 represent folding with a consistent thermal range of 60 to 44 °C, while MgCl2 concentrations increase in 5 mM steps from 5 mM (M5) to 30 mM (M30).

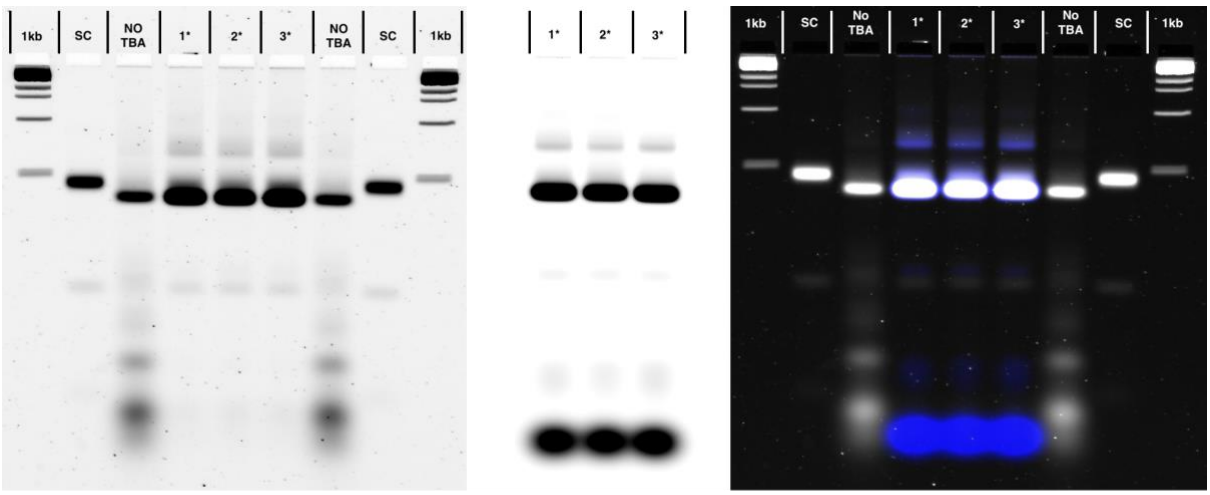

EtBr Channel **Cy5 Channel** **Merge channels**

Figure 29: Evaluation of Cy5-Labeled TBA Association with V4: The left gel illustrates three approaches: 1) Co-folding of origami with TBA, followed by chilling at 4°C. 2) Addition of TBA to pre-folded origami, left to incubate at room temperature overnight. 3) Origami is folded first, then TBA is added before the sample is cooled to 4°C and kept at this temperature. The middle gel, imaged in the Cy5 channel, shows fluorescent signals in lanes with TBA. The image on the right merges the ethidium bromide (EtBr) and Cy5 channel data, providing an enhanced view of the TBA binding sites.

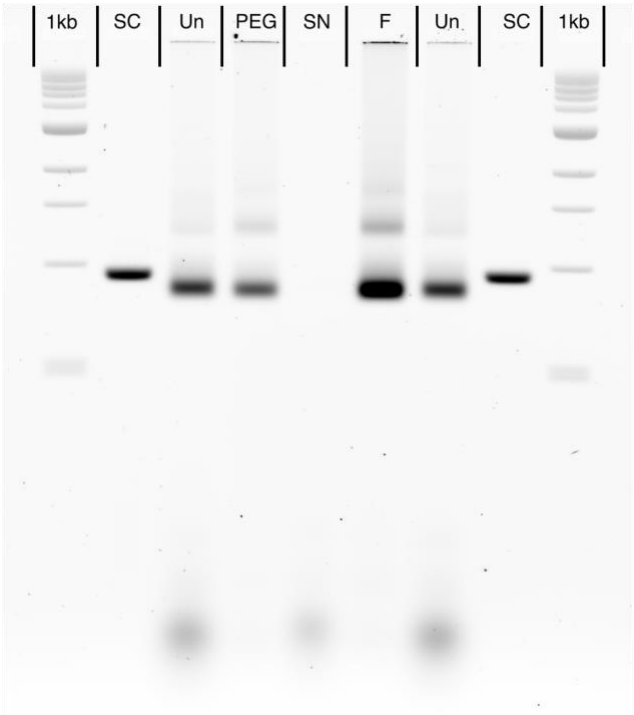

Figure 30: Purification Process for V2: The gel electrophoresis results exhibit multiple lanes, indicating the stages of purification. '1kb' represents the 1kb DNA marker, 'SC' corresponds to the 2873 nucleotide DNA scaffold, 'Un' shows the unpurified folded DNA origami, 'PEG' denotes the PEG-precipitated purified sample, 'SN' contains only the excess staples from the PEG purification supernatant, and 'F' indicates the sample further concentrated using an Amicon filter, prepared specifically for cryo-EM analysis.

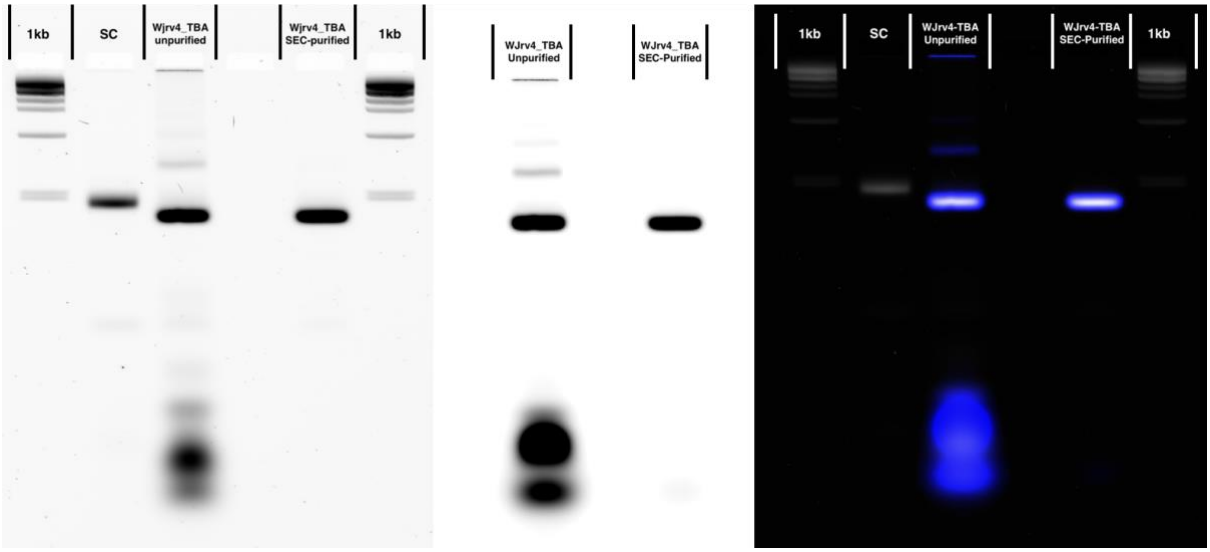

Figure 31: DNA Origami V4_TBA Purification Sequence: The purification workflow, incorporating size exclusion chromatography (SEC), is visualized through gel electrophoresis. From left to right, the lanes display a 1kb ladder, the scaffold strand, the unpurified origami construct, and the SEC-purified sample subsequently concentrated with Amicon filters. The central panel reveals the Cy5 channel, verifying the thrombin-binding aptamer (TBA) retention post-purification. The rightmost panel merges the channels, offering an integrated depiction of the purified DNA origami structure.

Supporting information: Cryo-EM Reconstructions

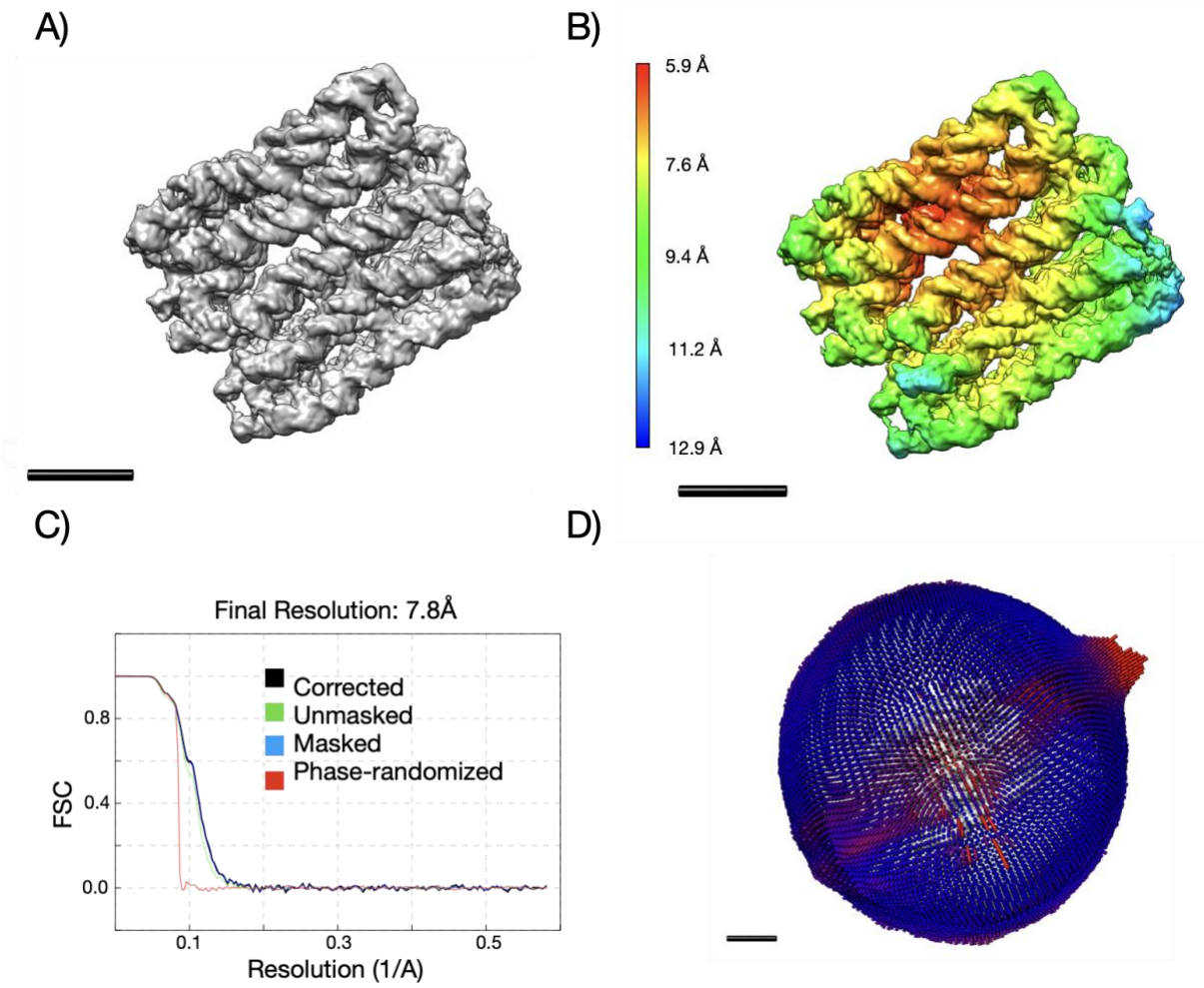

Figure 32: Cryo-EM Analysis of DNA Origami V4 Constructed with Desalted Purified Staple Oligos: A) The cryo-EM structural map. B) A local resolution map depicting the resolution variation ranging from 5.9Å to 12.9Å. C) The Fourier Shell Correlation (FSC) curve demonstrates an overall resolution of 7.8Å. D) The distribution of particle orientations.

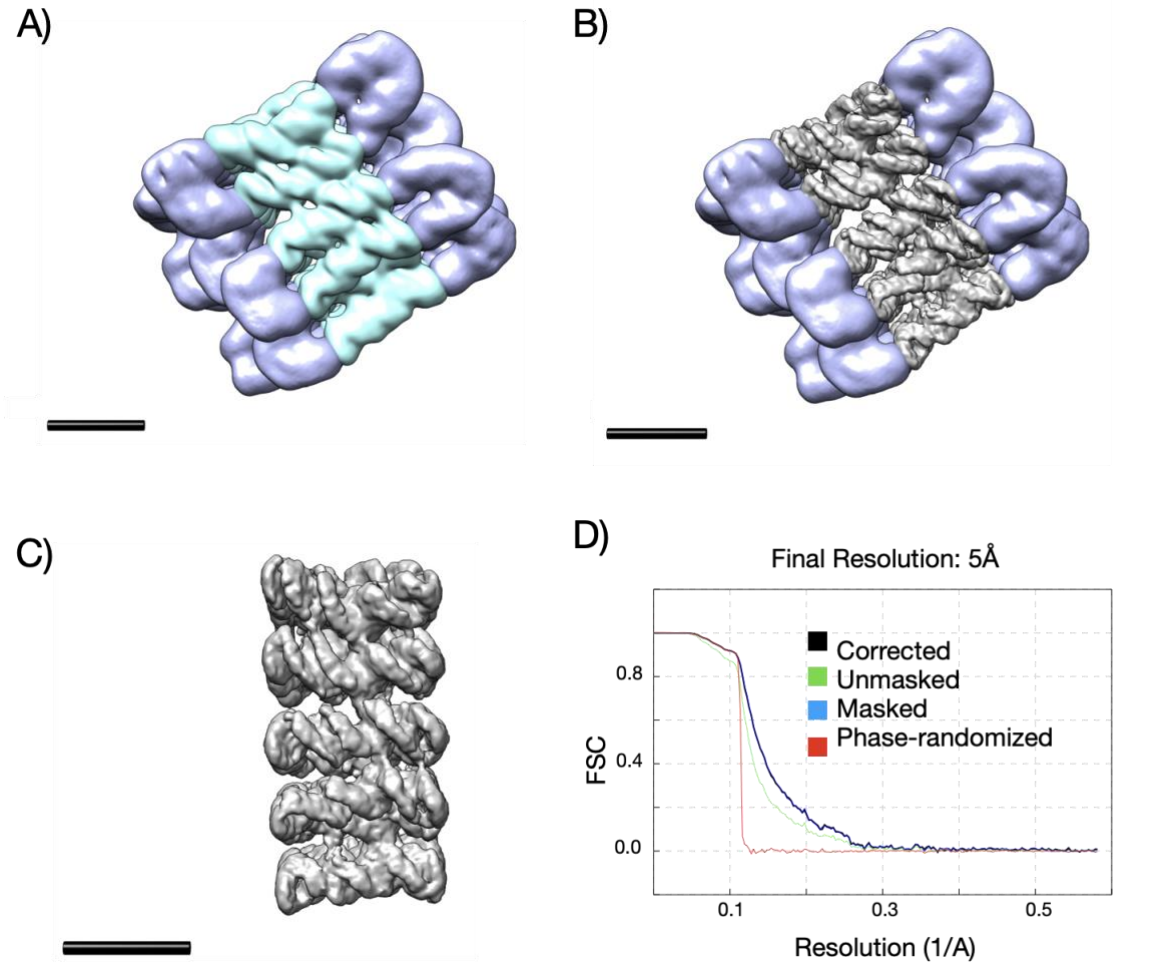

Figure 33: Enhancing Resolution of DNA Origami V4 with Desalted Purified Staples via Multibody Analysis: A) Isolation of the central, less flexible region from the more flexible ends of the DNA origami. B, C) Enhanced resolution of the central area achieved through Relion's multibody analysis. D) The Fourier Shell Correlation (FSC) curve for the central, less flexible region, indicating an improved resolution of 5Å.

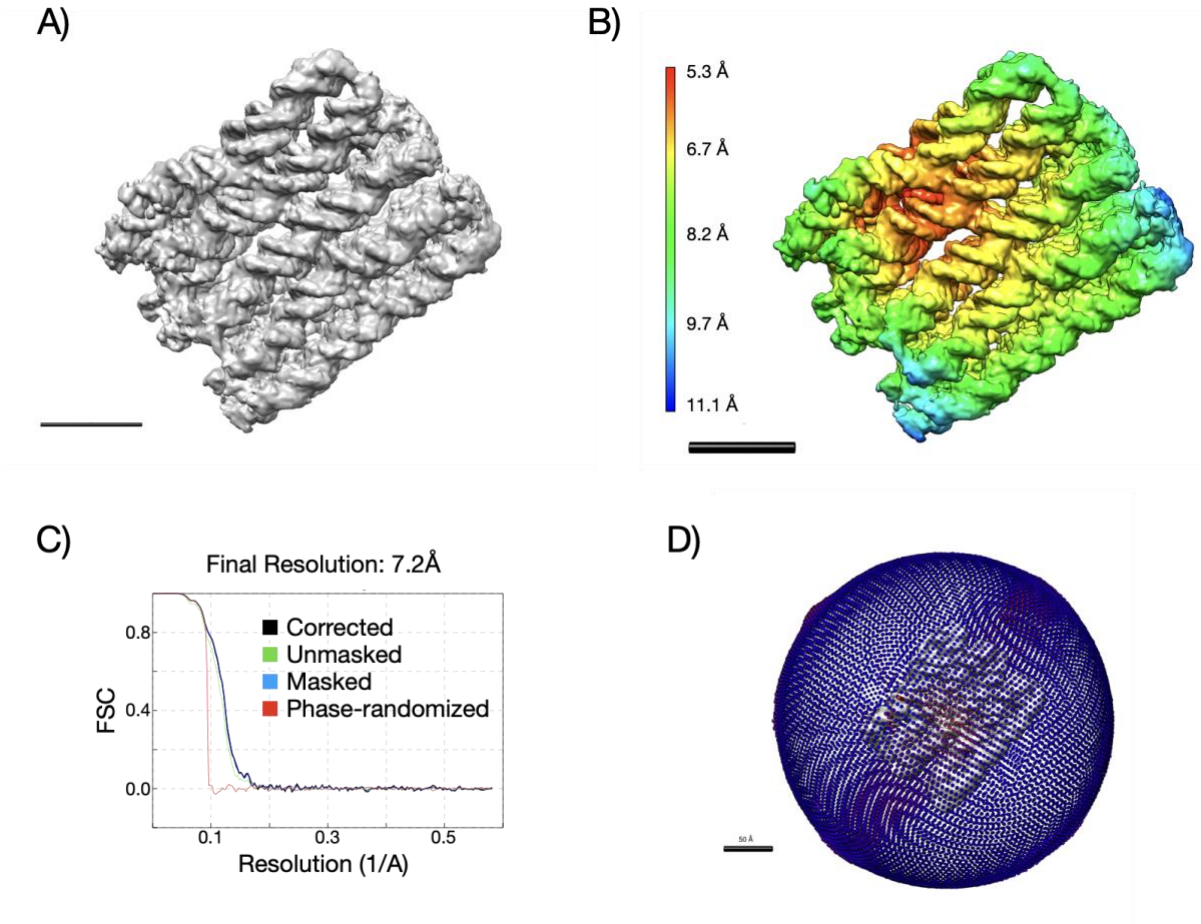

Figure 34: Cryo-EM Structural Analysis of DNA Origami V4 with HPLC Purified Staple Oligos: A) The cryo-EM map of the structure. B) Local resolution mapping, illustrating variations from 5.3Å to 11.1Å. C) Fourier Shell Correlation (FSC) curve, indicating an overall resolution of 7.2Å. D) Analysis of the orientation distribution of particles.

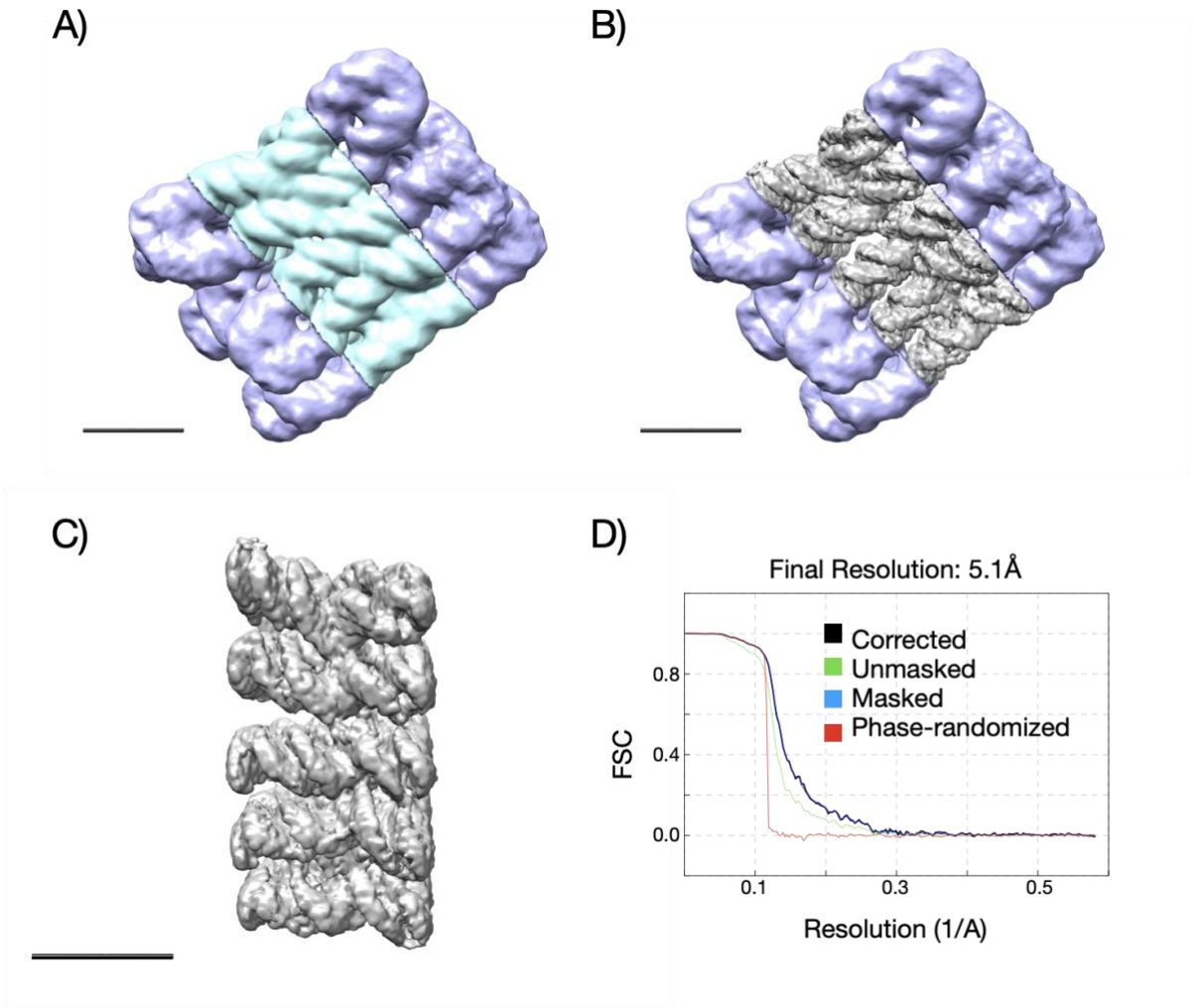

Figure 35: Resolution Enhancement of DNA Origami V4 Using HPLC Purified Staples Through Multibody Analysis: A) Differentiation of the central, more rigid segment from the flexible peripheral parts of the DNA origami structure. B, C) Resolution refinement in the central section conducted using Relion's multibody analysis technique. D) Fourier Shell Correlation (FSC) curve for the central, more stable region, revealing an enhanced resolution of 5.1Å.

Object	DNA origami Concentration (μM)	Grid Type	# of particles for refinement	# of fractions	Dose (e/A^2)	Pixel size (A/pix)	Resolution of resulting 3D map (A)
V1	3	Quantifoil 1.2/1.3-200 mesh	140317	13	51	1.4	8.6
V2	6.75	Quantifoil 1.2/1.3-200 mesh	151581	20	50	0.86	7.5
V3	8	Quantifoil 1.2/1.3-Au, 300 mesh	295463	10	50	1.4	8.3
V4_SD	14.1	Quantifoil -1.2/1.3-200 mesh	408927	20	50	0.86	7.8
V4_HPLC	10.3	Quantifoil -1.2/1.3-200 mesh	389297	20	50	0.86	7.2
V4_TBA	10	Quantifoil -1.2/1.3-200 mesh	966383	20	50	0.86	7.5
V4_TBA_Thrombin	10.5	Quantifoil -1.2/1.3-200 mesh	133161	20	40	0.86	9.3

Supplementary Table 1 | Cryo-EM grid preparation and imaging conditions.

References

1. Rothemund, P.W., *Folding DNA to create nanoscale shapes and patterns.* Nature, 2006. 440(7082): p. 297-302.
2. Ramezani, H. and H. Dietz, *Building machines with DNA molecules.* Nature Reviews Genetics, 2020. 21(1): p. 5-26.
3. Andersen, E.S., et al., *Self-assembly of a nanoscale DNA box with a controllable lid.* Nature, 2009. 459(7243): p. 73-76.
4. Benson, E., et al., *DNA rendering of polyhedral meshes at the nanoscale.* Nature, 2015. 523(7561): p. 441-444.
5. Dietz, H., S.M. Douglas, and W.M. Shih, *Folding DNA into twisted and curved nanoscale shapes.* Science, 2009. 325(5941): p. 725-730.
6. Douglas, S.M., et al., *Self-assembly of DNA into nanoscale three-dimensional shapes.* Nature, 2009. 459(7245): p. 414-418.
7. Douglas, S.M., et al., *Rapid prototyping of 3D DNA-origami shapes with caDNAno.* Nucleic Acids Research, 2009. 37(15): p. 5001-5006.
8. Ke, Y., et al., *Multilayer DNA Origami Packed on a Square Lattice.* Journal of the American Chemical Society, 2009. 131(43): p. 15903-15908.
9. Sobczak, J.-P.J., et al., *Rapid folding of DNA into nanoscale shapes at constant temperature.* Science, 2012. 338(6113): p. 1458-1461.
10. Veneziano, R., et al., *Designer nanoscale DNA assemblies programmed from the top down.* Science, 2016. 352(6293): p. 1534-1534.
11. Ke, Y., et al., *Two design strategies for enhancement of multilayer-DNA-origami folding: underwinding for specific intercalator rescue and staple-break positioning.* Chemical science, 2012. 3 8: p. 2587-2597.
12. Ma, Z., et al., *Rhombic-Shaped Nanostructures and Mechanical Properties of 2D DNA Origami Constructed with Different Crossover/Nick Designs.* Small, 2018. 14(1): p. 1702028.
13. Kuzuya, A. and M. Komiyama, *DNA origami: Fold, stick, and beyond.* Nanoscale, 2010. 2(3): p. 309-321.
14. Kube, M., et al., *Revealing the structures of megadalton-scale DNA complexes with nucleotide resolution.* Nature Communications, 2020. 11(1): p. 6229.
15. Wang, H.-W. and J.-W. Wang, *How cryo-electron microscopy and X-ray crystallography complement each other.* Protein Science, 2017. 26(1): p. 32-39.
16. Weissenberger, G., R.J.M. Henderikx, and P.J. Peters, *Understanding the invisible hands of sample preparation for cryo-EM.* Nature Methods, 2021. 18(5): p. 463-471.
17. Adrian, M., et al., *Cryo-electron microscopy of viruses.* Nature, 1984. 308(5954): p. 32-36.
18. Merk, A., et al., *Breaking cryo-EM resolution barriers to facilitate drug discovery.* Cell, 2016. 165(7): p. 1698-1707.
19. Bai, X.-c., et al., *Cryo-EM structure of a 3D DNA-origami object.* Proceedings of the National Academy of Sciences, 2012. 109(49): p. 20012-20017.

20. Bertosin, E., et al., *Cryo-electron microscopy and mass analysis of oligolysine-coated DNA nanostructures.* ACS nano, 2021. 15(6): p. 9391-9403.
21. Nogales, E. and S.H. Scheres, *Cryo-EM: a unique tool for the visualization of macromolecular complexity.* Molecular cell, 2015. 58(4): p. 677-689.
22. Herzik, M.A., M. Wu, and G.C. Lander, *High-resolution structure determination of sub-100 kDa complexes using conventional cryo-EM.* Nature Communications, 2019. 10(1): p. 1032.
23. Sigworth, F.J., *Principles of cryo-EM single-particle image processing.* Journal of Electron Microscopy, 2015. 65(1): p. 57-67.
24. Henderson, R., *The potential and limitations of neutrons, electrons and X-rays for atomic resolution microscopy of unstained biological molecules.* Quarterly reviews of biophysics, 1995. 28(2): p. 171-193.
25. Danev, R., et al., *Volta potential phase plate for in-focus phase contrast transmission electron microscopy.* Proceedings of the National Academy of Sciences, 2014. 111(44): p. 15635-15640.
26. Fan, X., et al., *Single particle cryo-EM reconstruction of 52 kDa streptavidin at 3.2 Angstrom resolution.* Nature Communications, 2019. 10(1): p. 2386.
27. McMullan, G., A.R. Faruqi, and R. Henderson, *Chapter One - Direct Electron Detectors*, in *Methods in Enzymology*, R.A. Crowther, Editor. 2016, Academic Press. p. 1-17.
28. Palovcak, E., et al., *Enhancing the signal-to-noise ratio and generating contrast for cryo-EM images with convolutional neural networks.* IUCrJ, 2020. 7(Pt 6): p. 1142-1150.
29. Yeates, T.O., *Geometric Principles for Designing Highly Symmetric Self-Assembling Protein Nanomaterials.* Annual Review of Biophysics, 2017. 46(1): p. 23-42.
30. King, N.P., et al., *Computational design of self-assembling protein nanomaterials with atomic level accuracy.* Science, 2012. 336(6085): p. 1171-4.
31. Liu, Y., et al., *Near-atomic cryo-EM imaging of a small protein displayed on a designed scaffolding system.* Proceedings of the National Academy of Sciences, 2018. 115(13): p. 3362-3367.
32. Liu, Y., D.T. Huynh, and T.O. Yeates, *A 3.8 Å resolution cryo-EM structure of a small protein bound to an imaging scaffold.* Nature Communications, 2019. 10(1): p. 1864.
33. Erramilli, S.K., et al., *Cryo-EM structures of a synthetic antibody against 22 kDa claudin-4 reveal its complex with Clostridium perfringens enterotoxin.* bioRxiv, 2023: p. 2023.06.12.544689.
34. Aksel, T., et al., *Molecular goniometers for single-particle cryo-electron microscopy of DNA-binding proteins.* Nat Biotechnol, 2021. 39(3): p. 378-386.
35. Zhou, Y., J. Dong, and Q. Wang, *Fabricating higher-order functional DNA origami structures to reveal biological processes at multiple scales.* NPG Asia Materials, 2023. 15(1): p. 25.
36. Alberts, B., *Molecular biology of the cell*. 2017: Garland science.
37. Goldberg, M., R. Langer, and X. Jia, *Nanostructured materials for applications in drug delivery and tissue engineering.* Journal of Biomaterials Science, Polymer Edition, 2007. 18(3): p. 241-268.
38. Liechty, W.B., et al., *Polymers for drug delivery systems.* Annual review of chemical and biomolecular engineering, 2010. 1: p. 149-173.

39. Doll, T.A., et al., *Nanoscale assemblies and their biomedical applications.* Journal of The Royal Society Interface, 2013. 10(80): p. 20120740.
40. Green, J.J. and J.H. Elisseeff, *Mimicking biological functionality with polymers for biomedical applications.* Nature, 2016. 540(7633): p. 386-394.
41. Goldberg, M.S., *Improving cancer immunotherapy through nanotechnology.* Nature Reviews Cancer, 2019. 19(10): p. 587-602.
42. Seeman, N.C., *DNA in a material world.* Nature, 2003. 421(6921): p. 427-431.
43. Seeman, N.C., *Nanomaterials based on DNA.* Annual review of biochemistry, 2010. 79: p. 65-87.
44. Lin, C., Y. Liu, and H. Yan, *Designer DNA nanoarchitectures.* Biochemistry, 2009. 48(8): p. 1663-1674.
45. Zhang, F., et al., *Structural DNA nanotechnology: state of the art and future perspective.* Journal of the American Chemical Society, 2014. 136(32): p. 11198-11211.
46. Seeman, N.C. and H.F. Sleiman, *DNA nanotechnology.* Nature Reviews Materials, 2017. 3(1): p. 1-23.
47. Watson, J.D. and F.H. Crick, *Molecular structure of nucleic acids: a structure for deoxyribose nucleic acid.* Nature, 1953. 171(4356): p. 737-738.
48. Zadegan, R.M. and M.L. Norton, *Structural DNA nanotechnology: from design to applications.* International journal of molecular sciences, 2012. 13(6): p. 7149-7162.
49. Winfree, E., et al., *Design and self-assembly of two-dimensional DNA crystals.* Nature, 1998. 394(6693): p. 539-544.
50. LaBean, T.H., et al., *Construction, analysis, ligation, and self-assembly of DNA triple crossover complexes.* Journal of the American Chemical Society, 2000. 122(9): p. 1848-1860.
51. Chen, J. and N.C. Seeman, *Synthesis from DNA of a molecule with the connectivity of a cube.* Nature, 1991. 350(6319): p. 631-633.
52. Rothemund, P.W.K., *Folding DNA to create nanoscale shapes and patterns.* Nature, 2006. 440(7082): p. 297-302.
53. Maune, H.T., et al., *Self-assembly of carbon nanotubes into two-dimensional geometries using DNA origami templates.* Nature Nanotechnology, 2010. 5(1): p. 61-66.
54. Gerling, T., et al., *Dynamic DNA devices and assemblies formed by shape-complementary, non–base pairing 3D components.* Science, 2015. 347(6229): p. 1446-1452.
55. Douglas, S.M., I. Bachelet, and G.M. Church, *A Logic-Gated Nanorobot for Targeted Transport of Molecular Payloads.* Science, 2012. 335(6070): p. 831-834.
56. Woods, D., et al., *Diverse and robust molecular algorithms using reprogrammable DNA self-assembly.* Nature, 2019. 567(7748): p. 366-372.
57. Le, J.V., et al., *Probing Nucleosome Stability with a DNA Origami Nanocaliper.* ACS Nano, 2016. 10(7): p. 7073-7084.
58. Wagenbauer, K.F., et al., *How We Make DNA Origami.* ChemBioChem, 2017. 18(19): p. 1873-1885.
59. Andersen, E.S., et al., *Self-assembly of a nanoscale DNA box with a controllable lid.* Nature, 2009. 459(7243): p. 73-76.

60. Bush, J., et al., *Synthesis of DNA Origami Scaffolds: Current and Emerging Strategies.* Molecules, 2020. 25(15): p. 3386.
61. Ketterer, P., E.M. Willner, and H. Dietz, *Nanoscale rotary apparatus formed from tight-fitting 3D DNA components.* Science Advances, 2016. 2(2): p. e1501209.
62. Ramakrishnan, S., et al., *Structural stability of DNA origami nanostructures under application-specific conditions.* Computational and structural biotechnology journal, 2018. 16: p. 342-349.
63. Bila, H., E.E. Kurisinkal, and M.M. Bastings, *Engineering a stable future for DNA-origami as a biomaterial.* Biomaterials science, 2019. 7(2): p. 532-541.
64. Keller, A. and V. Linko, *Challenges and perspectives of DNA nanostructures in biomedicine.* Angewandte Chemie International Edition, 2020. 59(37): p. 15818-15833.
65. Julin, S., et al., *DNA-Origami-Templated Growth of Multilamellar Lipid Assemblies.* Angewandte Chemie International Edition, 2021. 60(2): p. 827-833.
66. Schreiber, R., et al., *DNA origami-templated growth of arbitrarily shaped metal nanoparticles.* Small, 2011. 7(13): p. 1795-1799.
67. Weizenmann, N., et al., *Chemical ligation of an entire DNA origami nanostructure.* Nanoscale, 2021. 13(41): p. 17556-17565.
68. Ramakrishnan, S., et al., *Enhancing the stability of DNA origami nanostructures: staple strand redesign versus enzymatic ligation.* Nanoscale, 2019. 11(35): p. 16270-16276.
69. Gerling, T., et al., *Sequence-programmable covalent bonding of designed DNA assemblies. Sci. Adv. 4, eaau1157*. 2018.
70. Hahn, J., et al., *Addressing the instability of DNA nanostructures in tissue culture.* ACS nano, 2014. 8(9): p. 8765-8775.
71. Kollmann, F., et al., *Superstructure-dependent loading of DNA origami nanostructures with a groove-binding drug.* ACS omega, 2018. 3(8): p. 9441-9448.
72. Liu, Q., et al., *Enhanced stability of DNA nanostructures by incorporation of unnatural base pairs.* ChemPhysChem, 2017. 18(21): p. 2977-2980.
73. Castro, C.E., et al., *Mechanical design of DNA nanostructures.* Nanoscale, 2015. 7(14): p. 5913-5921.
74. Plesa, C., et al., *Ionic permeability and mechanical properties of DNA origami nanoplates on solid-state nanopores.* ACS nano, 2014. 8(1): p. 35-43.
75. Chandrasekaran, A.R., et al., *Exceptional nuclease resistance of paranemic crossover (PX) DNA and crossover-dependent biostability of DNA motifs.* Journal of the American Chemical Society, 2020. 142(14): p. 6814-6821.
76. Ma, Z., et al., *Tuning porosity and radial mechanical properties of DNA origami nanotubes via crossover design.* Japanese Journal of Applied Physics, 2017. 56(6S1): p. 06GJ02.
77. Kim, D.-N., et al., *Quantitative prediction of 3D solution shape and flexibility of nucleic acid nanostructures.* Nucleic acids research, 2012. 40(7): p. 2862-2868.
78. Dunn, K.E., et al., *Guiding the folding pathway of DNA origami.* Nature, 2015. 525(7567): p. 82-86.

79. Ramakrishnan, S., et al., *Structural stability of DNA origami nanostructures in the presence of chaotropic agents.* Nanoscale, 2016. 8(19): p. 10398-10405.
80. Xin, Y., et al., *Environment-Dependent Stability and Mechanical Properties of DNA Origami Six-Helix Bundles with Different Crossover Spacings.* Small, 2022. 18(18): p. 2107393.
81. Funke, J.J., et al., *Exploring Nucleosome Unwrapping Using DNA Origami.* Nano Letters, 2016. 16(12): p. 7891-7898.
82. Funke, J.J., et al., *Uncovering the forces between nucleosomes using DNA origami.* Science Advances, 2016. 2(11): p. e1600974.
83. Robertson, D.L. and G.F. Joyce, *Selection in vitro of an RNA enzyme that specifically cleaves single-stranded DNA.* Nature, 1990. 344(6265): p. 467-468.
84. Tuerk, C. and L. Gold, *Systematic Evolution of Ligands by Exponential Enrichment: RNA Ligands to Bacteriophage T4 DNA Polymerase.* Science, 1990. 249(4968): p. 505-510.
85. Ellington, A.D. and J.W. Szostak, *In vitro selection of RNA molecules that bind specific ligands.* Nature, 1990. 346(6287): p. 818-822.
86. Langecker, M., et al., *Synthetic Lipid Membrane Channels Formed by Designed DNA Nanostructures.* Science, 2012. 338(6109): p. 932-936.
87. Sigl, C., et al., *Programmable icosahedral shell system for virus trapping.* Nature Materials, 2021. 20(9): p. 1281-1289.
88. Kretzmann, J.A., et al., *Gene-encoding DNA origami for mammalian cell expression.* Nature Communications, 2023. 14(1): p. 1017.
89. Williams, D.B. and C.B. Carter, *Transmission electron microscopy : a textbook for materials science*. 2nd ed. 2008, New York: Springer.
90. Franken, L.E., et al., *A Technical Introduction to Transmission Electron Microscopy for Soft-Matter: Imaging, Possibilities, Choices, and Technical Developments.* Small, 2020. 16(14): p. 1906198.
91. James, E.M. and J.M. Rodenburg, *A method for measuring the effective source coherence in a field emission transmission electron microscope.* Applied Surface Science, 1997. 111: p. 174-179.
92. Tiemeijer, P.C., et al., *Using a monochromator to improve the resolution in TEM to below 0.5Å. Part I: Creating highly coherent monochromated illumination.* Ultramicroscopy, 2012. 114: p. 72-81.
93. Iiyoshi, R. and S. Maruse, *Tungsten-Point-Cathode Electron Gun Using Electron Bombardment for Cathode Tip Heating: Cathode Life and Operating Characteristics at Cathode Temperatures above 2,800 K.* Journal of Electron Microscopy, 1996. 45(2): p. 128-134.
94. Schmidt, P.H., et al., *Design and optimization of directly heated LaB6 cathode assemblies for electron-beam instruments.* Journal of Vacuum Science and Technology, 1978. 15(4): p. 1554-1560.
95. Egerton, R.F., *Choice of operating voltage for a transmission electron microscope.* Ultramicroscopy, 2014. 145: p. 85-93.
96. Peet, M.J., R. Henderson, and C.J. Russo, *The energy dependence of contrast and damage in electron cryomicroscopy of biological molecules.* Ultramicroscopy, 2019. 203: p. 125-131.
97. Koster, A.J. and W.J. de Ruijter, *Practical autoalignment of transmission electron microscopes.* Ultramicroscopy, 1992. 40(2): p. 89-107.
98. Glaeser, R.M., et al., *Precise beam-tilt alignment and collimation are required to minimize the phase error associated with coma in high-resolution cryo-EM.* Journal of Structural Biology, 2011. 174(1): p. 1-10.

99. Sawada, H., et al., *Experimental evaluation of a spherical aberration-corrected TEM and STEM.* Microscopy, 2005. 54(2): p. 119-121.
100. Franken, L.E., E.J. Boekema, and M.C.A. Stuart, *Transmission Electron Microscopy as a Tool for the Characterization of Soft Materials: Application and Interpretation.* Advanced Science, 2017. 4(5): p. 1600476.
101. Brenner, S. and R.W. Horne, *A negative staining method for high resolution electron microscopy of viruses.* Biochimica et Biophysica Acta, 1959. 34: p. 103-110.
102. Glaeser, R.M., *How good can cryo-EM become?* Nature Methods, 2016. 13(1): p. 28-32.
103. Zhu, D., et al., *An electron counting algorithm improves imaging of proteins with low-acceleration-voltage cryo-electron microscope.* Communications Biology, 2022. 5(1): p. 321.
104. Fresnel, A., *Oeuvres complètes*. Vol. 2. 1868: Imprimerie impériale.
105. Frank, J., *Three-Dimensional Electron Microscopy of Macromolecular Assemblies: Visualization of Biological Molecules in Their Native State*. 2006: Oxford University Press.
106. Henderson, R. and P.N.T. Unwin, *Three-dimensional model of purple membrane obtained by electron microscopy.* Nature, 1975. 257(5521): p. 28-32.
107. De Rosier, D.J. and A. Klug, *Reconstruction of Three Dimensional Structures from Electron Micrographs.* Nature, 1968. 217(5124): p. 130-134.
108. Henderson, R., et al., *Model for the structure of bacteriorhodopsin based on high-resolution electron cryo-microscopy.* Journal of Molecular Biology, 1990. 213(4): p. 899-929.
109. Frank, J., *Averaging of low exposure electron micrographs of non-periodic objects.* Ultramicroscopy, 1975. 1(2): p. 159-162.
110. van Heel, M. and J. Frank, *Use of multivariates statistics in analysing the images of biological macromolecules.* Ultramicroscopy, 1981. 6(1): p. 187-194.
111. Radermacher, M., et al., *A NEW 3-D RECONSTRUCTION SCHEME APPLIED TO THE 50S RIBOSOMAL SUBUNIT OF E. COLI.* Journal of Microscopy, 1986. 141(1): p. RP1-RP2.
112. Taylor, K.A. and R.M. Glaeser, *Electron Diffraction of Frozen, Hydrated Protein Crystals.* Science, 1974. 186(4168): p. 1036-1037.
113. Dubochet, J. and A.W. McDowall, *VITRIFICATION OF PURE WATER FOR ELECTRON MICROSCOPY.* Journal of Microscopy, 1981. 124(3): p. 3-4.
114. Dubochet, J., et al., *Cryo-electron microscopy of vitrified specimens.* Quarterly Reviews of Biophysics, 1988. 21(2): p. 129-228.
115. Shen, P.S., *The 2017 Nobel Prize in Chemistry: cryo-EM comes of age.* Analytical and Bioanalytical Chemistry, 2018. 410(8): p. 2053-2057.
116. Scheres, S.H., *RELION: implementation of a Bayesian approach to cryo-EM structure determination.* Journal of structural biology, 2012. 180(3): p. 519-530.
117. Zheng, S.Q., et al., *MotionCor2: anisotropic correction of beam-induced motion for improved cryo-electron microscopy.* Nature Methods, 2017. 14(4): p. 331-332.
118. Cheng, Y., et al., *A primer to single-particle cryo-electron microscopy.* Cell, 2015. 161(3): p. 438-449.

119. Roseman, A., *FindEM—a fast, efficient program for automatic selection of particles from electron micrographs.* Journal of structural biology, 2004. 145(1-2): p. 91-99.
120. Chen, J.Z. and N. Grigorieff, *SIGNATURE: a single-particle selection system for molecular electron microscopy.* Journal of structural biology, 2007. 157(1): p. 168-173.
121. Voss, N., et al., *DoG Picker and TiltPicker: software tools to facilitate particle selection in single particle electron microscopy.* Journal of structural biology, 2009. 166(2): p. 205-213.
122. Ludtke, S.J., P.R. Baldwin, and W. Chiu, *EMAN: semiautomated software for high-resolution single-particle reconstructions.* Journal of structural biology, 1999. 128(1): p. 82-97.
123. Wang, F., et al., *DeepPicker: A deep learning approach for fully automated particle picking in cryo-EM.* Journal of structural biology, 2016. 195(3): p. 325-336.
124. Zhu, Y., Q. Ouyang, and Y. Mao, *A deep convolutional neural network approach to single-particle recognition in cryo-electron microscopy.* BMC bioinformatics, 2017. 18: p. 1-10.
125. Tegunov, D. and P. Cramer, *Real-time cryo-electron microscopy data preprocessing with Warp.* Nature methods, 2019. 16(11): p. 1146-1152.
126. Bepler, T., et al., *Topaz-Denoise: general deep denoising models for cryoEM and cryoET.* Nature communications, 2020. 11(1): p. 5208.
127. Wagner, T., et al., *SPHIRE-crYOLO is a fast and accurate fully automated particle picker for cryo-EM.* Communications biology, 2019. 2(1): p. 218.
128. Zhang, X., et al., *EPicker is an exemplar-based continual learning approach for knowledge accumulation in cryoEM particle picking.* Nature Communications, 2022. 13(1): p. 2468.
129. van Heel, M. and M. Stöffler-Meilicke, *Characteristic views of E. coli and B. stearothermophilus 30S ribosomal subunits in the electron microscope.* The EMBO journal, 1985. 4(9): p. 2389-2395.
130. Dari, K., et al., *New tools for automated cryo-EM single-particle analysis in RELION-4.0.* bioRxiv, 2021: p. 2021.09.30.462538.
131. Penczek, P.A., *Resolution measures in molecular electron microscopy*, in *Methods in enzymology*. 2010, Elsevier. p. 73-100.
132. Rosenthal, P.B. and R. Henderson, *Optimal determination of particle orientation, absolute hand, and contrast loss in single-particle electron cryomicroscopy.* Journal of molecular biology, 2003. 333(4): p. 721-745.
133. Khoshouei, A., et al., *Designing Rigid DNA Origami Templates for Molecular Visualization Using Cryo-EM.* Nano Letters, 2024. 24(16): p. 5031-5038.
134. Rohou, A. and N. Grigorieff, *CTFFIND4: Fast and accurate defocus estimation from electron micrographs.* Journal of Structural Biology, 2015. 192(2): p. 216-221.
135. Wagner, T., et al., *SPHIRE-crYOLO is a fast and accurate fully automated particle picker for cryo-EM.* Communications Biology, 2019. 2(1): p. 218.
136. Pettersen, E.F., et al., *UCSF Chimera--a visualization system for exploratory research and analysis.* J Comput Chem, 2004. 25(13): p. 1605-12.
137. Sanchez-Garcia, R., et al., *DeepEMhancer: a deep learning solution for cryo-EM volume post-processing.* Communications Biology, 2021. 4(1): p. 874.

138. Kaur, S., et al., *Local computational methods to improve the interpretability and analysis of cryo-EM maps.* Nature Communications, 2021. 12(1): p. 1240.
139. Emsley, P., et al., *Features and development of Coot.* Acta Crystallographica Section D, 2010. 66(4): p. 486-501.
140. Croll, T., *ISOLDE: a physically realistic environment for model building into low-resolution electron-density maps.* Acta Crystallographica Section D, 2018. 74(6): p. 519-530.
141. Pettersen, E.F., et al., *UCSF ChimeraX: Structure visualization for researchers, educators, and developers.* Protein Science, 2021. 30(1): p. 70-82.
142. Wang, R.Y.-R., et al., *Automated structure refinement of macromolecular assemblies from cryo-EM maps using Rosetta.* eLife, 2016. 5: p. e17219.
143. Afonine, P.V., et al., *Real-space refinement in PHENIX for cryo-EM and crystallography.* Acta Crystallographica Section D, 2018. 74(6): p. 531-544.

Acknowledgments

I would like to express my deepest gratitude to my supervisor, Professor Hendrik Dietz. His support and guidance have been invaluable throughout my PhD journey. Working in his lab with access to state-of-the-art equipment has been a remarkable experience. Professor Dietz is one of the most influential people in my life, and I will be forever grateful to him for his mentorship and inspiration.

I am deeply grateful to my colleagues at DietzLab. The collaborative and friendly atmosphere in the lab made it an incredibly rewarding place to work and grow as a researcher.

Special thanks go to my friends, particularly Aryan, for their unwavering emotional support. Aryan, your willingness to listen and comfort me whenever needed has been a significant strength.

To my mother, who has always been there for me emotionally, offering endless love and encouragement, I cannot thank you enough for your support.

A heartfelt thank you to my dear sister, Maryam, whose support has been both professional and personal. Maryam, your introduction to the field of electron microscopy and your expertise in the area have inspired me greatly. Your motivation and guidance were instrumental in my decision to pursue a career in electron microscopy.

I would like to conclude with a poem by Jaleh Esfahani, which holds great meaning for me:

"Life is the unique scene of our artistry,

Each person sings their own song and leaves the stage,

The stage remains constant.

Blessed is the song that people remember."

زندگی صحنه ی یکتای هنرمندی ماست

هر کسی نغمه ی خود خواند و از صحنه رود

صحنه پیوسته به جاست

خرم آن نغمه که مردم بسپارند به یاد